Ollscoil na hÉireann, Corcaigh

National University of Ireland, Cork

University College Cork, Ireland
Coláiste na hOllscoile Corcaigh

Design and Integration Techniques for Compact, Wideband and Multi-functional Baluns

Thesis presented by

Joe Steele, BSc.

https://orcid.org/0009-0008-2645-6416

for the degree of

Master of Research

University College Cork

Department of Electrical and Electronic Engineering

&

Tyndall National Institute

Head of Department: Professor Peter Parbrook

Supervisor: Professor Dimitra Psychogiou

2024

Contents

Declaration

This is to certify that the work I am submitting is my own and has not been submitted for another degree, either at University College Cork or elsewhere. All external references and sources are clearly acknowledged and identified within the contents. I have read and understood the regulations of University College Cork concerning plagiarism and intellectual property.

X

Joe Steele

Abstract

The prevalence of RF components in 5G communications and the 'Internet of Things' (IoT), has resulted in the integration of electronic devices into all facets of life. This has driven the need for RF components with smaller footprints, lower power consumption and less loss, while being more versatile across the ever-more crowded frequency spectrum. RF baluns, being a key front-end passive component in RF communications must meet these requirements, while effectively providing an impedance transformation and converting balanced-to-unbalanced RF signals. However, current balun technologies are typically large in size, lossy, or narrowband, calling for the development new design techniques and integration methods that will overcome these modern challenges.

On the basis of the aforementioned limitations, this dissertation investigates RF and EM design methodologies for the realization of broadside-coupled line baluns with highly-miniaturized footprint, ultra-wide bandwidth (BW), and the added RF capability of bandpass filtering. Furthermore, the thesis outlines the performance capabilities and limitations of commercially available streamlined multilayer PCB processes and emerging additive manufacturing technologies using inkjet printing. Specifically, this thesis lays the foundations for; i) maximizing the fractional bandwidth (FBW) of Marchand baluns (MBs) and capacitively-loaded variants, dependant on process constraints, using broadside coupled transmission lines and perforated ground planes, ii) enhanced footprint miniaturization using self-packaged integration concepts enabled by freeform inkjet printing, and iii) RF co-designed bandpass filtering, by utilising the resonant behaviour of the coupled-line sections and exploiting the inkjet printing process to tailor their coupling levels.

Experimentally validated results that are presented in this work demonstrate i) FBWs up to 122%, larger than what is achievable with the most common balun implementations, ii) footprints below 0.005 λ_g^2, which are competitive with state-of-the-art miniaturised balun designs, and iii) 3rd-order compact RF co-designed filtering baluns, with FBWs from 30-110%, and footprints at least 6x smaller than what is currently presented in the literature.

Table of Abbreviations

AI: Amplitude imbalance
AM: Additive manufacturing
BPF: Bandpass filter
BPF-B: Bandpass filtering balun
BPF-I: Bandpass filtering isolator
BPF-PD: Bandpass filtering power divider
BW: Bandwidth
CI: Conductive ink
CLIP: Continuous liquid interface production
CMOS: Complementary metal oxide semiconductors
CPW: Coplanar waveguide
DI: Dielectric ink
EM: Electromagnetic
EMS: Embedded microstrip
FBW: Fractional bandwidth
GCPW: Grounded coplanar waveguide
GSG: Ground-signal-ground
IP: Intellectual property
LTCC: Low-temperature co-fired ceramics,
MB: Marchand balun
ML PCB: Multilayer printed circuit board
MMIC: Monolithic integrated circuit
MS: Microstrip
IC: Integrated circuit
IoT: Internet of Things
OC: Open-circuit
PCB: Printed circuit board
PI: Phase imbalance
RF: Radio frequency
RL: Return loss
SICL: Substrate integrated coaxial line
SC: Short-circuit
SL: Stripline
SLS: Selective and laser sintering
SMD: Surface-mounted device
SOA: State-of-the-art
SWaP: Size, weight and power
TF: Transfer function
TL: Transmission line
UWB: Ultra-wideband
VNA: Vector network analyser
WB: Wideband

Acknowledgements

Firstly, I would like to thank my supervisor, Prof. Dimitra Psychogiou, for giving me the opportunity to research under her guidance, and for her subsequent tireless efforts in maximising my research potential.

I want to acknowledge and thank the many friends I made at Tyndall, in particular to everyone in the Advanced RF Technologies group, who offered constant assistance throughout my time there.

I acknowledge support from Science Foundation Ireland, Grant 20/RP/8334 and Skyworks Inc. I acknowledge access to SFI funded computing resources and laboratory equipment at Tyndall National Institute. I also to acknowledge the assistance from colleagues at Tyndall National Institute, SkyWorks Inc., and Nano Dimension™ for their assistance in fabricating components presented in this thesis.

I want to thank my parents and brother Conor, for their love and support, and for instilling in me the work ethic that has brought me this far in my academic career. Thank you also to my friends, who got me out of the lab enough to retain my sanity. Finally, thank you to Saerlaith, who gave me every reason in the world to make it to the finish line.

1 Introduction

1.1 Background and Motivation

Since the first RF communication systems – wireless telegraphs in the 1890s – the modern world has become data-centric, with nearly-every person constantly sending and receiving information wirelessly [1]. The digital age and the ever-expanding 'Internet of Things' (IoT) continues to drive the development of wireless and high-speed communications, thus requiring developments in RF technology that will facilitate operability to higher and broader frequency bands. The balun, which is a portmanteau of 'balanced-to-unbalanced', was first documented in the literature as a passive device used to feed the television transmitting antenna for the Empire State Building in 1939 [2]. The balun was so-named due to its input supporting an unbalanced RF signal, while its output supporting a balanced RF signal as shown in Figure 1.1. Baluns perform many different functions in the RF transceiver, such as impedance matching, converting balanced-to-unbalanced RF signals, and suppressing noise in signal transmission [3]. These various capabilities have found uses in the design of many fundamental RF devices, like balanced antenna feeds [4], mixers [5], push-pull amplifiers [6], frequency multipliers [7], phase detectors [8], modulators, and numerous others. Without baluns in particular RF devices such as the above, several issues may arise. These include signal degradation due to the interference caused by the common mode signals and impedance mismatches between the balanced and unbalanced sections. The balun's clear key importance in RF transceivers,

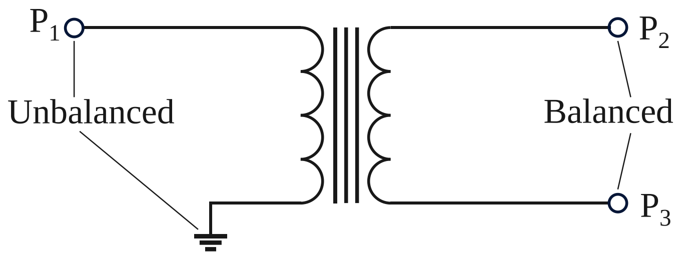

Figure 1.1. Circuit schematic of an ideal balun realised by an ideal transformer with unbalanced port at P_1, and balanced port at P_2 and P_3.

combined with its relatively simple function, motivates the design of baluns with the widest BWs possible, to facilitate their operation over a wide range of 5G frequencies, facilitating the realization of RF transceiver antenna systems that can serve multiple 5G applications at a time.

In addition to designing wideband baluns, there has been increasing interest in the realization of multi-functional RF baluns incorporating multiple RF signal processing functions simultaneously, thus reducing the size of the RF front-end. In particular, due to the large size of bandpass filters (BPFs) and their crucial role in suppressing interference and noise, their RF co-design with other fundamental front-end components is of great importance. Examples of their RF co-design with other fundamental RF components include isolators (BPF-Is) [9], [10], power dividers (BPF-PDs) [11], [12], and antennas (the so called filtenna concept) [130]. The realization of bandpass filtering baluns (BPF-Bs) [13], [14] has also been demonstrated due to BPF-Bs being crucial for antenna front-end interfaces, providing RF filtering while effectively converting unbalanced and balanced RF signals [15], [16].

Alongside a balun's frequency response requirements, innovations are needed in their integration using multilayer processes to facilitate size compactness and low loss, enabling the realization of RF transceivers with small size, weight, and power (SWaP) [3]. As such, alternative integration techniques are being investigated, spanning from streamlined multilayer printed circuit boards (ML PCBs), low-temperature co-fired ceramics (LTCC), monolithic integrated circuits (MMICs), and complementary metal oxide semiconductors (CMOS), all capable of supporting many discrete layers.

To facilitate miniaturization and performance enhancement, new manufacturing processes are constantly being developed, seeking to solve design limitations inherent to modern multilayer processes. One RF manufacturing approach that has been receiving significant attention in recent years is additive manufacturing (AM), with many different technologies being presented to date, spanning from continuous liquid interface production (CLIP) [91], to selective and laser sintering (SLS) [92], and inkjet printing [102]. As opposed to standard ML PCB/LTCC/MMIC manufacturing, where conductive material is removed from each layer to realise the circuit, AM techniques such as inkjet printing add conductive and/or dielectric materials to realise the circuit. This fundamental difference leads to several important benefits with AM over standard PCB manufacturing, offering the potential to greatly enhance device prototyping compared to conventional multilayer processes. AM facilitates on-demand RF components to be fabricated in-house, providing enhanced intellectual property (IP) protection, and significant reduction in the prototyping costs [17]. Furthermore, AM allows for enhanced design freedoms. It is capable of realising 3D shapes and flexible layouts, allowing for improved performance and miniaturized size. AM can additionally decrease the overall device weight (e.g., 3D printed polymers can be 70% lighter compared to conventional FR4 [18]) while having a lower environmental impact and producing less waste material compared to standard multilayer manufacturing. Despite the clear potential of AM in many RF applications, in particular two-material AM processes such as inkjet printing, AM's potential for the realization of RF baluns has not yet been explored.

Considering the aforementioned limitations, the major goal of this thesis is to lay the foundations for new design methodologies and integration techniques for the realization of broadside coupled-line baluns with ultra-wide bandwidths, small physical sizes and the RF co-designed functionality of a BPF. Thus, the objectives of this thesis are to:

i) Develop a comprehensive design methodology that maximizes the fractional bandwidth (FBW) of one of the most popular balun architectures, the Marchand balun (MB), considering the material and geometrical constraints of a manufacturing process.

ii) Investigate the performance capabilities and limitations of a commercially-available streamlined multi-layer PCB process and an emerging two-material inkjet-printed process for the realization of tightly-coupled broadside coupled lines for the design of wideband MBs.

iii) Investigate miniaturization methodologies using vertical integration, spiralling and by exploiting the free-form design and integration capabilities of inkjet printing.

iv) Develop BW widening techniques by investigating capacitively-loaded variants of the MB, and utilising broadside-coupled embedded microstrip transmission lines and perforated ground plane structures.

v) Propose RF co-design techniques that allow bandpass filtering alongside unbalanced-to-balanced RF signal conversion by utilising the resonant behaviour of the coupled-line sections.

1.2 RF Balun Overview

1.2.1 Theoretical background

The balun is a three-port device that has a matched single-ended input (i.e., P_1 in Figure 1.1) and a matched differential output (i.e., P_2 an P_3 in Figure 1.1) and converts an unbalanced RF signal to a balanced one with the output ports of the balun carrying RF signals with equal magnitude and opposite signal phase. This relatively simple definition allows for the S-parameters of the balun, at a given frequency, to be directly written down as follows,

$$S_{12} = S_{21} = -S_{31} = -S_{13} \tag{1.1}$$

$$S_{11} = 0 \tag{1.2}$$

As the balun performs several operations simultaneously, its operational BW is defined by three different metrics that need to be satisfied simultaneously. These are:

1. 10 dB return loss (RL) BW: $|S_{11}| < -10\text{ dB}$
2. Amplitude imbalance (AI): $|S_{31}| - |S_{21}| < 1\text{ dB}$
3. Phase imbalance (PI): $|\angle S_{31}| - |\angle S_{21}| < 180° \pm 10°$

The fractional bandwidth (FBW) of a balun is then the frequency range $[f_L, f_R]$ satisfying these three conditions simultaneously and is calculated by

$$\text{FBW} = 200 \times \frac{f_R - f_L}{f_R + f_L}. \tag{1.3}$$

The second key figure of merit used in the literature is the overall balun footprint, whose dimensions are quoted in units of λ_g, which is the guided wavelength of an RF signal at the balun's centre frequency f_0. A balun's overall performance can then be characterised by its FBW and its occupied area that can be expressed as a fraction of λ_g^2 or its occupied volume as a fraction of λ_g^3. These key metrics will be used in the following sections to understand the current capabilities of the state-of-the-art (SOA) in miniaturised wideband balun design.

1.2.2 Common balun design techniques

A variety of architectures and design approaches have been demonstrated for the realization of compact and wideband baluns to date and they can be summarized into five main categories:

1. ***Inductively-coupled transformer-based baluns*** are the most commonly used approach for the realization of low-frequency balun designs, providing wide BW and excellent signal balance. They are constructed by coiling two individual wires around a magnetic core, akin to a transformer, as shown in Figure 1.2(a). One side of the primary winding is grounded, inducing an unbalanced state on the primary side and a balanced state on the secondary side. Moreover, the secondary side can possess a variable turns ratio to the primary side, resulting in an adjustable impedance transformation between the unbalanced and balanced signals. However, at frequencies above 1 GHz, high hysteresis and eddy current losses limit its performance, while also being bulky for planar integration. Coreless planar spiral inductors have been used at higher frequencies to realise transformer baluns on multilayer circuits, achieving very low footprints (>0.0005 λ_g^2). However, the dielectric-filled core, and capacitive and inductive parasitics greatly narrow their FBW while additional matching networks are needed to recover good signal balance [19]. Transformer-based baluns are therefore only a wideband solution for applications in the early MHz frequency regime, while being an inherently narrowband approach at GHz frequencies and beyond, with FBWs

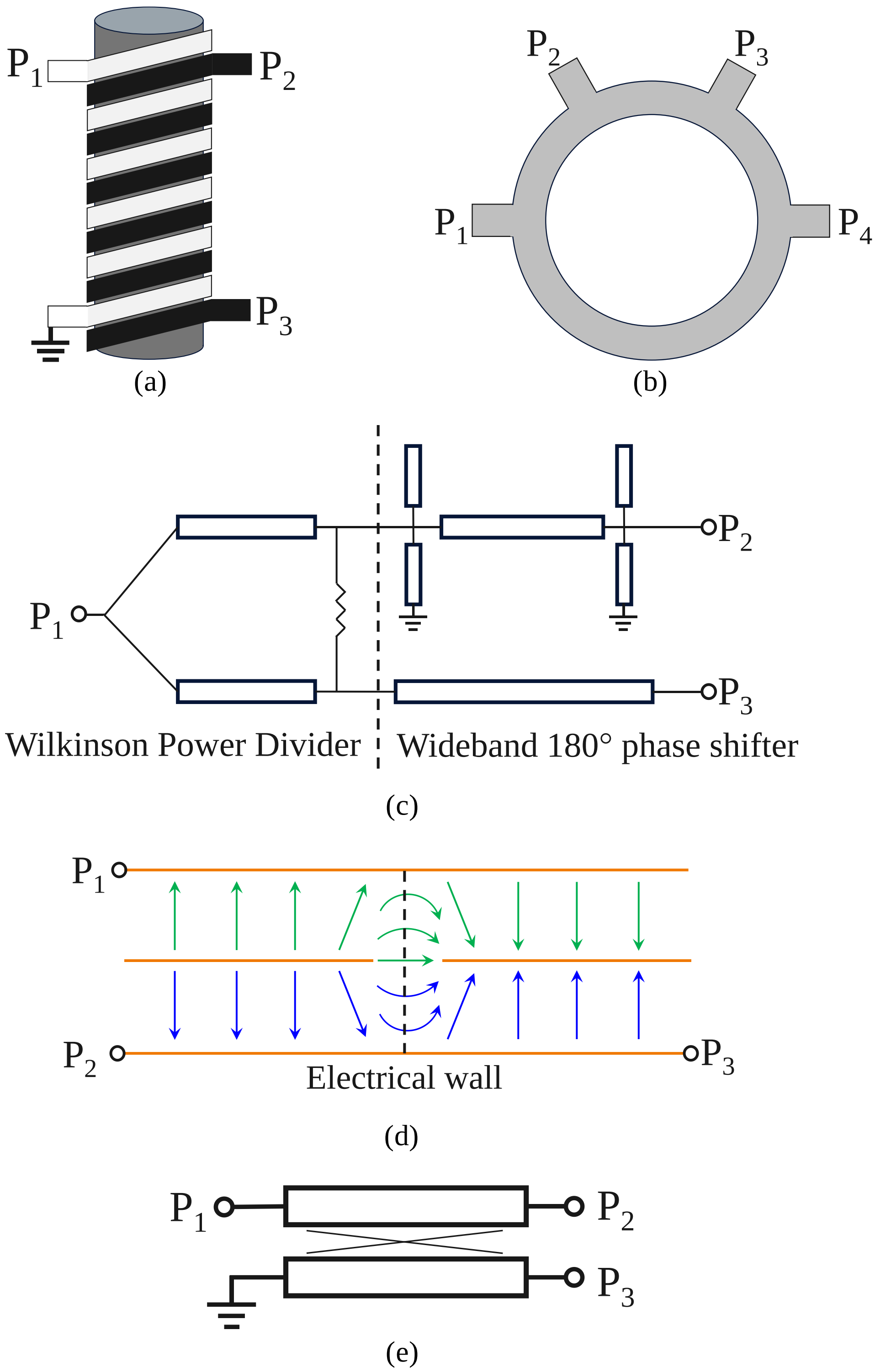

Figure 1.2. (a) Example illustration of a flux-coupled balun, reproduced from [129]. (b) Example illustration of a 180° power-dividing balun, commonly referred as a rat race coupler. (c) Example illustration of a power dividing/phase inverting balun, reproduced from [34]. (d) Illustration of a slotline transition balun, reproduced from [13]. (e) Example illustration of a capacitively-coupled TL balun.

< 40% found across planar implementations [20-23].

2. ***180° power-dividing baluns*** perform the power splitting and phase inversion mechanisms simultaneously. A canonical example of a 180° power-dividing balun is the standard rat-race coupler, also known as a hybrid ring coupler, shown in Figure 1.2(b). This type of balun is a 4-port device where an input signal at port 1 will be split between ports 2 and 4, and port 3 will be isolated. The rat race, along with many other classic 180° power-dividing balun implementations such as the two-section branch-line balun, are typically narrowband (FBWs <50%), while having footprints at least λ_g^2 in size [24], [25]. BW widening techniques using cascaded smaller unit cells have been shown to increase FBW to as large as 93%, but this is at the expense of increasing the overall device footprint [26], [27].

3. ***Power dividing/phase inverting baluns*** execute the two operations of a balun, power division and phase inversion, in succession. This allows for each stage to be designed separately using wideband power splitting and wideband phase inverting approaches and thus can produce wide BWs up to 147% [28]. Power dividing sections typically consist of a multiple-stage Wilkinson power divider, allowing for wide BW power division alongside isolation between the two output ports. The phase inverting stage between the output ports has been implemented using current swapping [28], [29], [30], metamaterial TLs [31], [32], field swapping [33], and other phase shifting stages [29], [34]. An example topology of such a balun is provided in Figure 1.2(c) with the separate stages of the balun labelled. The nature of this implementation, requiring two separate stages results in large footprints above $0.5\lambda_g^2$ which is the major drawback to this approach. In addition, the requirement of resistive components needed to realise Wilkinson power dividing stages hinders this approach for monolithic integration into modern multilayer processes. While this approach can be

used for wideband balun design, it is not capable of offering the low footprints, or ease of integration required for modern multilayer balun design.

4. ***Slotline transition baluns*** have been increasingly researched in recent years due to their wide achievable BWs and high-order filtering capabilities [13], [35-39]. They are typically realized on 2–3-layer multilayer stack-ups using a combination of slotline-to-microstrip transitions, and open-circuited (OC) and short-circuited (SC) stubs, capable of achieving FBWs up to 187%. Their basic operation is demonstrated in Figure 1.2(d), where a cut along a three-layer structure is illustrated. The unbalanced signal enters along the top layer, while the slotline located along the central layer causes the fields to transform in opposite directions at ports 2 and 3. Like those previously discussed, these baluns have large footprints, typically above $0.5\ \lambda_g^2$. Furthermore, when used to functionalize BPF-Bs, this design method results in large device areas, particularly when increasing filter order N. An N+3-order response requires an $N \times \lambda/4$ long slotline (at f_0) which cannot easily be miniaturised.

5. ***Capacitively-coupled transmission line baluns*** are one of the most popular realization approaches as they can deliver on both wide BWs, and significantly miniaturised footprints below $0.001\ \lambda_g^2$ [128], which is the only approach to have similar levels of miniaturisation to the inductively-coupled transformer-based balun. The balun topology shown in Figure 1.2(e) has been demonstrated to exhibit BW ratios up to 46:1 (FBW = 192%), but suffers in its ability for compact, versatile integration into multilayer processes. The sensitive coupled-line structure requires a large footprint for its layout, and multilayer stack-ups requiring air gaps and thick-thin substrates with layer thicknesses up to 90:1 to achieve the necessary coupled-line parameters. This particular topology is therefore generally not suitable for compact

Table 1.1
Performance comparison of the different SOA balun design approaches

Case	**No. of papers**	**Approach**	**FBW range**	**Processes**	**Footprint (λ_g^2)**
1.	~10	Flux-coupled transformer-based	<40%	ML PCB	>0.0005
2.	~10	180° Power divider	<93%	PCB, LTCC	>1
3.	~20	Phase shift balun	<147%	PCB	>0.5
4.	~20	Slotline transition	<187%	ML PCB, LTCC	>0.5
5.	<200	Capacitively-coupled TL-based	<192%	MMIC, ML PCB, LTCC	>0.001

balun design [40-43]. Across this class of baluns, wide FBW responses generally require large coupling coefficients (k), making their practical development often challenging due to the need to materialize narrow TLs with small capacitive gaps in between them [14], [44-55]. In spite of these challenges, this is the only approach that has demonstrated capabilities of low footprints and wideband operation.

Table 1.1 compares the performance of the various SOA approaches that have been presented to date for compact wideband balun design. It is evident that capacitively-coupled TL approaches hold the most promise for the realization of wideband baluns with small footprint, demonstrated by the significantly larger number of published papers on this class of balun topology. All other approaches have considerably larger sizes or narrower bandwidth. Slotline transition baluns do hold potential for simultaneously wide BWs and low footprints, but require significant integration advances for their practical development.

1.2.3 *The planar Marchand balun*

Among the most prominent capacitively-coupled TL-based baluns, the MB has proven the most popular. It was first introduced by Nathan Marchand in 1944 using coaxial lines as shown in Figure 1.4(a) [56] and later converted to a coupled-line implementation, referred to as the compensated MB, shown in Figure 1.4(b), in 1960 by Bawer and Wolfe [57]. This particular topology has achieved BW ratios up to 15:1 and maximum AI and PI between 0.5-1 dB and 5-10°, respectively [58-61]. Like its coaxial line predecessor, it occupies a large footprint ~0.25 λ_g^2. Later on, a simplified version of these MB concepts, the so-called planar MB, shown in Figure 1.4(c) was proposed. It consists of only of two sections of λ/4 coupled lines, however it can achieve FBWs of about 130%, depending on the desired impedance transformation [109].

MBs tend to have large footprints (>0.1 λ_g^2) when implemented using single-layer PCB processes due to being based on λ/4 edge-coupled TLs [68]. Furthermore, their FBW is limited when implemented with edge-coupled TLs which have low couplings (k)—typically below k=0.4 when not using interdigital couplers like the Lange coupler, which increases the coupled line size [126], [127]. FBW enhancement techniques using patterned ground planes [47] or stepped impedance sections [48] lead to FBWs > 100%, however at the expense of footprint. Another integration approach, using thin layer multilayer processes such as CMOS and MMIC facilitate high k>0.8, FBWs of 109% and compact footprints below 0.001 λ_g^2 [17], [47], [62-70]. Their FBWs can however vary, depending on the utilized process dimensions and impedance transformation.

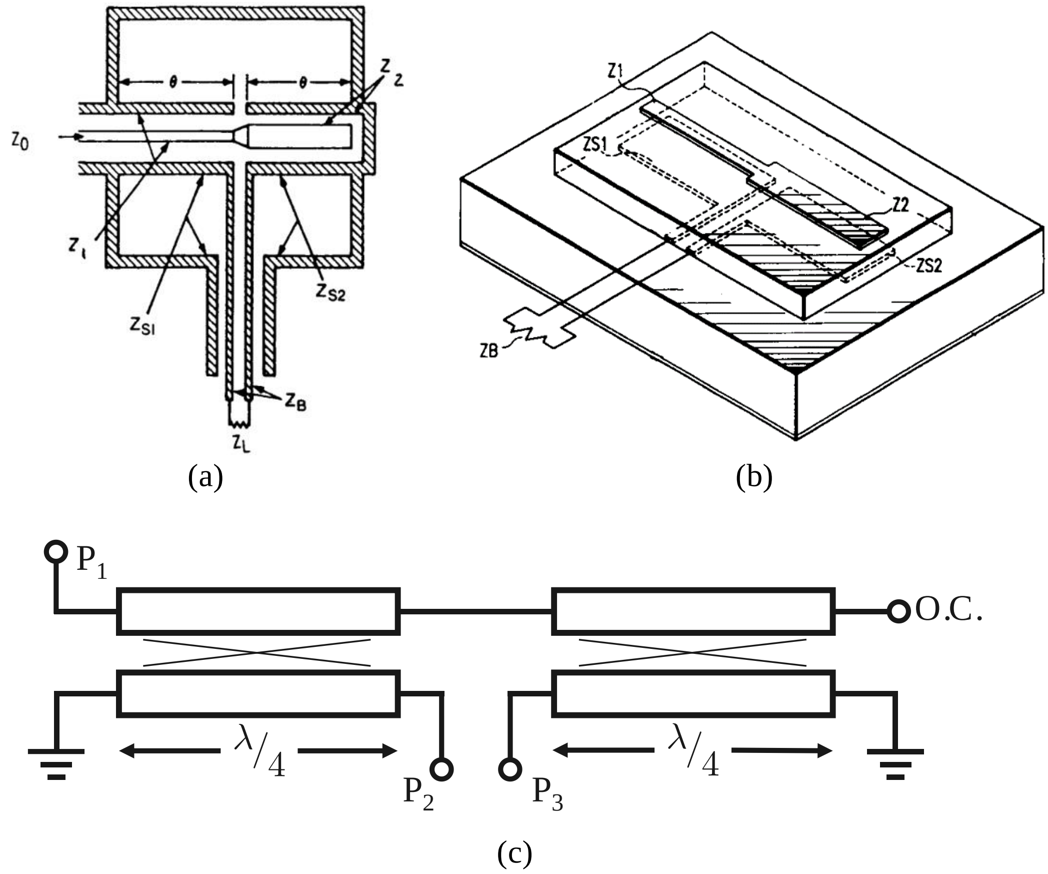

Figure 1.3. (a) The original compensated coaxial line-based MB, reproduced from [46] (b) The converted compensated coupled line-based MB, reproduced from [46]. (c) The planar MB topology.

To achieve the largest FBWs (>100%) in the planar MB configuration, a large *k* is still needed, as is the case with all capacitively-coupled TL topologies, which is the primary restriction on realisable FBW. Several emerging design trends are focusing on BW widening using stepped impedance sections [48], multi-coupled lines [52], [71], patterned ground planes [62], [68], and substrate integrated coaxial lines (SICLs) [72]. However, these approaches lead to large device footprints and can be heavily equation-based, increasing design complexity while lacking insights into the realisable FBW given a process' own limitations. In addition to BW widening, alterations to the topology using capacitive (*C*)-loading techniques are also being investigated for phase compensation, miniaturization, and frequency tunability [67], [69], [73], [74], however at the expense of FBW (<50% [75-79]). FBW enhancement techniques using C-loading were not found across the reviewed literature and are a major objective of this work.

The MB performance improves when materialized using expensive multilayer IC, PCB and LTCC integration platforms [74], [80], [81]. Their thin layer capabilities allow to functionalize a large k and enable miniaturization. However, their performance is limited by their manufacturing capabilities and IC-based MBs typically exhibit high losses when compared to standard PCB, limiting their overall performance. As such there is an increasing need to explore alternative manufacturing and integration concepts for the MB that have the potential to facilitate a high k and low cost. One approach that has not yet been explored in MB design is inkjet AM, which will be explored in this thesis.

1.3 Inkjet-Printed Additive Manufacturing

AM technologies facilitate free-form design and are increasingly being explored for the realization of RF components with enhanced capabilities. A plethora of 3D printed RF components have been reported to date, spanning from antennas [82-87], reflect-arrays [88], frequency selective surfaces [89], and filters [90]. They are manufactured using various techniques, encompassing continuous liquid interface production [91], stereolithography apparatus (SLA), and selective and laser sintering [92]. However, these are single material processes and are either suitable for the realization of fully metallic waveguide components or require post processing for the metallization of their plastic parts using sputtering or electroplating.

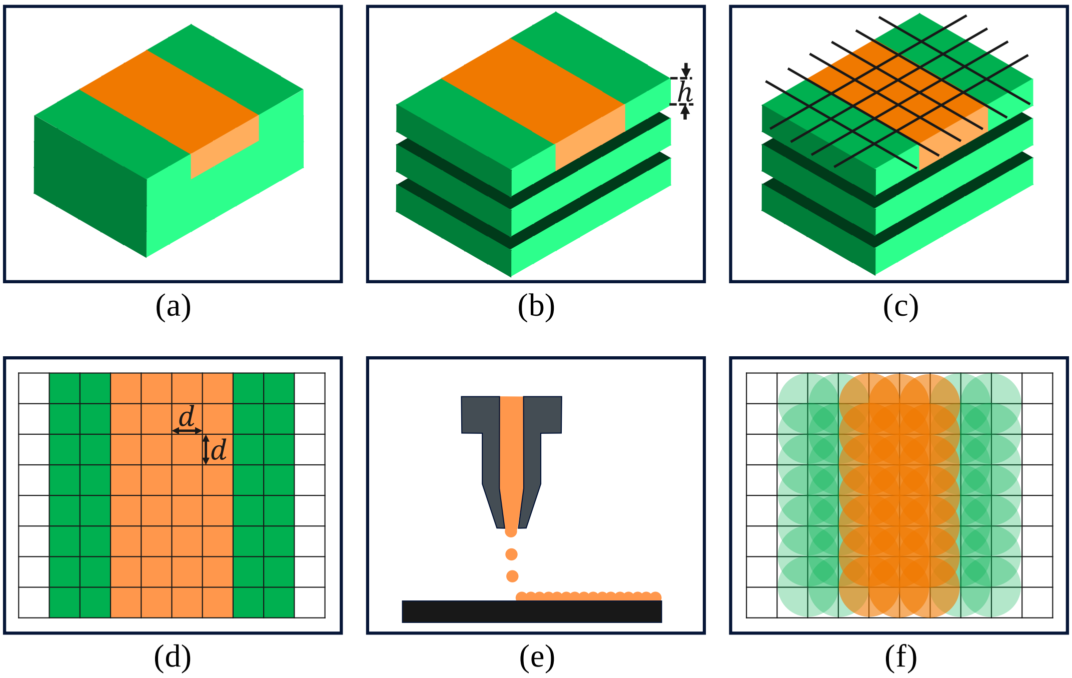

Figure 1.4. (a) 3D two-material structure where dielectric material is in green and conductive material is in orange. (b) Slicing of structure into thin layers with thicknesses h. (c) Pixelization of each layer into a grid. (d) Pixelized circuit layer at a resolution of d. (e) Printing of conductive and dielectric inks. (f) Illustration of the realised printed layer.

For RF components requiring both conductive and dielectric materials in their volume, inkjet-based AM is more suitable and is increasingly being explored as a manufacturing alternative. This AM technique has been used extensively in the realization of patch antennas [93-99]. The basic operation of inkjet-printed AM is shown in Figure 1.4. A given circuit is 'sliced' into layers of a discrete thickness h as shown in (a) and (b). Each layer is then pixelated as shown in Figure 1.4(c) so that a grid with pixels of conductive and dielectric materials can be programmed into the inkjet printer. Multiple nozzles either supply droplets of conductive ink (CI) or dielectric ink (DI) following the pixelized pattern to realise the circuit as shown in Figure 1.4(e), (f). It can be seen in (f) that the droplets do not form as exact square pixels, but that they rather form disks that are efficiently overlapped to realise the pixelized pattern. In theory, this approach allows for totally freeform design within a planar package that can easily be integrated into RF systems. However, most inkjet AM processes are limited to one or two materials and can only produce a single or few vertically stacked layers, with layers having thicknesses $h < 1$ µm resulting in very thin substrates (1-3.5 µm thick) that and cannot easily be used for the realization of 3D RF components that require mm-scale thicknesses. A very promising multilayer inkjet AM process using a silver-based CI and DI was recently developed by Nano Dimension™ [100]. It facilitates thin and thick substrates to be realized by combining multiple dielectric and metallic layers and can be exploited for the realization of vertically integrated components. Component demonstrators using this technology span antennas [101], [102], metasurfaces [103-106], bandpass filters [107], and transmission lines [108], among others. This technology allows for two-material printing up to thicknesses of 3 mm, with total freedom along the *z*-axis. The potential for inkjet printing to revolutionise multilayer RF design motivates its research into all RF components crucial to future communications technologies. For the first time in this thesis, inkjet AM is used for the design of wideband, compact baluns.

1.4 Thesis Outline

Taking into consideration the enabling capabilities of inkjet printing, and the design limitations in modern balun design, this thesis investigates for the first time, the potential to realize wideband and highly-miniaturized MBs using inkjet printing and vertically-integrated tightly-coupled broadside-coupled lines. Capacitively-loaded MB variants focusing on FBW enhancement are explored for the first time in this thesis, with significant increases in realisable FBW reported. Furthermore, this thesis explores new design techniques and integration methods for the realization of highly-miniaturized RF front-ends through the RF co-design of baluns with BPFs.

Additionally, the thesis lays the foundations for comprehensive design methodologies and optimization methods for each topology to determine the maximum achievable FBW depending on the manufacturing process capabilities. A comprehensive comparison with stream-line PCB integration methods is also provided to demonstrate the enabling capabilities for inkjet printing for MB realizations. The rest of this thesis is organized as follows:

- Chapter 2 lays the foundations for the efficient synthesis of broadside-coupled line planar MBs using an inkjet AM process with wide FBWs, good balanced signal quality, and highly miniaturised footprints. Several TL-based integration concepts are analysed using 2D and 3D EM simulations to specify the required impedances and couplings that maximize FBW while taking into consideration the process capabilities of a multi-material multilayer inkjet printing process which is used in this work for the realization of MBs for first time. A miniaturization scheme using spiral TLs and slanted vias is also explored for size compactness. To validate this approach, several coupled-line test structures and MBs were designed, manufactured, and tested. The contributions of this chapter have been published in [109].
- Chapter 3 demonstrates a practical validation of the FBW enhancement design method in Chapter 2 using a streamlined 6-layer PCB process for comparison purposes and discusses its capabilities and limitations. Two MBs using coupled stripline and embedded microstrip TLs are experimentally validated and their performance and design trade-offs in relation to FBW and footprint are analysed. Finally, a comparison between inkjet AM and multilayer PCB baluns across key performance metrics is performed.

- Chapter 4 presents a comprehensive design methodology for *C*-loaded MBs with maximized FBW and highly-miniaturized footprint. The potential of the two-material inkjet AM process is used to demonstrate: i) the realization of *C*-loaded tightly-coupled TLs, leading to ultra-wide FBWs and ii) 3D monolithic capacitor integration that can be exploited for smaller footprints. A FBW enhancement technique using a patterned ground plane is also demonstrated in this chapter.
- Chapter 5 investigates a new design methodology for the realization of highly-miniaturized RF co-designed filtering baluns with high selectivity that can be readily scaled to any order to address the need for compact BPF-Bs in modern wireless communications. BPF-Bs are implemented using inkjet-printed vertically-integrated broadside-coupled TLs. Design limitations regarding the realization of broadband BPF-Bs are investigated by exploiting the free-form manufacturing capabilities of inkjet printing.
- Chapter 6 summarizes the major contributions of this thesis and lays the groundwork for future areas of exploration as a result of this work.

2 Wideband Broadside-Coupled Line Baluns Enabled by Multi-Material Additive Manufacturing

This chapter reports on a comprehensive design methodology for the realization of wideband MBs using a two-material inkjet printing process and their experimental validation. Specifically, this chapter presents a comprehensive analysis on the maximum realizable FBW of MBs, depending on the desired balun impedance transformation and achievable k and an optimization method determining the maximum achievable FBW using broadside coupled-lines. Several TL-based integration concepts are analysed using 2D and 3D electromagnetic (EM) simulations to maximize FBW, while considering the process capabilities of a multi-material, multilayer inkjet printing process. This chapter also includes a validation of the proposed design approach through the design and testing of coupled-line test structures and four MB prototypes. The research outcomes of this chapter have been published in [109].

2.1 Theoretical Foundations of MB Design

2.1.1 Bandwidth limits of Marchand baluns

The circuit schematic details of a MB are provided in Figure 2.1. It transforms an unbalanced RF signal (applied to Port 1) to a balanced one (between Ports 2 and 3) alongside providing an impedance transformation between Z_A (the impedance of Port 1) and Z_B (the impedance of Ports 2, 3). MBs are designed to be perfectly matched at

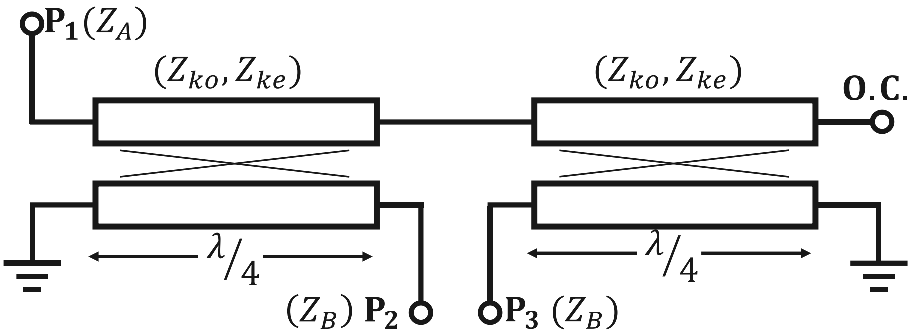

Figure 2.1. Circuit schematic of a planar MB. P_1: Unbalanced port with characteristic impedance Z_A. P_2 and P_3: Balanced ports with characteristic impedance Z_B. All coupled lines are 90° long at f_0 and have characteristic impedance Z_k and coupling k - © IEEE 2024 [109].

their input, i.e., $S_{11} = 0$ at f_0 and all conditions can be met when the even- and odd-mode impedances of the λ/4 coupled lines (Z_{ko}, Z_{ke}) satisfy (2.1) [62]:

$$\frac{1}{Z_{ko}} - \frac{1}{Z_{ke}} = \sqrt{\frac{1}{Z_A Z_B}} \tag{2.1}$$

Using the equivalences for k and the characteristic impedance (Z_k) of the coupled lines in (2.2), an expression can be derived for the optimal Z_k in (2.3).

$$k = \frac{Z_{ke} - Z_{ko}}{Z_{ke} + Z_{ko}}, \qquad Z_k = \sqrt{Z_{ke} Z_{ko}}\,, \tag{2.2}$$

$$Z_k(k) = \sqrt{2 Z_A Z_B}\,\frac{k}{\sqrt{1-k^2}}. \tag{2.3}$$

Whereas these expressions allow (k, Z_k) to be calculated for perfect impedance matching at f_0, they do not provide any insight on the operational FBW of the MB. Thus, the FBW needs to be calculated by computing its S-parameters using ideal linear circuit simulations (e.g. in Keysight's Advanced Design System (ADS) [110]).

To get a better picture on the FBW performance capabilities of the MB dependent on impedance transformation, a parametric study over (k, Z_B) in steps of 0.01 and 2.5

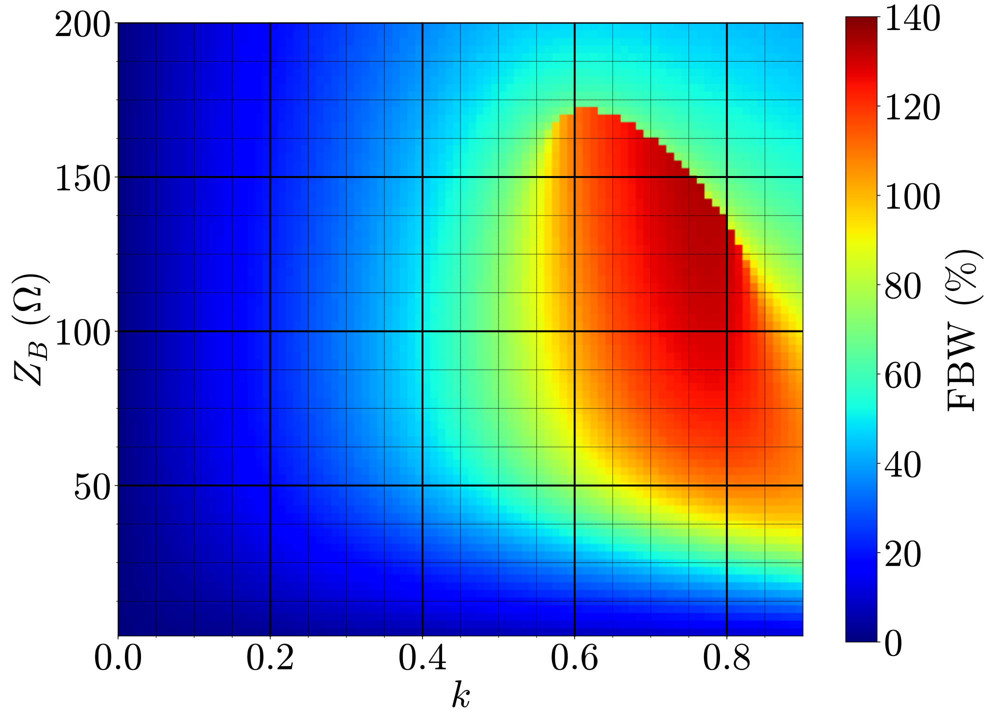

(a)

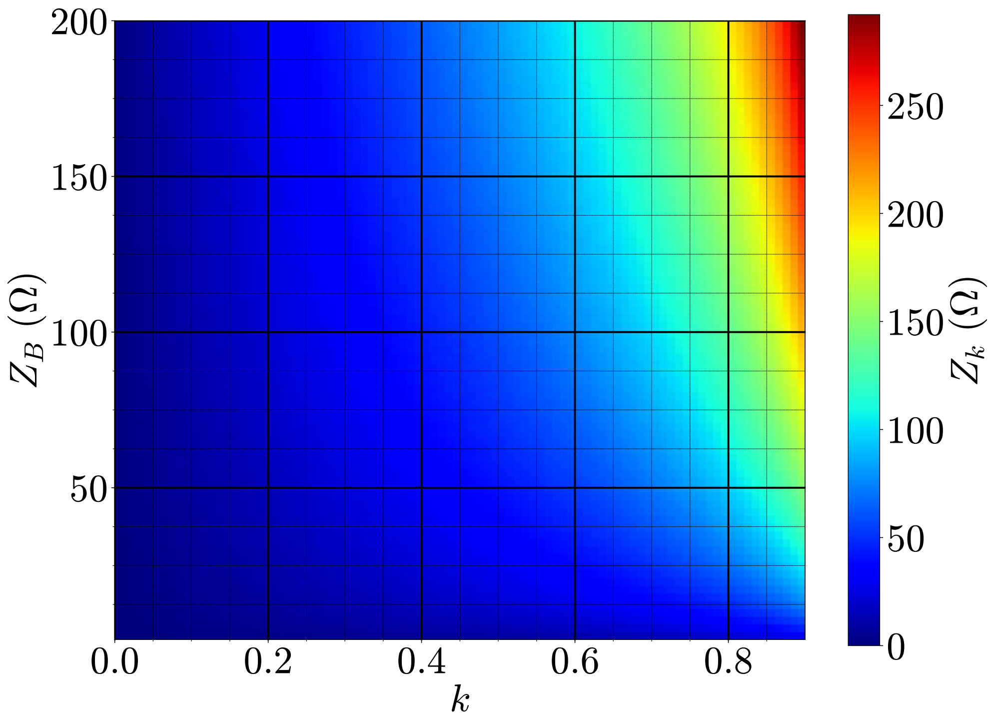

(b)

Figure 2.2. Parameter sweeps of the MB topology in Figure 2.1 as a function of Z_B, k when Z_A = 50 **Ω**. (a) Heatmap of FBW over the (k, Z_B) parameter space. (b) Heatmap of Z_k over the (k, Z_B) parameter space - © IEEE 2024 [109].

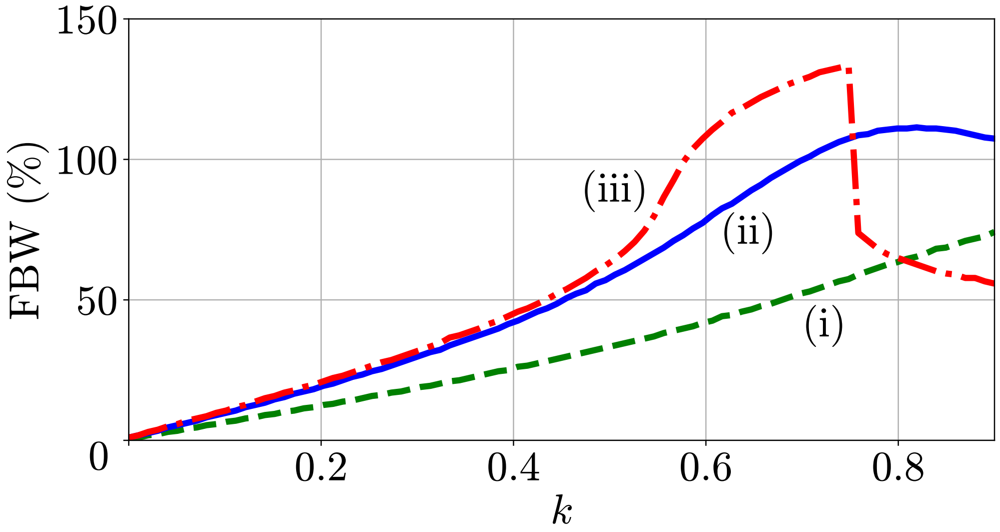

(a)

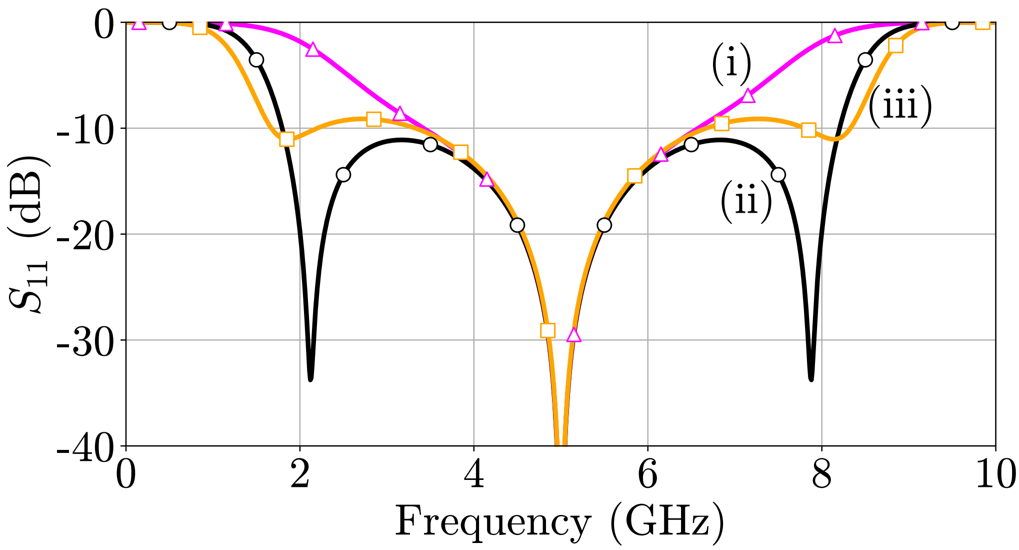

(b)

Figure 2.3. FBW and reflection coefficient ($|S_{11}|$) of the MB topology in Figure 2.1 as a function of Z_B, k when Z_A = 50 Ω. (a) FBW as a function of k for three Z_B example cases. Case (i) Z_B = 25 Ω, case (ii) Z_B = 50 Ω, case (iii) Z_B = 150 Ω. (b) Three example frequency responses of $|S_{11}|$ for Z_B = 150 Ω and varying k. Case (i) k = 0.5, case (ii) k = 0.7, case (iii) k = 0.8 - © IEEE 2024 [109].

Ω respectively was performed and is provided in Figure 2.2(a). As shown, FBWs > 100% can be clearly seen for k > 0.6, while the maximum possible FBWs of about 135% occur around $k \approx 0.7$ for Z_B > 100 Ω. Figure 2.2(b) plots (2.3) for varying k, Z_B, and demonstrates the large Z_k required for large impedance transformations. As a large

Z_k can be difficult to realise, this topology is less useful for baluns with large impedance transformations. To illustrate the possible FBW trends further, three specific cases are provided in Figure 2.3(a). As shown, for lower impedances such as Z_B = 25 Ω in case (i), only FBWs below 62% are possible, whereas for the most common case in the literature, i.e., Z_B = 50 Ω in case (ii), the FBW increases with k and reaches an ultimate maximum of 109% for k = 0.83 and Z_k = 105 Ω. However, such a high k cannot be realized even in advanced commercially available processes such as PCB, LTCC, MMIC, CMOS, etc. (typically below 0.75 [50], [71]), thus the actual FBW in practice is narrower. Case (iii) presents the FBW trends for Z_B = 150 Ω, where a sharp decrease in the FBW is observed shortly after its maximum for k = 0.75 in Figure 2.3(a). This sharp drop can be better explained by examining the S-parameter performance in Figure 2.3(b) for Z_B = 150 Ω and by varying k. As can be seen, the FBW drops due to the reflection zeros at the passband edges moving further away from the centre frequency and resulting in finite reflection. This can also be observed in practice in the MB configuration in [68] that has been implemented for Z_B = 150 Ω (see Figure 3 within).

As Z_A = Z_B = 50 Ω is the most common MB implementation [3], [15], [47], [63], [64], [66], [70], [78], [111-114], this thesis will focus on its realization using inkjet printing and will aim to maximize its FBW. Its corresponding performance is illustrated in detail in Figure 2.4. Based on the obtained relationship between FBW and k in Figure 2.4(a), it can be approximated using the piecewise function in (2.4) that was obtained by interpolating ten extracted pairs of (k, FBW).

$$\mathrm{FBW}(k) = \begin{cases} 118k^3 - 8.25k^2 + 85.5k, & k \leq 0.7 \\ 1371k^3 - 4018k^2 + 3834k - 1089, & k > 0.7 \end{cases} \tag{2.4}$$

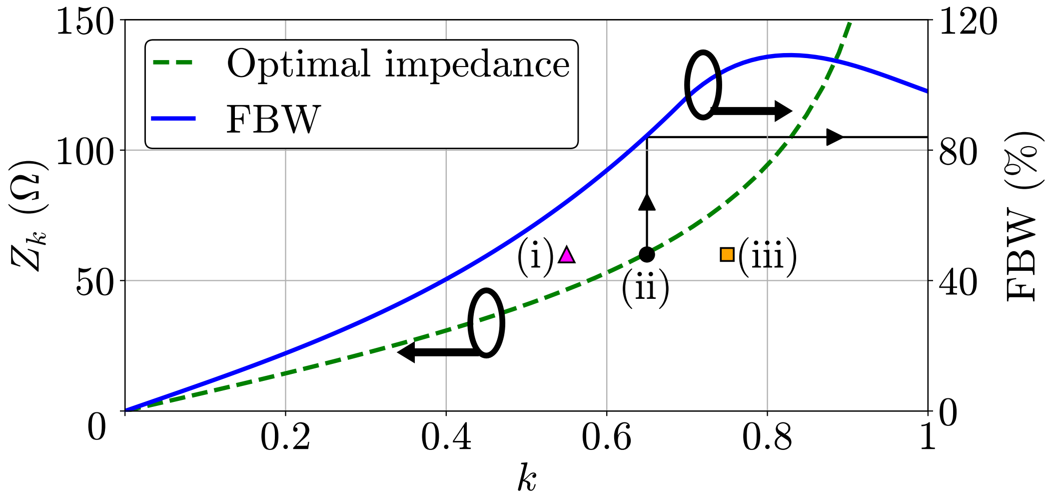

(a)

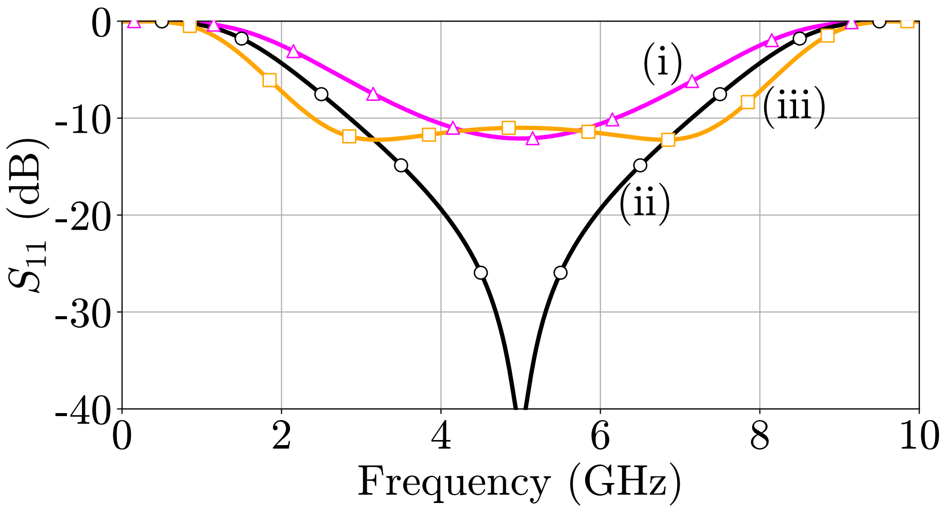

(b)

Figure 2.4. (a) Optimal required Z_k (dashed green line) of the MB in Figure 2.1. Circuit schematic of a planar MB. P_1: Unbalanced port with characteristic impedance Z_A. P_2 and P_3: Balanced ports with characteristic impedance Z_B. All coupled lines are 90° long at f_0 and have a characteristic impedance Z_k as a function of k using (2.3) and resultant FBW calculated from (2.4). (b) Corresponding frequency response of $|S_{11}|$ for three (k, Z_k) example cases with a fixed $Z_k = 60$ Ω. Case (i): $k = 0.55$, case (ii): $k = 0.65$, (ideal), case (iii), $k = 0.75$. In all these examples $Z_A = Z_B = 50$ Ω - © IEEE 2024 [109].

It can be observed that as k increases, FBW also increases, reaching its maximum of 109% when $k = 0.83$, and decreasing thereafter. Thus, it is not generally the case that maximising k will result in a maximum FBW, as is typically the rule of thumb of

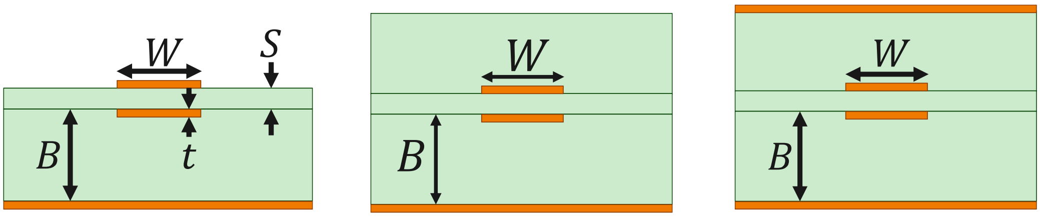

Figure 2.5. Broadside-coupled line types. (a) MS, (b) EMS, and (c) SL - © IEEE 2024 [109].

the open technical literature. It should be further emphasized that (2.4) describes the FBW for perfect matching at f_0, for a given k and corresponding Z_k prescribed by (2.3). If coupled lines with (k, Z_k) not satisfying (2.3) are used, then the matching at f_0 is compromised and may lead to narrower or wider FBWs as shown in Figure 2.4(b) for three design cases. Thus, the significantly degraded matching at f_0 = 5 GHz in cases (i) and (iii) compared to perfect matching in case (ii) demonstrates the necessity of accurately calculating coupled-line parameters for the process that is being used.

2.1.2 Broadside-coupled lines design process

To achieve a high k alongside a small footprint in practice, broadside-coupled TLs are typically preferred to their edge-coupled counterparts due to their k being significantly higher. Three different geometries, namely microstrip (MS, in Figure 2.5(a)), embedded microstrip (EMS, in Figure 2.5(b)) and stripline (SL, in Figure 2.5(c)) are considered and are shown in Figure 2.5. Their performance is determined by considering the capabilities of the inkjet process in [56] with the minimum spacing (S) being the most critical factor. Specifically, the process allows for two different materials to be printed in the same manufacturing platform, namely an acylate-based dielectric ink with relative permittivity (ε_r) ~2.83 and dielectric loss tangent tan(δ) ~ 0.023 at 5 GHz, and a silver nano-particle conductive ink with conductivity σ between 1.8×10^6 – 2.52×10^7 S/m [100], [101], [115]. All initial simulations were performed using the nominal value in the data sheet as 2.21×10^7 S/m [115]. Furthermore, in this process trace widths > 75 µm, trace-to-trace spacings > 100 µm, and small layer thicknesses are possible with the minimum achievable dielectric thickness depending on the thickness of the metallization layer. In this case a metallization thickness of 17 µm (3-11x the skin depth at 5 GHz) is used and a minimum dielectric thickness of 50 µm.

Considering the aforementioned process capabilities, various TL geometries were analysed using 2D and 3D EM simulations in ANSYS in order to extract their Z_k and k values as a function of various geometrical parameters, i.e., the width of the traces (W) and the distance between the traces and the ground (B), are summarized in Figure 2.6 and Figure 2.7 for $S = 50$ µm (the minimum layer thickness). A wide range of Z_k and k can be obtained by freely altering B, an advantage to be highlighted as opposed to conventional PCB, LTCC, and MMIC processes that have finite and discrete layer thicknesses, preventing a continuous range of Z_k and k to be obtained.

The 2D EM simulations were performed on the same coupled-line structures using the Q3D 2D extractor from ANSYS that allows one to extract the *R, L, C, G* (resistance, inductance, capacitance, and conductance, respectively) parameters of the TL [116]. They can be used to calculate the odd- and even-mode capacitances and inductances of the TL using (2.5) where labels 1, 2 denote the upper and the lower conductor, respectively.

$$\begin{aligned} C_o &= 0.5(C_{11} + C_{22} - C_{12} - C_{21}) \\ C_e &= 0.5(C_{11} + C_{22} + C_{12} + C_{21}) \\ L_o &= 0.5(L_{11} + L_{22} - L_{12} - L_{21}) \\ L_e &= 0.5(L_{11} + L_{22} + L_{12} + L_{21}) \end{aligned} \tag{2.5}$$

Subsequently, the odd- and even-mode characteristic impedances (Z_{ko}, Z_{ke}) can be specified using (2.6).

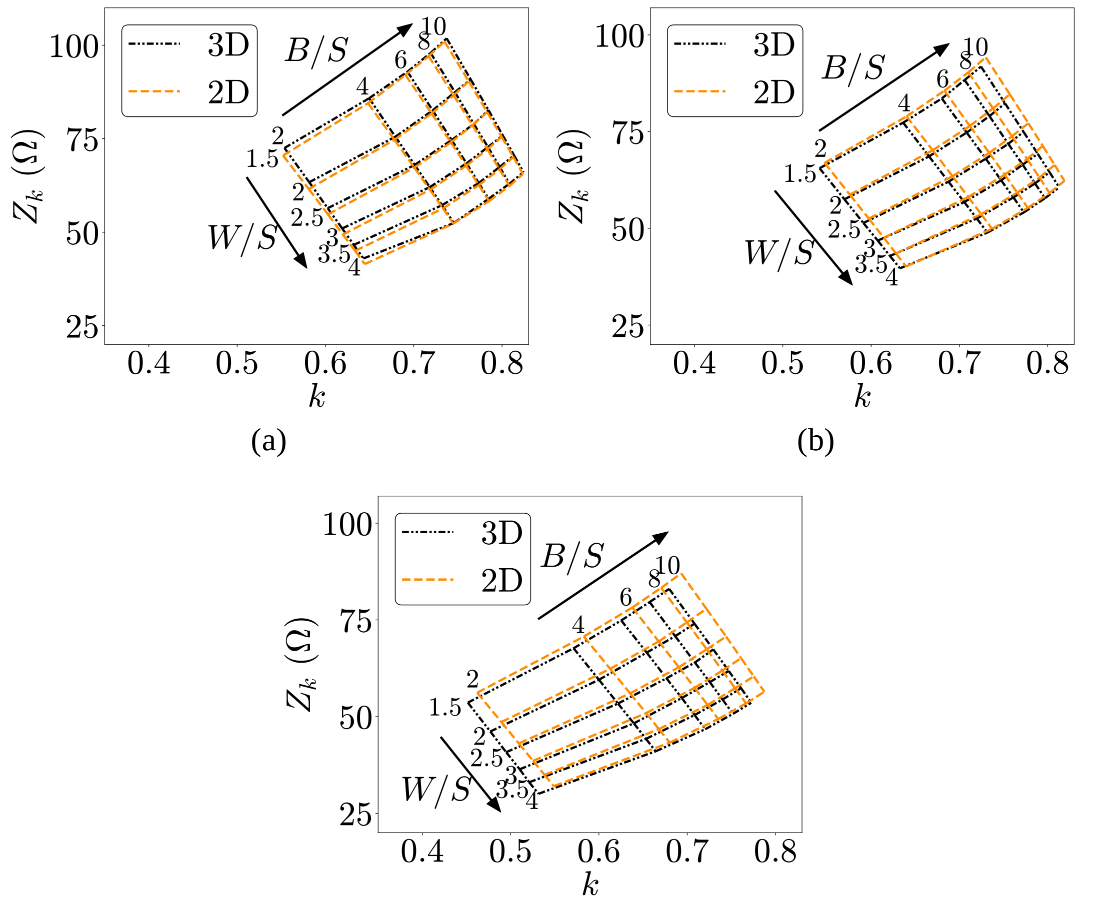

(a) (b) (c)

Figure 2.6. Z_k and k for three types of broadside-coupled lines as a function of the ratios W / S and B / S using the 2D RLCG extraction method and full 3D EM simulations. (a) MS geometry shown in Figure 2.5(a). (b) EMS geometry shown in Figure 2.5(b). (c) SL geometry shown in Figure 2.5(c) - © IEEE 2024 [109].

$$Z_{ko} = \sqrt{\frac{L_o}{C_o}}, \qquad Z_{ke} = \sqrt{\frac{L_e}{C_e}} \tag{2.6}$$

Z_k and k can also be calculated using 3D EM simulations in ANSYS HFSS by exciting the λ/4 coupled lines with differential ports at each end. This allows for the accurate calculation of the common mode impedance (Z_{Comm}) and the differential mode impedance (Z_{Diff}). Then Z_{ko}, Z_{ke} can be computed using (2.7) shown below and Z_k and k using (2.2).

$$Z_{ko} = 0.5 Z_{\text{Diff}}, \qquad Z_{ke} = 2 Z_{\text{Comm}} \tag{2.7}$$

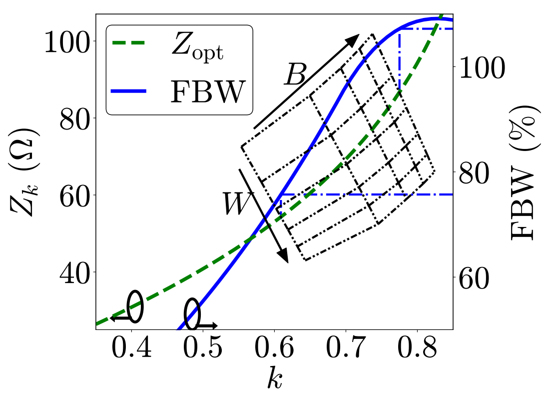

(a)

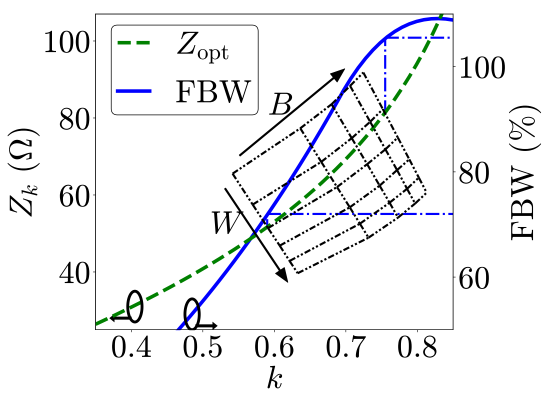

(b)

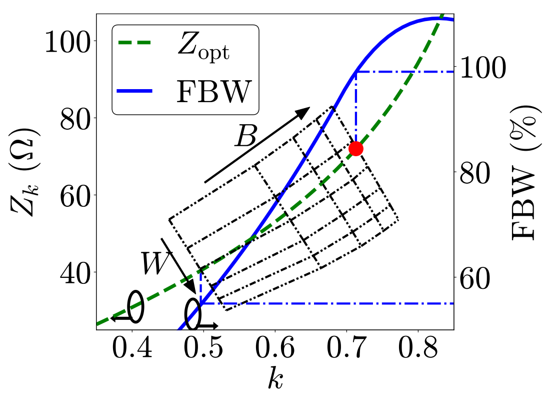

(c)

Figure 2.7. Z_k and k for three types of broadside-coupled lines as a function of the ratios W/S and B/S calculated using full 3D EM simulations. They are overlaid on the optimal Z_k and FBW curves given by (2.3) and (2.4). (a) MS geometry shown in Figure 2.5(a). (b) EMS geometry shown in Figure 2.5(b). (c) SL geometry shown in Figure 2.5(c) - © IEEE 2024 [109].

A comparison between the two methods is provided in Figure 2.6 for all the three different TLs which are in good agreement. It should be noted that the 2D method requires less computational time and is typically quicker to set up, while 3D simulations were found to be more accurate for balun synthesis. Having determined the Z_k and k characteristics of each TL, their optimal values for maximizing the FBW

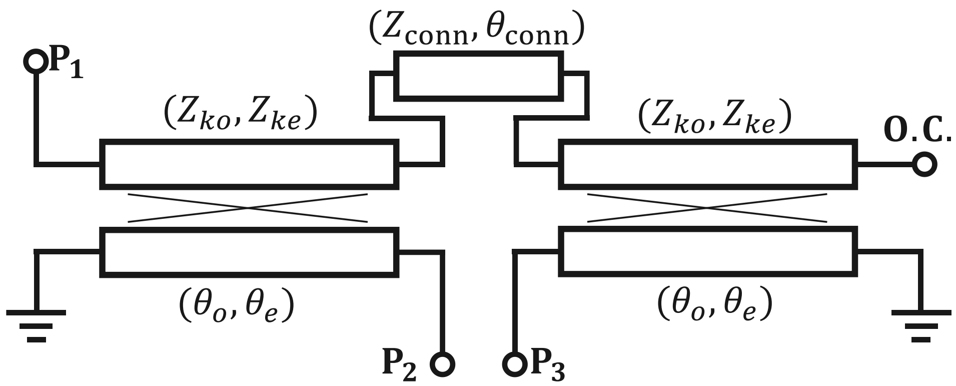

Figure 2.8. Adapted circuit schematic of the MB in Figure 2.1, including the necessary connecting line for practical implementation having characteristic impedance Z_{conn} and electrical length θ_{conn} - © IEEE 2024 [109].

of the MB can be specified graphically. After overlaying the FBW(k) and the $Z_k(k)$ relationships in (2.3) and (2.4) on the same plot, the region of intersection with the computed values of (k, Z_k) and (2.3) is found as shown in Figure 2.7. The design parameter ranges for MS, EMS and SL TLs are provided in **Table 2.1**. As expected, the largest Z_k and k are obtained for the MS coupled lines, leading to an optimal FBW of 107%. The lowest Z_k and k were got for the SL coupled lines leading to a nearly optimal maximum FBW of 99%. As noticed, the EMS performance is in between these two. Although the MS coupled lines are expected to give a slightly higher FBW, they have higher dispersion and may lead to higher AI and PI when used to materialize a MB [117] and may narrow its actual FBW. Thus, SL is used for the practical realization of the inkjet-printed MBs with k = 0.71, Z_k = 71 Ω, indicated by the red marker in

Table 2.1
Coupled-line parameter ranges plotted in Figure 2.7 - © IEEE 2024 [109].

Case	k	Z_k (Ω)	FBW (%)
(a) MS	0.61-0.78	54-88	76-107
(b) EMS	0.59-0.76	52-83	72-105
(c) SL	0.50-0.71	41-71	55-99

Figure 2.7(c), and corresponding to a W = 115 μm, B = 500 μm, and is expected to lead to a FBW = 99%.

2.1.3 Practical realization aspects

To practically realize the MB, an interconnecting line (Z_{conn}, θ_{conn}) as shown in Figure 2.8, needs to be added between the two upper sections to facilitate the realization of the P_2, P_3 outputs that would otherwise fall on top of each other. Additionally, this line can help to balance the AI and PI that is caused due to the dispersion of the coupled lines as discussed in [16]. For perfectly homogenous coupled lines with identical odd- and even- mode phase velocities (θ_o, θ_e), perfect AI and PI can be obtained for $\theta_{\text{conn}} = 0$. However, this is never the case in practice due to the inherently uneven phase velocities. It is then useful to design the connecting line to counteract the uneven (θ_o, θ_e) and improve the balun's AI and PI using (2.8), which gives a design curve of possible (θ_{conn}, Z_{conn}) pairs which ensure $S_{21} = -S_{31}$ at f_0.

$$\frac{1}{Z_{\text{conn}}}\tan\left(\frac{\theta_{\text{conn}}}{2}\right) = \frac{\cot(\theta_e)\csc(\theta_o) - \cot(\theta_o)\csc(\theta_e)}{Z_{ke}\csc(\theta_o) - Z_{ko}\csc(\theta_e)} \tag{2.8}$$

This method however requires the calculation of θ_o, θ_e which can be difficult to calculate using equation-based approaches, especially if using a more complex coupled-line structure. Thus, the full 3D EM extraction approach in Section 2.1.2. is used to obtain θ_o, θ_e. Specifically, θ_o, θ_e are respectively the common mode phase (θ_{Comm}) and the differential mode phase (θ_{Diff}) of these coupled lines at f_0 which can be calculated using (9)

$$\theta_{\text{Comm}} = \angle S_{cc21}, \qquad \theta_{\text{Diff}} = \angle S_{dd21} \tag{2.9}$$

where S_{cc21} and S_{dd21} are the common and differential mode power transmission coefficients [83].

In theory, SL broadside-coupled TLs are perfectly homogenous and have equal odd- and even-mode phase velocities, therefore requiring $\theta_{\text{conn}} = 0°$. Therefore, in practical implementations, when using straight coupled lines, only minor parasitic effects cause deviations from equal odd- and even-mode phase velocities. For the chosen SL parameters, they were calculated as $\theta_o = 88.6°$, $\theta_e = 91.9°$. If the connecting length is known, for example, $L_{\text{conn}} = 500$ µm, firstly $\theta_{\text{conn}} = 4.5°$ is calculated, leading to a $Z_{\text{conn}} = 65\ \Omega$, that corresponds to a width $W_{\text{conn}} = 130$ µm.

2.1.4 Marchand baluns using straight coupled lines

Using the process design guidelines as a reference and full-wave EM simulations in ANSYS HFSS, a MB was designed and is shown in Figure 2.9(a), (b). The addition of the inter-connecting line leads to a perfect matching at f_0 and a small FBW deterioration from 99% to 97%, which is the targeted maximum FBW for the experimental prototype. Straight coupled-line sections are used in this case and are folded side-by-side for size compactness, leading to an overall footprint of $L_{\text{St}} \times W_{\text{St}} \times H = 8.2 \times 1.35 \times 1.12$ mm^3. The RF signal is connected to the coupled lines through a vertical transition that is realized with a 3D via whose size and shape is optimized for minimum reflection loss. The 3D vertical transition is optimised by analysing its reflection coefficient. It was found that having the widths of the 3D vertical transition equal to the terminating CPW width ($W_{\text{CPW}} = 200$ µm) minimised reflection losses. A tapered transition from the coupled-line width ($W = 115$ µm) to the 3D via was used to further minimise reflections.

Grounding vias are also used to interconnect the bottom ground with the top ground plane of the grounded coplanar waveguide (GCPW) of the RF input/output ports as shown in Figure 2.9(b). They have been omitted in Figure 2.9(a) for clarity. The placement of the ground plane of the GCPW ports takes advantage of the design

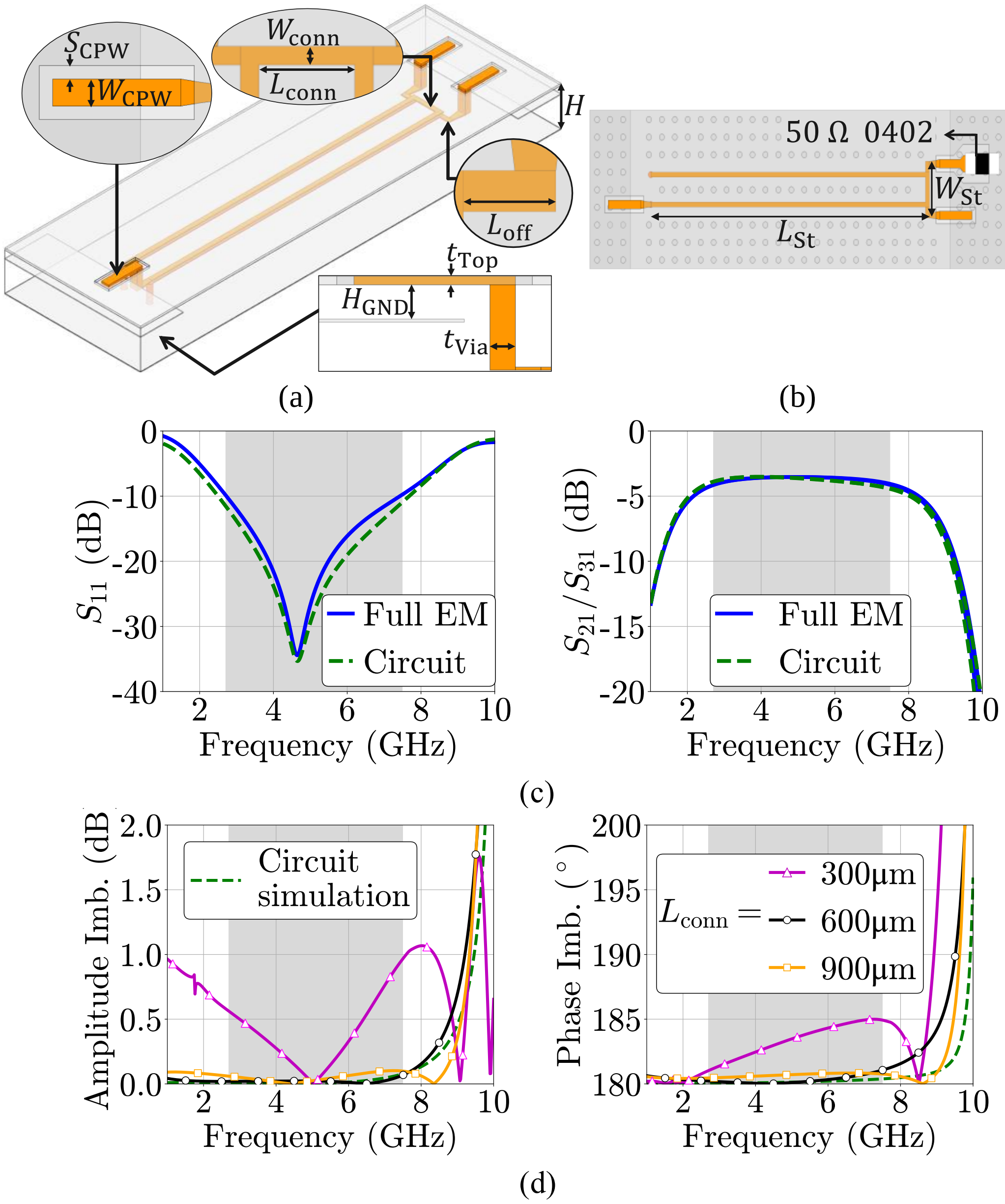

Figure 2.9. (a) Bird's eye view of the 3D geometry and EM simulation model for the inkjet-printed MB based on broadside-coupled straight SLs where L_{conn} = 500 μm, W_{conn} = 130 μm, W_{CPW} = 200 μm, S_{CPW} = 100 μm, H_{GND} = 187 μm, L_{off} = 260 μm, t_{Top} = 50 μm, t_{Via} = 150 μm, and $H = 2B + S + t + t_{Top}$ = 1117 μm. Orange layers: broadside SL coupled-lines materialized with conductive ink. Light grey layers: ground planes materialized with conductive ink. Transparent layers: dielectric ink. (b) Top-view of inkjet-printed MB based on broadside-coupled straight SLs where L_{St} = 8.2 mm and W_{St} = 0.83 mm. (c) Ideal circuit simulation including the connecting line with θ_{conn} = 4.5°, Z_{conn} = 65 Ω and EM-simulated transmission with L_{conn} = 600 μm and W_{conn} = 130 μm. (d) Full EM-simulated AI and PI of the straight balun given in (a) for fixed W_{conn} = 130 μm and varying L_{conn} - © IEEE 2024 [109].

freedom along the z-axis to facilitate excitation using 250 μm GSG probes. Specifically, using the minimum trace-to-trace spacing S_{CPW} = 100 μm, a trace width of W_{CPW} = 200 μm allows for 250 μm GSG probes to properly contact the trace and the ground plane. The impedance of the GCPW can be controlled by H_{GND}. Thus, the required value for H_{GND} can be extracted parametrically and a value of 187 μm was chosen for a 50 Ω GCPW impedance.

Figure 2.9(c) demonstrates the EM-simulated S-parameters of the MB alongside the ones obtained by linear circuit simulations for the same parameters (k = 0.71, Z_k = 71 Ω, θ_{conn} = 4.5° and Z_{conn} = 65 Ω respectively). As shown, they are in a good agreement successfully validating the proposed design methodology. Minor differences are observed in the obtained FBW which was calculated around 97% in the circuit simulations as opposed to 95% in EM simulations. These are to be expected considering the added parasitics from the required junctions and bends in the realistic prototype. Furthermore, Figure 2.9(d) demonstrates the effect of the connecting line on the AI and PI in full EM simulations when varying away from its optimal value L_{conn} = 600 μm. In summary, the EM-simulated MB exhibits the following RF performance characteristics: FBW = 95%, AI < 0.13 dB, and PI < 1.3° throughout this BW.

2.1.5 Miniaturized Marchand balun using spiral lines

Taking into consideration the free-form manufacturing capabilities of the two-material multilayer inkjet printing process, 3D vertical integration alongside spiralling can be considered for size compactness. Figure 2.10(a), (b) depicts the 3D geometry of the resulting MB that has a footprint of 0.043 × 0.094 × 0.028 λ_g^3 two times smaller than the MB based on straight coupled lines in Figure 2.9. Considering that spiralling of the coupled lines can affect the MB's AI and PI due to altering their odd- and even-

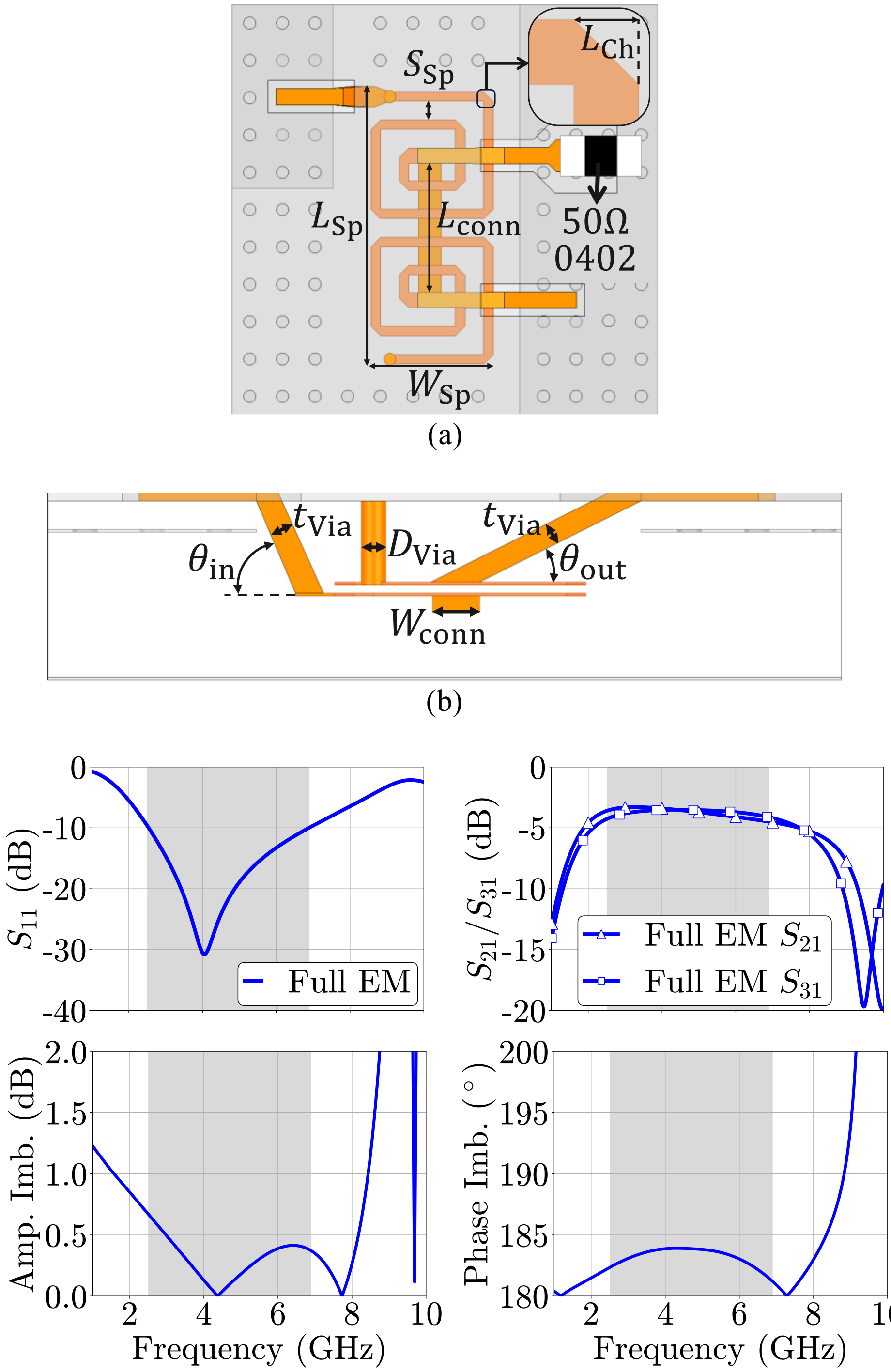

Figure 2.10. (a) Top view of the 3D geometry and EM simulation model for the inkjet-printed MB based on broadside-coupled spiralled SLs where L_{conn} = 1600 µm, L_{Ch} = 130 µm, S_{Sp} = 230 µm, L_{Sp} = 3350 µm, and W_{Sp} = 1530 µm. (b) Side view of geometry where t_{Via} = 150 µm, W_{conn} = 260 µm, D_{Via} = 150 µm, θ_{in} = 67°, and θ_{out} = 27°. (c) Comparison between EM-simulated, and ideal circuit-simulated S_{11} responses and full EM-simulated S_{21} / S_{31}, AI, and PI for k = 0.71, Z_k = 71 Ω, θ_{conn} = 15° and Z_{conn} = 50 Ω, or L_{conn} = 1600 µm and W_{conn} = 260 µm - © IEEE 2024 [109].

mode phase velocities [118], prior to starting the design of the MB, the characteristic parameters of the inter-connecting line need to be recalculated using the design method in Section 2.1.3 and 3D EM simulations. It should be emphasised that in this case, the exact spiralled TL configuration that is used in the MB must be simulated so that correct phase velocities. The increased inductive parasitics caused by the coupled-line spiralling generally require a longer connecting line. These values are as follows: θ_o= 84.6°, θ_e = 97.9°. To lay out the balun compactly, L_{conn} = 1600 µm was first chosen, resulting in a required. W_{conn} = 260 µm following the same design method as before, leading to an overall footprint of $L_{\text{Sp}} \times W_{\text{Sp}} \times H = 3.35 \times 1.53 \times 1.12$ mm^3. The EM-simulated performance of the spiralled-line MB is provided in Figure 2.10(c) and is summarized as follows: FBW = 95%, where AI = 0.35 ± 0.35 dB, and PI = 2 ± 2° over this FBW. As shown, the connecting line has allowed for good AI and PI to be obtained in the passband, but there is clear degradation compared to the straight coupled-line case. This is expected due to the induced parasitics, and current crowding introduced by spiralling the coupled lines.

2.2 Experimental Validation

To validate the potential of the two-material inkjet printing process for the proposed MB designs, various test structures and balun prototypes were manufactured and tested using an Agilent E5071C VNA and 250 µm GSG probes. These include two GCPW TLs, two GCPW-to-SL transitions with vertical and slanted 3D vias, a MB using straight broadside-coupled TLs, and a miniaturized MB using spiralled broadside-coupled TLs. Furthermore, the spiral balun was tested in a back-to-back configuration.

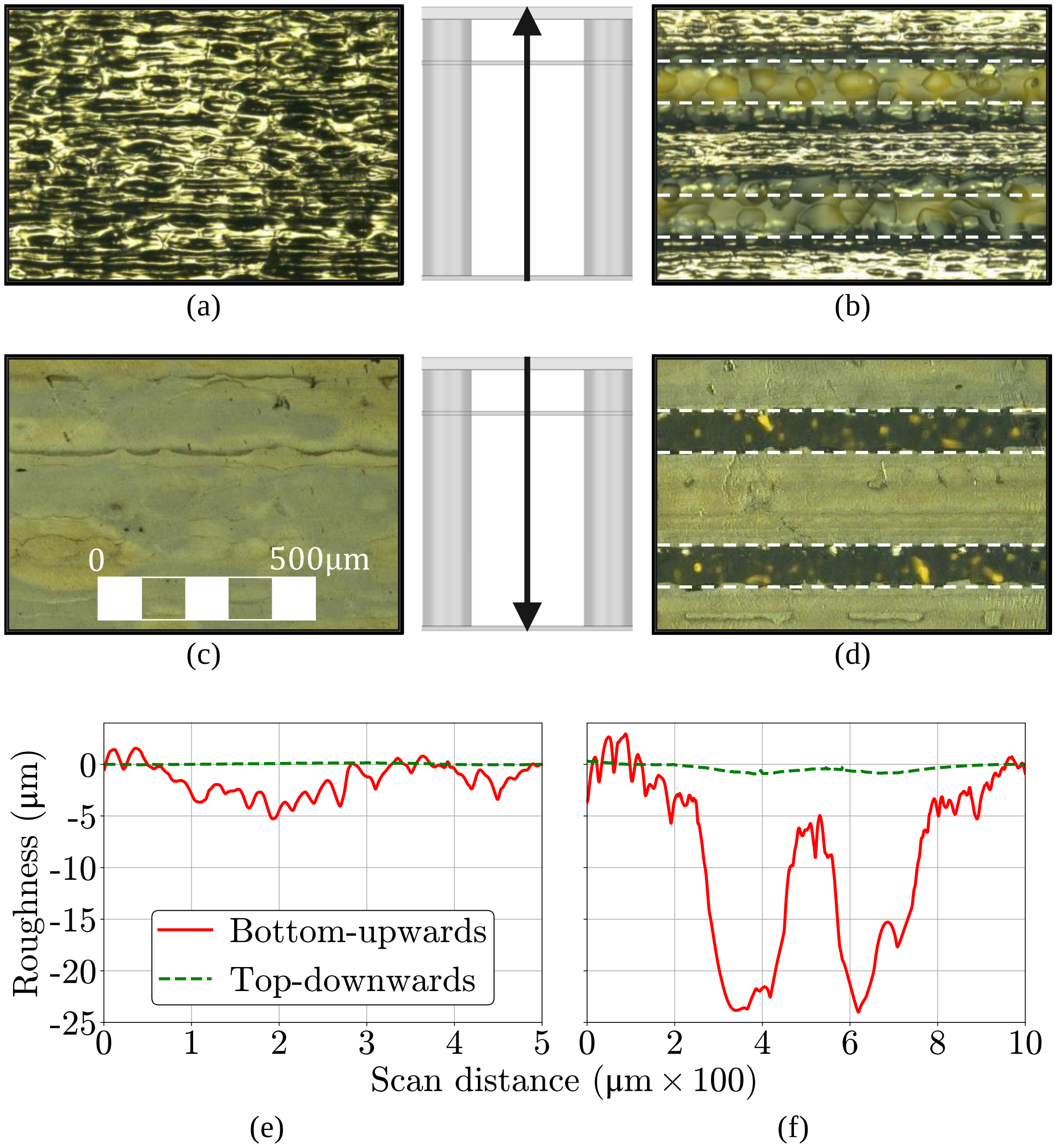

Figure 2.11. Optical images and surface roughness measurements of the manufactured MBs for two different printing orientations, i.e., bottom-upwards [in (a), (b)], and top-downwards [in (c), (d)]. The images zoom into a small metal area [in (a), (c)] and around a GCPW on the top of the test coupon [in (b), (d)]. The ideally designed CPWG profile lines for W_{CPW} = 200 µm and S_{CPW} = 100 µm, are overlaid as dashed white lines. (a), (b) Magnified detail of the metal and the GCPW area of a test coupon printed bottom-upwards and cross section of the coupon showing the printing orientation. (c), (d) Magnified detail of a test coupon printed top-downwards and cross section of the coupon showing the printing orientation. (e) Surface roughness of the metal area. (f) Surface roughness of the GCPW area - © IEEE 2024 [109].

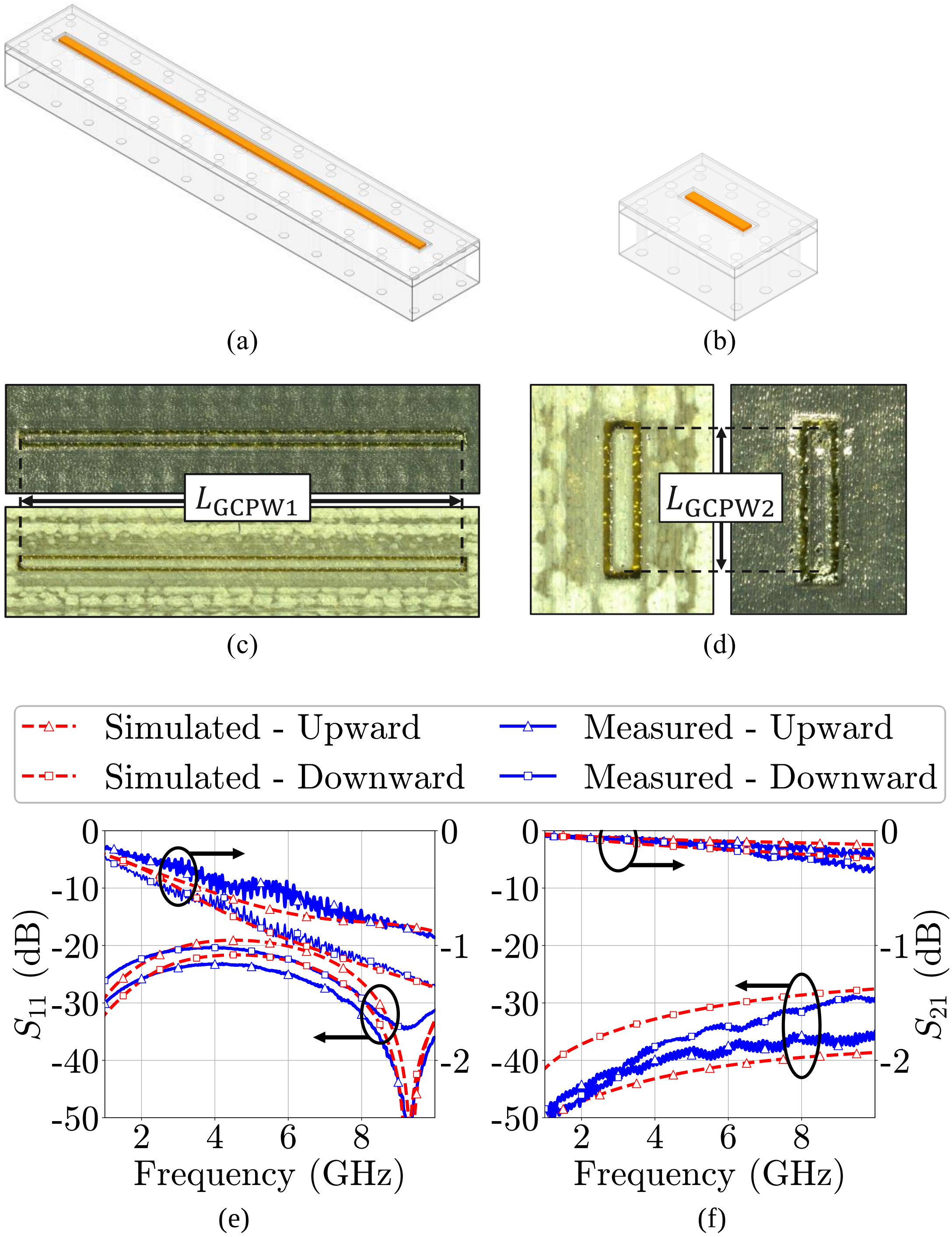

Figure 2.12. Characterization of GCPW TLs having two different lengths. (a), (c), (e) Layout, photograph, EM-simulated and RF-measured S-parameters of the longer GCPW with L_{GCPW1} = 10750 µm for two different printing directions: bottom-upwards (upper image) and top-downwards (lower image). (b), (d), (f) Layout, photograph, EM-simulated and RF-measured S-parameters of the GCPW with L_{GCPW2} = 1400 µm printed bottom-upwards (right image) and top-downwards (left image), and RF-measured *S*-parameters for each print direction - © IEEE 2024 [109].

2.2.1 *Test structures*

The 3D geometries, RF-measured and EM-simulated S-parameters and the surface profile of the test structures is provided in Figures 2.11–2.13. Specifically, Figure 2.11 illustrates the surface profile details of example test areas on the manufacturing coupons. Figure 2.12 displays the 3D geometry, the manufactured prototype, and the RF-measured and EM-simulated performance of two GCPW TLs having two different lengths of L_{GCPW1} = 10.75 mm [Figure 2.12(a), (c), (e)], L_{GCPW2} = 1.4 mm [Figure 2.12(b), (d), (f)] when printed bottom-upwards and top-downwards as shown in Figure 2.11. It can be observed that the test structures printed top-downwards exhibit less loss. This is due to the top layers of the GCPW being the first layers that are printed, therefore being directly attached onto the build plate which allows for a smooth surface to be obtained. To verify this further, Figure 2.11 provides magnified optical images and the measured surface roughness of sample areas around the test samples for a fully metalized area away from the GCPW and around the GCPW for the two different print orientations. They were obtained using a Tencor P10 surface profiler. In the bottom-upwards orientation in Figure 2.11(a), the roughness average of the surface (R_a) varies between 1.8 – 4.2 μm whereas in the top-downwards orientation in Figure 2.11(b), it varies between 0.04–0.2 μm. Taking several sample profiles over various regions on each coupon, an average $R_a \approx 2$ μm was estimated for the bottom-upward prototypes and $R_a \approx 0.1$ μm for the top-downward ones. In addition to the roughness, the printing orientation also affects the dimensions of the GCPW as evidenced in Figure 2.11(b), (d). As noticed in the bottom-upwards case, the GCPW profile deviates from the desired dimensions (marked with white dashed lines for clarity) with the gaps between the inner and the outer grounds being wider than expected, possibly leading to additional reflection loss as shown in Figure 2.12(e), (f). The GCPW profile quality is

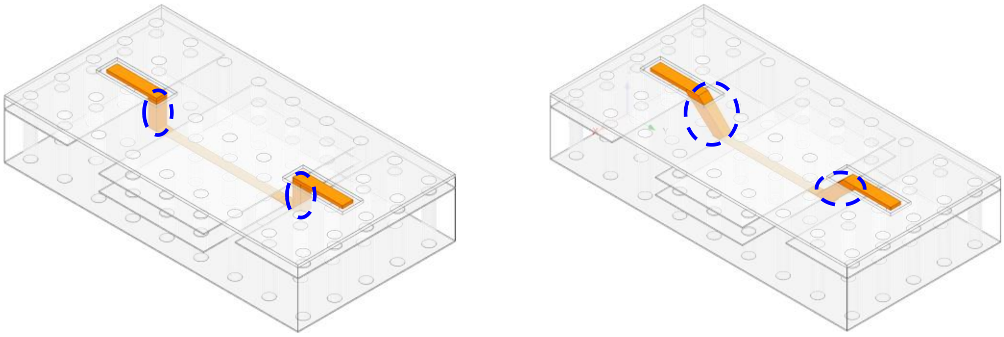

(a)

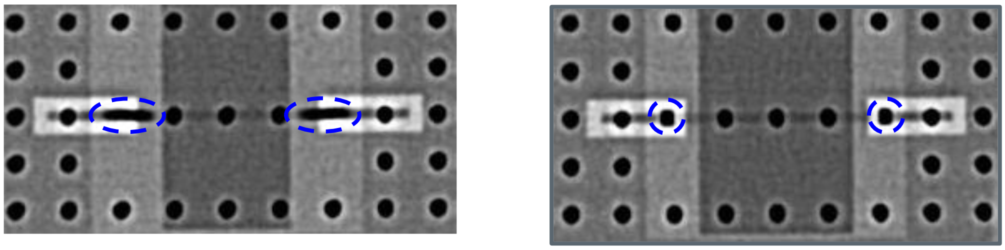

(b)

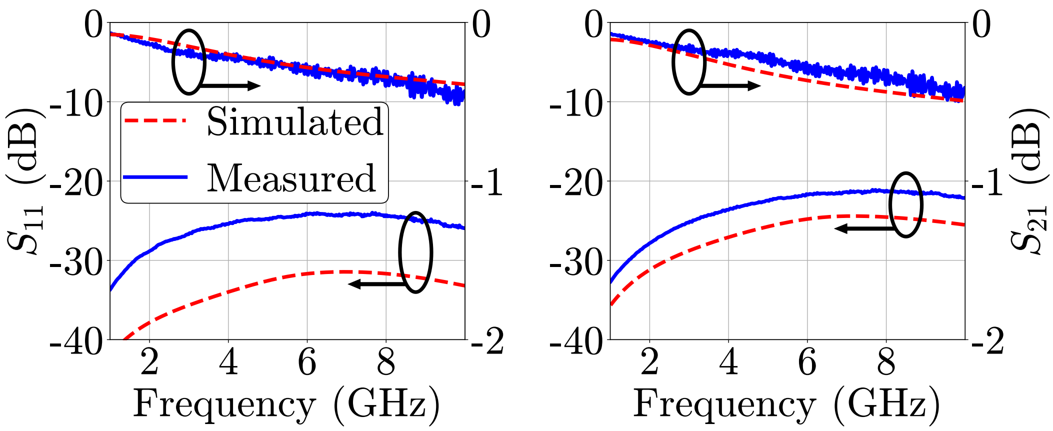

(c)

Figure 2.13. Characterization of 3D vertical and sloped via transition test structures. (a) 3D EM models of the slanted transition (left) and the vertical transition (right) with transitions indicated with dashed circles. (b) Top view of X-ray scans of slanted transition (left) and the vertical transition (right). (c) EM-simulated and RF-measured S-parameters of the slanted transition (left) and the vertical transition (right) - © IEEE 2024 [109].

provided in Figure 2.11(f). As shown in the bottom-upwards orientation, significant differences of up to 25 μm can be observed from the expected perfectly flat surface. Figure 2.12(e), (f) also include the EM-simulated responses of the test structures for alternative levels of roughness. A good agreement is obtained between the EM-simulated and the RF-measured responses when using the measured R_a values of 0.1 μm for the top-downwards case and R_a = 2 μm for the bottom-upwards case in combination with a conductivity $\sigma = 1.8 \times 10^6$ Sm^{-1} [119]. Taking into consideration that the printing orientation affects RF performance, the top-downwards approach was used for the manufacturing of the rest of the test structures and devices.

To investigate the quality of the vertical transitions, two test structures, namely: i) a GCPW-to-SL transition using a vertical 3D via and ii) a GCPW-to-SL transition with a slanted 3D via were manufactured and tested in a back-to-back configuration using a 17° (at 5 GHz) long piece of SL and are shown in Figure 2.13(a). X-rays of their prototypes are shown in Figure 2.13(b) with the transitions being indicated with dashed lines. Their EM-simulated and RF-measured S-parameters are provided in Figure 2.13(c) and appear to be in a good agreement, successfully validating the manufacturing process that leads to broadband (1-10 GHz), well-matched and low loss transitions. The agreement gives further evidence as to the validity of the material parameters used in simulation and using these simulations as a reference, the loss of the slanted and vertical structures was estimated at 0.11 and 0.12 dB at 5 GHz, respectively.

2.2.2 Marchand baluns

Optical scans of the test boards are included in Figure 2.14(a), (b) where the boards were printed bottom-upward in (a) and top-downward in (b). The following results all come from boards that were printed top-downward to achieve the smooth top surface. Due to only being able to test the MBs using a two port GSG characterization system; for each of the two different MBs, two resistively-terminated prototypes, named Balun A (P_3 resistively-terminated) and Balun B (P_2 resistively-terminated) were manufactured and tested so that each balun is tested as a 2-port device. The resistive

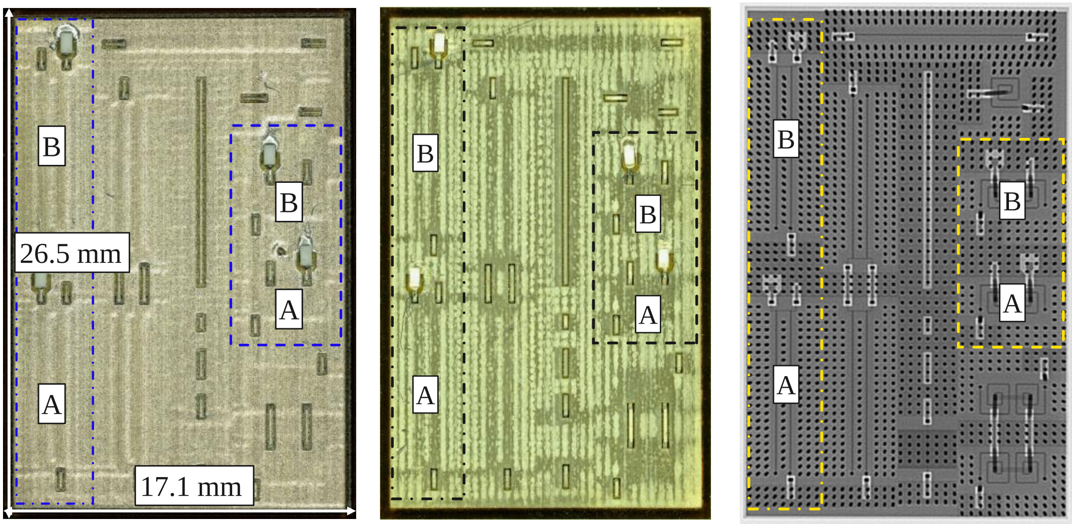

(a) (b) (c)

Figure 2.14. Optical cans of test coupons that include multiple devices and test structures. Example devices of the straight coupled-line (dot-dash lines) and spiralled-coupled line (dashed lines) baluns are indicated on each board. (a) Top view of an optical scan of a board printed bottom-upward where resistive terminations using 0402 resistors have been soldered on. (b) Top view of an optical scan of a board printed top-downward where resistive terminations using 0402 resistors have been soldered on. (c) X-ray view displaying internal structures underneath the top ground plane - © IEEE 2024 [109].

terminations were implemented using thick film 0402 surface-mounted device (SMD) resistors manufactured by YAGEO, and soldered onto pads which were designed to fit these resistors. These separate cases are indicated in the manufactured coupon in Figure 2.14(a), (b), with dot-dashed lines indicating the straight baluns, and dashed lines the spiral baluns. An X-ray scan of the coupon is shown in Figure 2.14(c).

Beginning with the straight coupled-line case, an X-ray photograph of an example manufactured prototype of the MB is provided in Figure 2.15(a). Its EM-simulated and RF-measured performance in terms of S-parameters, AI and PI are provided in Figure 2.15(b). They have been obtained by measuring the S-parameters of two different resistively-terminated baluns, namely Balun A and Balun B. The resistive termination

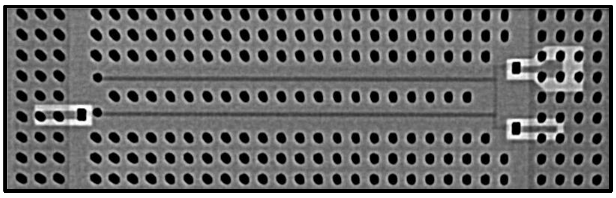

(a)

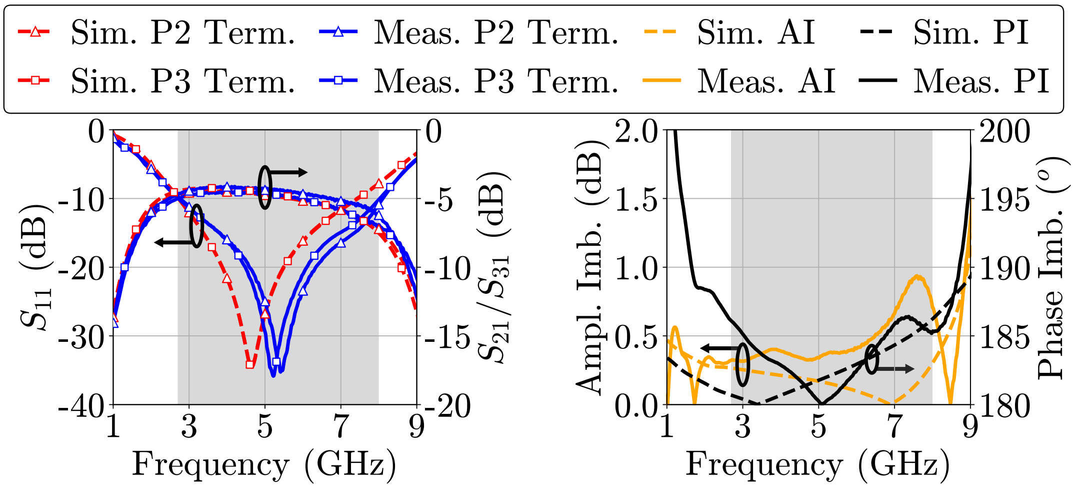

(b)

Figure 2.15. Resistively-terminated SL-based straight MB alongside its corresponding EM-simulated and RF-measured S-parameters, AI, and PI. (a) X-ray image of the manufactured SL-based straight MB (Balun A) with P_3 terminated to a 50 Ω 0402 resistor. The MB with resistive termination at port 3 (Balun B) has been omitted due to their similarity. The circles indicate the grounding vias. (b) EM-simulated and RF-measured S-parameters (top) of two resistively-terminated MBs (Balun A: Corresponding to S_{21A} where P_3 is resistively-terminated, Balun B: Corresponding to S_{21B} where P_2 is resistively-terminated) and calculated EM-simulated and RF-measured AI and PI. The shaded grey area indicates the operational bandwidth - © IEEE 2024 [109].

was performed with a 50 Ω 0402 resistor. Its RF-measured performance is summarized as follows: centre frequency (f_0) = 4.4 GHz, BW between 2.8-8 GHz and FBW of 96.3% that is shaded with a grey area in Figure 2.15(b) and appear to be in a good agreement with EM simulations. Across this BW, the measured power loss (where the vertical transition loss is included) was calculated between 1.2-3.9 dB and the PI was 3.5 ± 3.5°, and AI was 0.6 ± 0.3 dB. The finite amount of insertion loss is due to the

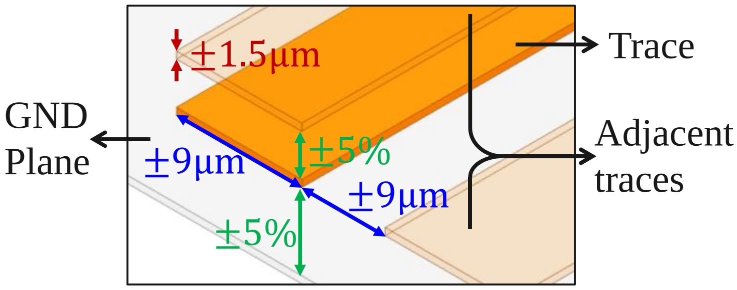

(a)

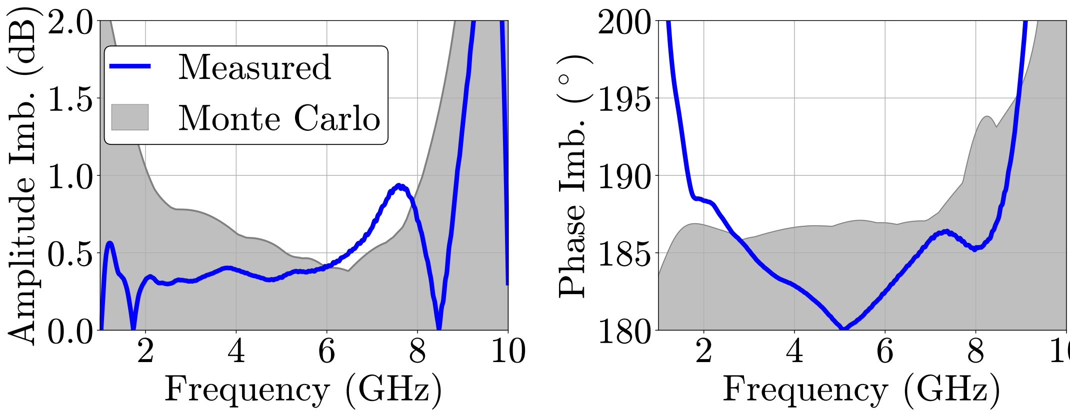

(b)

Figure 2.16. (a) Illustration of potential tolerance variations. (b) Resulting AI and PI between Balun A and Balun B estimated by Monte Carlo simulations with the RF-measured AI and PI overlayed. In these examples, R_a = 2 μm and $\sigma = 1.8\times10^6$ S/m are considered - © IEEE 2024 [109].

finite conductivity of the silver ink and the moderate tan(δ) of the dielectric ink. Furthermore, the conductive losses may also be impacted by the finite thickness of the conductors which are about 3x of the skin-depth. Conductive losses may be improved by using thicker conductors and dielectric losses can be minimized by opening air cavities around the TLs, however at the expense of size. The PI and AI are also plotted in Figure 2.15(b) and appear to be slightly higher than the ones predicted in EM simulations. This is due to the AI and PI being calculated by measurements performed between two different prototypes (i.e., Balun A and Balun B) which may be slightly different to one another due to process variations on the same coupon.

To evaluate the manufacturing tolerances effect on the AI and PI of the resistively-terminated baluns, the tolerances indicated in Figure 2.16(a) are considered. Specifically, all conductive layer thickness can vary within ±1.5 μm, the dielectric layer thickness can vary within ±5%, and the trace width and conductor-to-conductor spacings within ±9 μm. Furthermore, the SMD resistors have a ±10% tolerance. Monte Carlo simulations were performed and are provided in Figure 2.16(b). As shown, the obtained AI and PI range overlaps almost fully with the obtained AI and PI responses in RF measurements, demonstrating that it is likely these differences are mostly due to being estimated from two separate, resistively-terminated prototypes. The observed PI discrepancies at low frequencies are assumed to be due to the stray capacitances introduced by fabrication errors. However, these are outside of the desired operational range which is quite broad and shows acceptable AI and PI characteristics. AI and PI naturally are expected to be smaller if measured on a single MB device using 3-port RF characterization.

The spiral MB was also validated experimentally. Its manufactured prototype is provided in Figure 2.17(a) and its EM-simulated and RF-measured performance in terms of S-parameters, AI and PI are provided in Figure 2.17(b). They have also been obtained by measuring the S-parameters of two different resistively-terminated baluns. The RF-measured performance is summarized as follows: centre frequency (f_0) = 4.4 GHz, BW between 2.8-8 GHz and FBW of 95% that is shaded with a grey area in Figure 2.17(b). Across this BW, the power loss (where the slanted vertical transition loss is included) was measured between 1.2-3.9 dB, the PI was 3.5 ± 3.5°, and the AI was 0.6 ± 0.3 dB. The EM simulation responses are also provided and are in good agreement with the EM-simulated ones successfully validating the proposed spiral MB balun concept.

The spiral MB performance was also evaluated by manufacturing and testing an

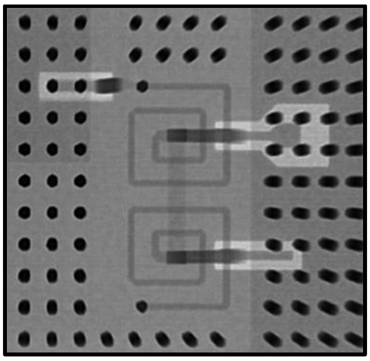

(a)

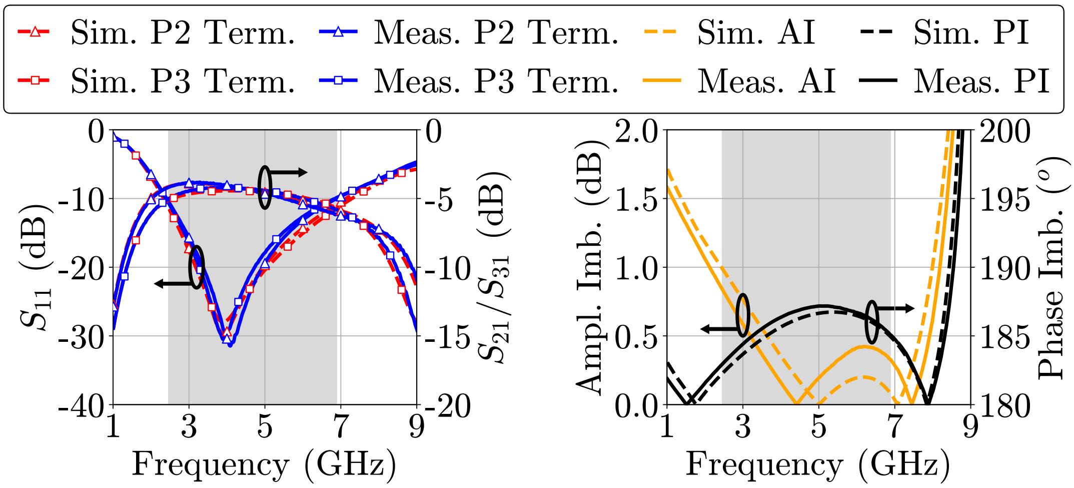

(b)

Figure 2.17. Resistively-terminated spiral MB alongside its corresponding EM-simulated and RF-measured S-parameters, AI, and PI. (a) X-ray image of the manufactured SL-based spiral MB (Balun A) with P_2 terminated to a 50 Ω resistor. (b) EM-simulated and RF-measured S-parameters (top) of two resistively-terminated MBs (Balun A: P_2 is resistively-terminated, Balun B: P_3 is resistively-terminated) and calculated EM-simulated and RF-measured AI and PI. The shaded grey area indicates the operational bandwidth - © IEEE 2024 [109].

additional prototype with two MBs arranged in a back-to-back configuration. TLs were required to route signals out from the centre of each spiral. Its photograph, illustrative circuit schematic, and EM-simulated and RF-measured responses are provided in Figure 2.18. The RF-measured performance is seen to be in close agreement with the EM-simulated one, successfully validating the proposed concept. It exhibits an insertion loss of 1.8 dB at f_0 = 4.4 GHz, with a 3 dB BW from 2.1-8.1

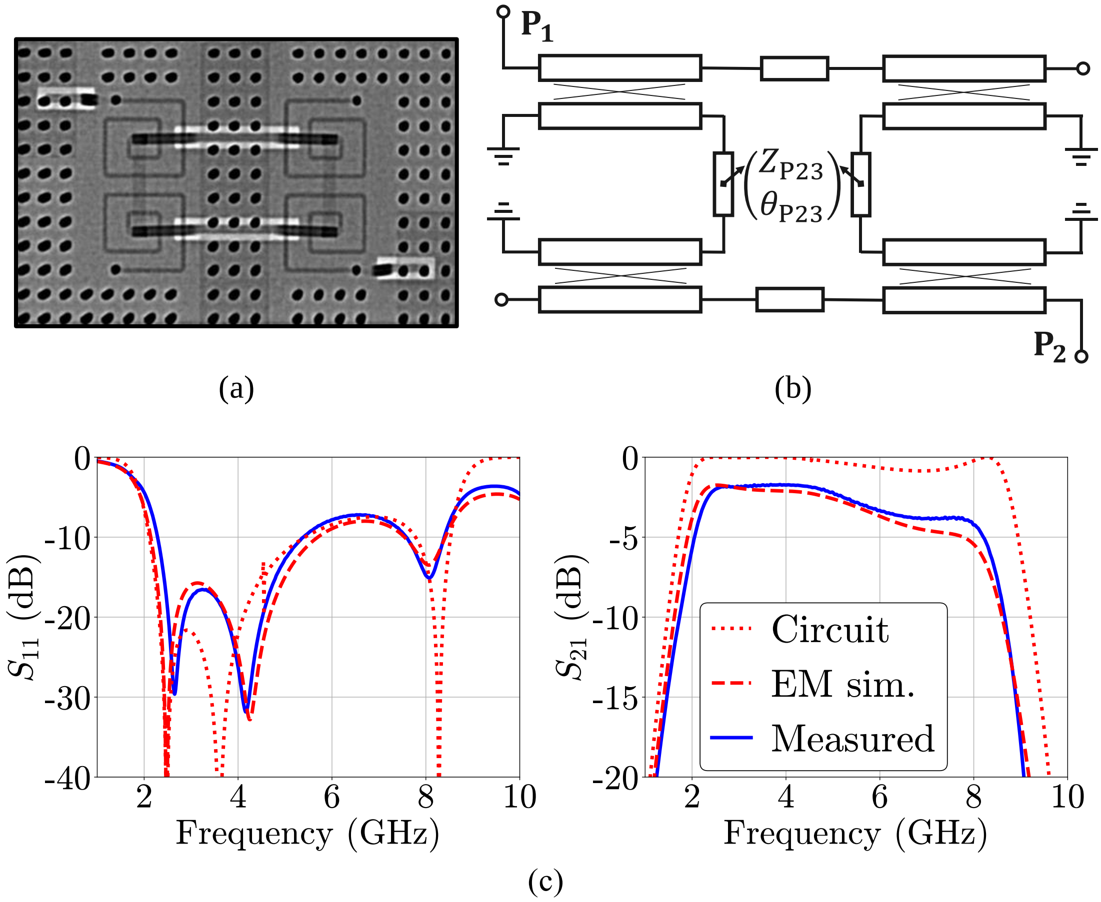

Figure 2.18. Characterization of the spiral SL-based MB in back-to-back configuration. (a) X-ray image of the prototype. (b) Illustrative circuit schematic, indicating the additional lines required to connect the two spiral baluns in a back-to-back configuration where Z_{P23} = 50 Ω, θ_{P23} = 15°. (c) Circuit-simulated, EM-simulated, and RF-measured S-parameters - © IEEE 2024 [109].

GHz.

Table 2.2 compares the proposed inkjet-printed MBs with other SOA coupled-line baluns realized with multilayer processes, e.g. LTCC, MMIC, CMOS, ML PCB. As shown, the proposed MB configurations exhibit small physical size, especially in the spiral case, and competitive RF performance. In particular for the spiral balun, it shows comparable AI and PI with most of the presented approaches (e.g., in [50], [113]) and in some instances its AI, PI, and size are smaller than the SOA (e.g., its AI is smaller than in [3], [78], [120], [121], its PI is smaller than in [3], [120], and its size is smaller

Table 2.2
Performance Comparison with SOA multilayer coupled-line baluns - © IEEE 2024 [109].

Ref.	**f_0 (GHz)**	**Max. Loss (dB)**	**Fractional bandwidth (FBW)**			**Technology**	**Volume (λ_g^3)**
			RL FBW	AI	PI		
[113]	2	0.9	71%**	<0.38 dB	<3.5°	LCP/PCB	0.20 × 0.50 × 0.14
[78]	2.4	1**	24%	<1 dB	<3°	LTCC	N/A
[3]	45	7**	89%	<1.5 dB	<10°	CMOS	0.296 × 0.163 × /
[112]	2	2**	75%**	N/A	N/A	MMIC	0.023 × 0.058 × /
[50]	2.6	2.8	31%	<0.5 dB	<5°	ML PCB	0.51 × 0.77 × 0.01
[120]	1.6	1.3	77%	<1 dB	<10°	LTCC	0.101 × 0.063 × 0.048
[121]	2	1*	93%	<0.9 dB	<1.8°	ML PCB	0.023 × 0.058 × 0.01
[122]	2.45	0.24	16%	<0.1 dB	<1°	LTCC	0.072 × 0.043 × 0.029
Figure 2.15	**4.4**	**3.9#**	**96%**	**<0.9 dB**	**<7°**	**Inkjet AM**	**0.033 × 0.241 × 0.028**
Figure 2.17	**4.4**	**3.1#**	**95%**	**<0.5 dB**	**<7°**	**Inkjet AM**	**0.043 × 0.094 × 0.028**

λ_g: Guided wavelength at f_0; ML: Multilayer; *: Insertion loss at f_0; **: Estimated from graphs/images, /: Measurement not given, #: Includes transition loss

than in [3], [15], [50], [120]) while it exhibits the widest FBW, which is very close to the optimally predicted 99% by the theoretical analysis in Section 2.1.2. Although its loss may appear to be higher than certain integration concepts (e.g., LTCC [78], [120], [122], CMOS [3]), to the best of the authors knowledge, this is the first time that a wideband MB has been implemented monolithically using a two-material inkjet printing process, which demonstrates comparable or even better performance (in terms of FBW) than SOA multilayer processes. Processes which are potentially more expensive, require expensive clean-room manufacturing facilities, and do not facilitate such high levels of design flexibility.

2.3 Conclusions

This chapter presented a detailed design methodology for the practical development of wideband MBs, alongside a unique integration concept using multi-material inkjet printing. An optimization method determining the maximum achievable FBW for alternative RF input/output impedances was proposed for the first time. Several TL-based integration concepts were analysed using 2D and 3D EM simulations taking into consideration the capabilities of a multi-material multilayer inkjet printing process which is used in this work for the realization of MBs for first time. A miniaturization scheme using spiral TLs and slanted vias was also explored for size compactness. To validate this approach, the properties of the inkjet printing process were evaluated through test structures, optical characterization methods and RF testing. Lastly several coupled-line test structures and MBs were designed, manufactured, and tested in resistively-terminated and back-to-back configurations.

3 Compact Multilayer PCB-Based Marchand Baluns With Maximized Fractional Bandwidth

Having validated the design procedures to maximize the FBW of a MB using a multi-material inkjet AM process, in this chapter, these design methodologies are adapted to the best achievable design of planar MBs using a streamlined multi-layer PCB process for comparison purposes. The maximum FBW achievable for a given coupled line structure is described, while the practical validation of the concept is shown through two maximum achievable FBW MBs on a 6-layer ML PCB process using coupled SL and EMS TLs. Finally, a comparison between the realised inkjet AM and ML PCB baluns is provided to give a better understanding of the tradeoffs associated with each approach in terms of area, board thickness, FBW, loss, and design flexibility.

3.1 Theoretical Foundations

3.1.1 Bandwidth limits of various coupled-line types

The planar MB topology in Figure 3.1(a) is now analysed using three different coupled-line geometries, namely MS in Figure 3.1(b), EMS in Figure 3.1(c), and SL in Figure 3.1(d). They are implemented in a 6-layer PCB process with copper layers (orange) having thickness t = 15 μm, trace widths $W \geq$ 50 μm, and trace spacings ≥ 50 μm. The dielectric prepreg (green) and core (blue) layers have thicknesses H_{PP} = 25 μm and H_{Core} = 42 μm, dielectric constants (ε_r) of 3.65 and 4.05, and loss tangents of 0.009 and 0.0075 at 5 GHz, respectively.

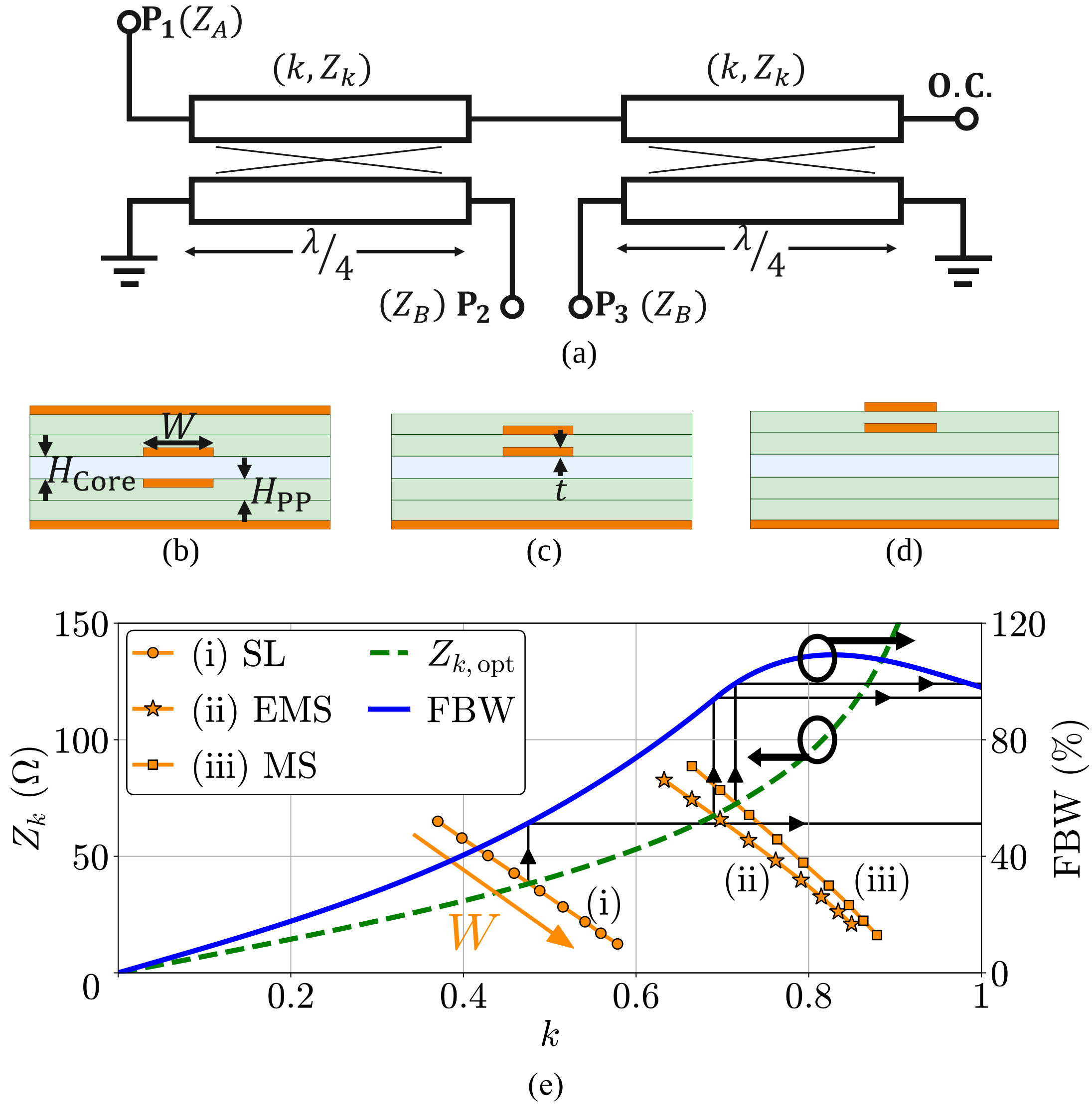

Figure 3.1. (a) Circuit schematic of a planar MB. P_1: Unbalanced port with impedance Z_A. P_2 and P_3: Balanced ports with impedance Z_B. Coupled lines are 90° long at f_0 and have a coupled-line parameters k, Z_k. (b), (c), (d) ML PCB SL, EMS, and MS TLs, respectively. (e) Optimal required Z_k (dashed green line) of the MB for $Z_A = Z_B = 50$ Ω as a function of k using (2.3) and the resultant FBW calculated from (2.4). (k, Z_k) for varying W for stack-ups shown in (b)-(d) and corresponding best achievable FBW for each case.

In choosing the optimal TL configuration, minimum vertical trace-to-trace spacings and maximum trace-to-ground spacings that maximize k and Z_k can be considered. Full 3D EM simulations can be performed to extract their Z_k and k values while varying W from 25–400 µm and are plotted in Figure 3.1(e). As evidenced, k increases when

Table 3.1
Coupled line parameter ranges and best achievable MB FBW for alternative PCB integrated TLs.

Case	k	Z_k (Ω)	W_{opt} (μm)	FBW (%)
(i) PCB SL	0.11 – 0.49	12 – 53	75	55
(ii) PCB EMS	0.18 – 0.77	18 – 65	50	94
(iii) PCB MS	0.19 – 0.80	19 – 75	40	99

Z_k decreases for increasing W, and its corresponding FBW demonstrates the opposite trend to the theoretically calculated FBW(k) relationship in (2.4). Therefore, a single k, Z_k pair for each of the TL structures crosses the optimal k, Z_k curve of the MB which then determines the best achievable FBW (and required W) for a given coupled-line configuration.

Having specified the optimal dimensions, the expected FBW can easily be calculated using (2.4) and is anticipated to be smaller than the theoretical optimum of 109%. **Table 3.1** provides a summary of the maximum FBW and required W_{opt} for all of the three TL configurations. As can be seen, the SL configuration leads to the narrowest FBW of 55% for a W_{opt} = 75 μm, but is the most homogenous, leading to low differences in the odd-mode phase (θ_o) and even-mode phases (θ_e) of the coupled lines, and thus a MB with low AI and PI [117]. The EMS and MS TLs have similar best achievable FBWs of 94% for W_{opt} = 50 μm, and 99% for W_{opt} = 40 μm, respectively. Considering that the MS is the least homogenous coupled-line structure and has a W_{opt} narrower than the process minimum where $W \geq 50$ μm, MBs with EMS and SL TLs were therefore selected to validate the design procedure.

3.1.2 Design of PCB-based Marchand baluns

The 3D EM models and layouts of the SL and EMS-based MBs are shown in Figures 3.2 and 3.3. They have been designed for centre frequencies of 6 GHz and 4.5

GHz, and FBWs of 56% and 91%. Their footprint is miniaturized through geometrical spiralling, leading to an overall device footprint of $L_{SL} \times W_{SL} = 0.0033\ \lambda_g^2$ and $L_{EMS} \times W_{EMS} = 0.0022\ \lambda_g^2$. It should be emphasized that the inhomogeneous mediums and coupled-line spiralling increases the differences between θ_o, θ_e, compromising the AI and PI of the MB. To counteract this effect, the TL parameters (θ_{conn}, Z_{conn}) of the interconnecting line that links the broadside-coupled spirals can be calculated using the same method described in Chapter 2 [16].

As evidenced in Figures 3.2 and 3.3, the required L_{conn} for the EMS balun is longer than the SL case due to its TLs being less homogenous (i.e., having larger θ_o, θ_e differences) causing a shift of the reflection zero to lower frequencies which then requires the coupled line sections to be shortened (in this case, by a length 0.063 λ_g) to counter this effect. The optimized dimensions of the MBs for the SL and the EMS are respectively provided in Figures 3.2, 3.3 and have been obtained with full EM simulations in the software package ANSYS HFSS. Their corresponding EM-simulated performance of the spiralled-line SL and EMS MBs are provided in Figure 3.2(c) and Figure 3.3(c), respectively and are summarized as follows: FBW = 56% (4.6-8.2 GHz) with f_0 = 6 GHz and 91% (3.1-8.2 GHz) with f_0 = 4.5 GHz, where AI = 0.35 dB ± 0.35 dB and 0.2 dB ± 0.2 dB, and PI = 2° ± 1° and 4° ± 1°. As evidenced, the EM-simulated FBWs for both of the MBs are in close agreement with their predicted FBWs of 55% and 94% in **Table 3.1**. The small bandwidth narrowing at higher frequencies is compounded by parasitics and current crowding, introduced by spiralling the coupled lines.

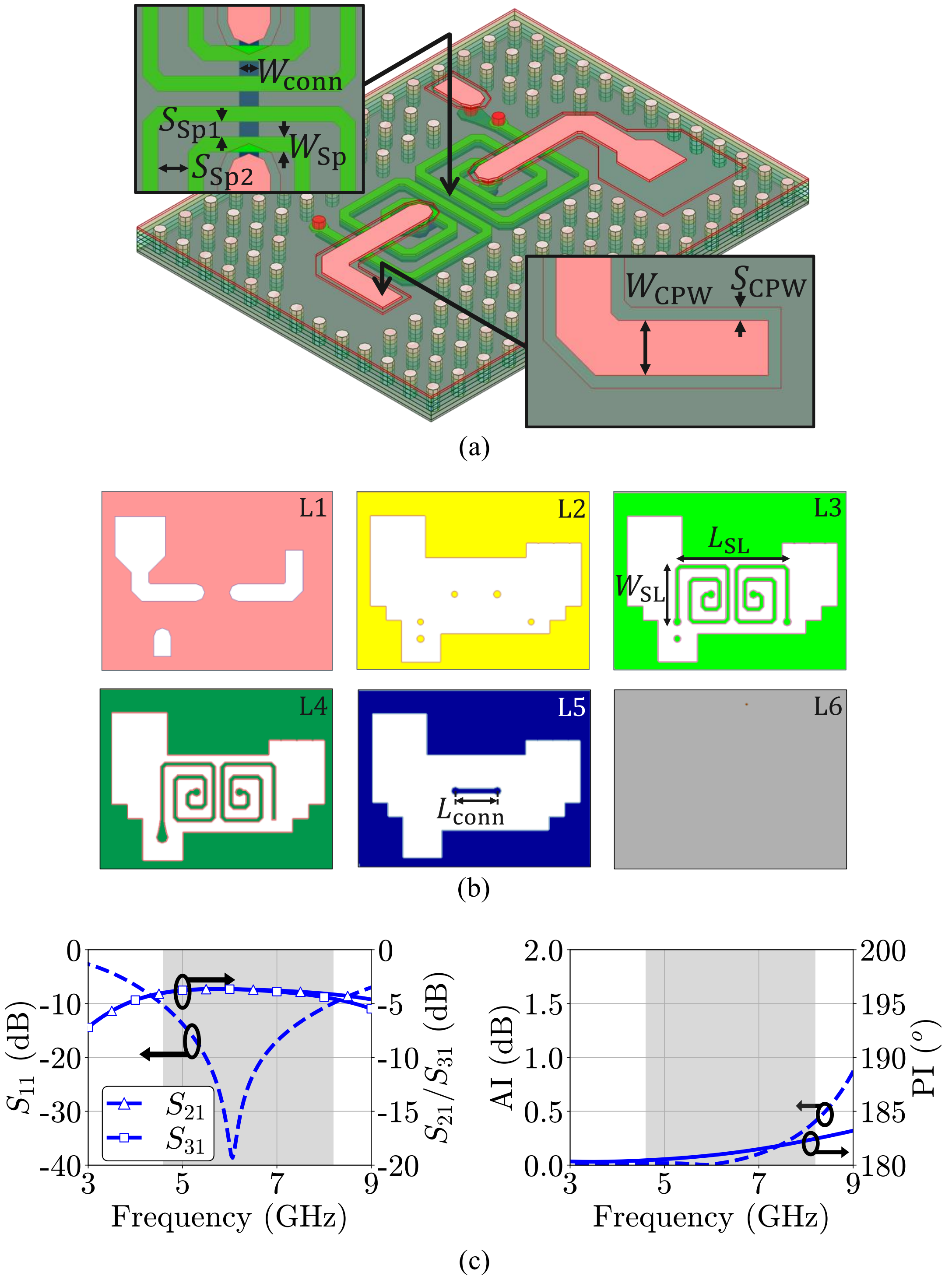

Figure 3.2. (a), (b) 3D geometry of the SL MB and layout of balun over the 6 conductor layers. L_{conn} = 750 μm, W_{conn} = 95 μm, W_{SP1} = 75 μm, S_{SP1} = 75 μm, S_{SP2} = 150 μm, L_{SL} = 2100 μm, W_{SL} = 1080 μm, W_{CPW} = 220 μm, and S_{CPW} = 50 μm. (b) EM-simulated S-parameters, AI, and PI.

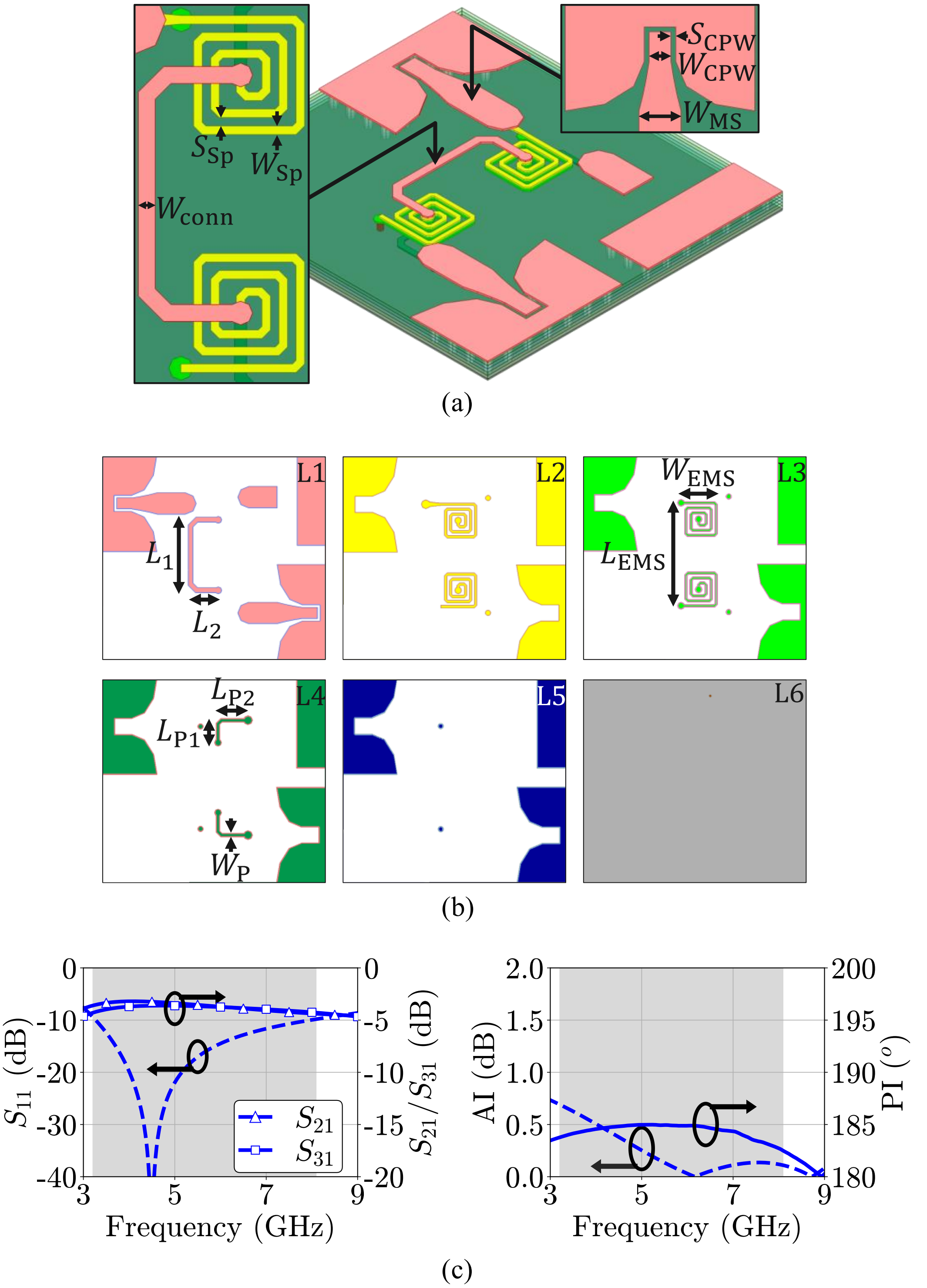

Figure 3.3. (a), (b) 3D geometry and layout of the EMS MB. W_{conn} = 100 µm, W_{SP} = 50 µm, S_{SP} = 50 µm, L_{EMS} = 2190 µm, W_{EMS} = 810 µm, L_1 = 1400 µm, L_2 = 550 µm, W_P = 70 µm, L_{P1} = 450 µm, L_{P2} = 600 µm, W_{MS} = 425 µm, W_{CPW} = 220 µm, and S_{CPW} = 50 µm. (b) EM-simulated S-parameters, AI, and PI.

3.2 Experimental Validation

3.2.1 Coupled-line test structures

To characterise the broadside coupled-line quality, all-pass SL and EMS coupled TL test structures of the circuit element in Figure 3.4(a) were designed and measured as shown in Figure 3.4(b)-(g). The same trace widths W_{opt} of the respective SL and EMS baluns were used in each case. 50 Ω GCPW terminations were designed to facilitate 250 μm GSG probe-based characterization measurements. Excellent agreement is seen between simulation and measurement as shown in Figure 3.4(f), (g), indicating good coupled-line quality. A spur in the EMS test structure can be seen in Figure 3.4(g). The reason for this can be seen in Figure 3.4(e), where an additional metal structure that is circled in red has introduced a resonance in the coupled line structure at 5.5 GHz, causing the spurious peak. This additional metal structure – which was part of another test device – was placed too close to the coupled line structure due to layout constraints in the fixed area reticules sent for fabrication.

3.2.2 EMS and SL spiral baluns

The SL and EMS MBs were manufactured and tested to validate the design concept. The photographs of the SL and EMS Baluns A and B are provided in Figure 3.5(a) and Figure 3.6(a). The EM-simulations and RF-measured S-parameters, AI, and PI are provided in Figure 3.5(b) and Figure 3.6(b). For the SL and EMS designs, the measured FBWs were 56% with f_0 = 6.1 GHz and 71% with f_0 = 4.3 GHz, respectively. Across these BWs, the measured power loss, PI, and AI were measured between 0.8-1.5 dB and 1-2.2 dB, 2 ± 2° and 6.5 ± 1°, and 0.35 ± 0.35 dB and 0.45 ± 0.45 dB, respectively. A very good FBW agreement is obtained for the SL balun while there is FBW narrowing on the right edge of the passband for the EMS balun. Despite this BW

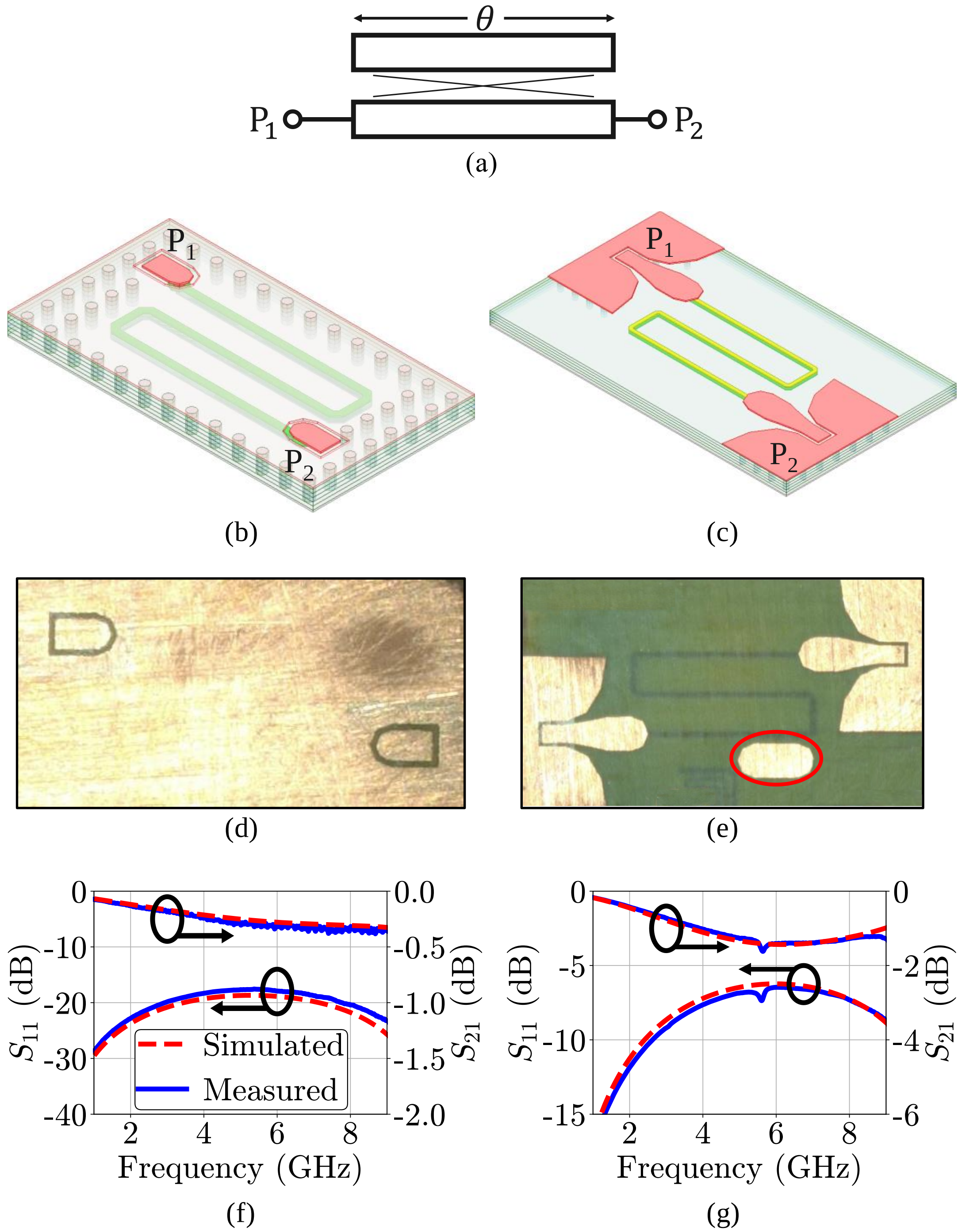

Figure 3.4. Characterization of SL and EMS broadside-coupled TLs. (a) All pass coupled-line structure. (b), (d), (f) 3D model, optical photograph, and EM-simulated and RF-measured S-parameters of the SL-coupled TLs where $W = 75$ μm and $\theta = 90°$ at 6 GHz. (c), (e), (g) Respective images for EMS-coupled TLs where $W = 50$ μm and $\theta = 90°$ at 6 GHz.

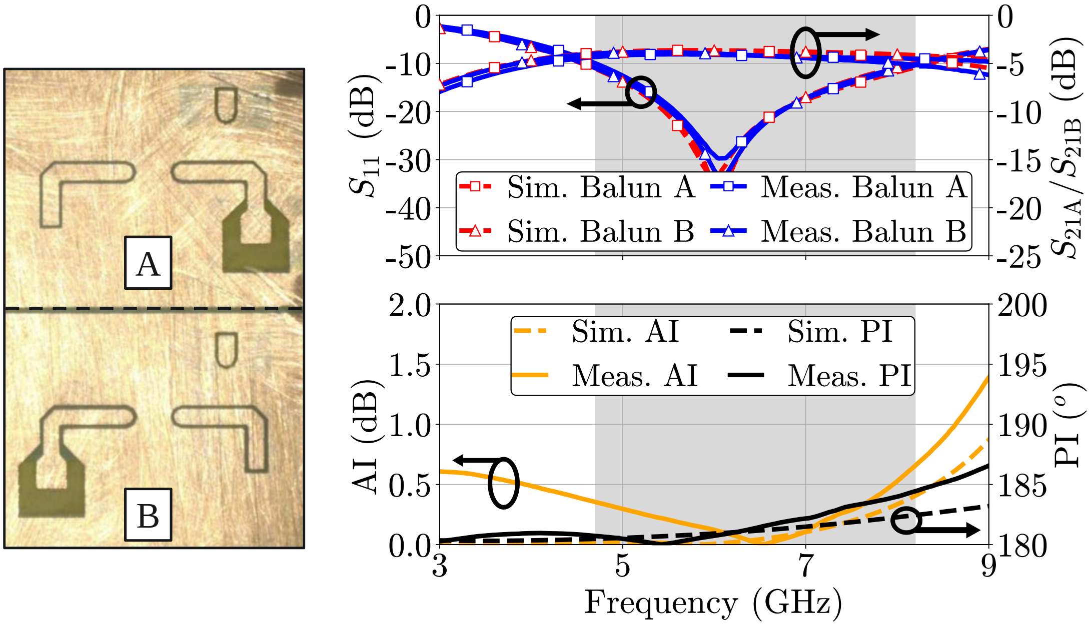

(a) (b)

Figure 3.5. (a) Optical image of the manufactured SL Balun A and B. (b) EM-simulated and RF-measured S-parameters (top) of the two resistively-terminated baluns (Balun A: Corresponding to S_{21A}, Balun B: Corresponding to S_{21B}) and EM-simulated and RF-measured AI and PI (bottom). Grey area: operational BW.

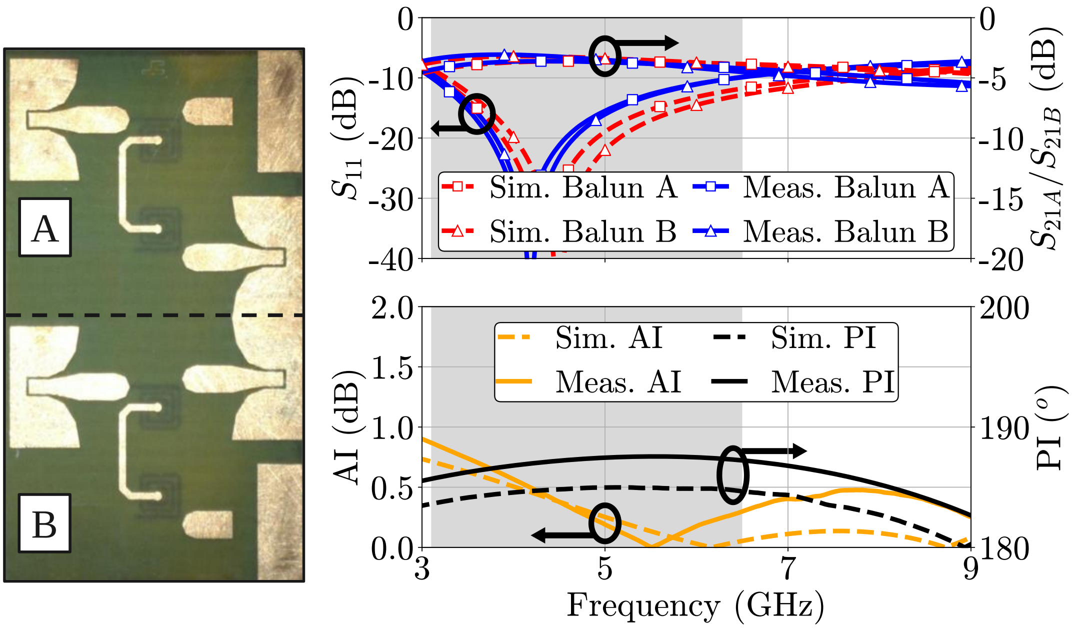

(a) (b)

Figure 3.6. (a) Optical image of the manufactured EMS Balun A and B (b) EM-simulated and RF-measured S-parameters (top) and AI and PI (bottom). Grey area: operational BW.

Table 3.2
State-of-the-art Marchand baluns on multilayer processes.

Ref.	**f_0 (GHz)**	**Max. Loss (dB)**	**FBW (%)**	**AI (dB)**	**PI (°)**	**Technology**	**Area (λ_g^2)**
[3]	60	7*	89	<1.5	<10	CMOS	0.048
[46]	1.6	1.3	77	<1	<10	LTCC	0.0063
[47]	23	2.9	77	<2	<10	CMOS	0.0037
[48]	45	1.2	74	<0.7	<1.2	MMIC	0.0348
[49]	2	0.9	71*	<0.38	<3.5	LCP/PCB	0.1
[50]	2.45	0.24	16	<0.1	<1	LTCC	0.0031
[74]	2.4	1**	24	<1	<3	LTCC	<0.003**
SL balun	**6**	**2**	**55**	**<0.7**	**<4**	**ML PCB**	**0.0033**
EMS balun	**4.8**	**1.5**	**71**	**<0.8**	**<7.5**	**ML PCB**	**0.0022**

λ_g: Guided wavelength at f_0; ML: Multilayer; *: Estimated from graphs/images

narrowing, a very good agreement is obtained with the EM simulations, successfully validating the proposed FBW optimization concept.

Table 3.2 compares the proposed SL and EMS MBs with other SOA coupled-line baluns realized with multilayer processes, e.g., LTCC, CMOS, ML PCB. As shown, both of the proposed MB configurations exhibit small physical size, with only [74] exhibiting slightly smaller footprint, however having a considerably narrower BW than the proposed concepts. In cases where a larger FBW has been achieved (e.g., in [3], [48]) their size is about 15-22x larger than in the proposed configuration which also has lower while AI, PI and loss.

3.3 Comparison of Inkjet AM and PCB Processes

In order to compare the performance of baluns implemented on PCB and using an inkjet AM process in Chapter 2, the miniaturised SL baluns, which were both designed to maximise FBW in their respective processes are compared across all important balun metrics using manufactured balun implementations as shown in Figure 3.7.

1. Achievable FBW: The inkjet AM approach demonstrated wider achievable BWs for SL TLs compared to the ML PCB case, as evidenced in Figure 3.7(a), where the back-to-back inkjet AM implementation covers a wider BW (2.3-8.4 GHz or FBW = 114%) compared to the back-to-back PCB implementation balun (4.3-8.4 GHz or FBW = 64%). The inkjet AM implementation therefore has benefits of excellent AI and PI, enabled by the SL TLs, while offering much wider BWs compared to the PCB implementation.
2. Footprint: The footprints of the SL inkjet AM and PCB baluns were 0.0043 λ_g^2 (blue areas in Figure 3.7(b)) and 0.0033 λ_g^2 (red areas in Figure 3.7(b)), respectively. The 30% reduction in footprint in the PCB balun compared to the inkjet AM balun is due to the thinner coupled-line widths in the PCB balun (W = 75 μm) allowing for a tighter spiral and thus reduced footprint compared to the inkjet AM case which requires a wider trace width W = 115 μm. Although the PCB approach does produce a lower footprint, both spiral MBs offer significant miniaturization with footprints comparable with the SOA (<0.005 λ_g^2) in miniaturised baluns.
3. Board Thickness: The overall AM board thickness H_{AM} = 1050 μm is four times larger compared to the overall PCB thickness of H_{PCB} = 262 μm, as illustrated in Figure 3.7(c), allowing for the enhanced coupled-line parameters achieved in the inkjet AM case. Increasing board thickness allows for a higher k in the inkjet AM case, even though the PCB layer thicknenesses (25 and 42 μm for prepreg and core layers, respectively) are smaller than the minimum vertical spacings of 50 μm allowed in the inkjet AM process. The ability to

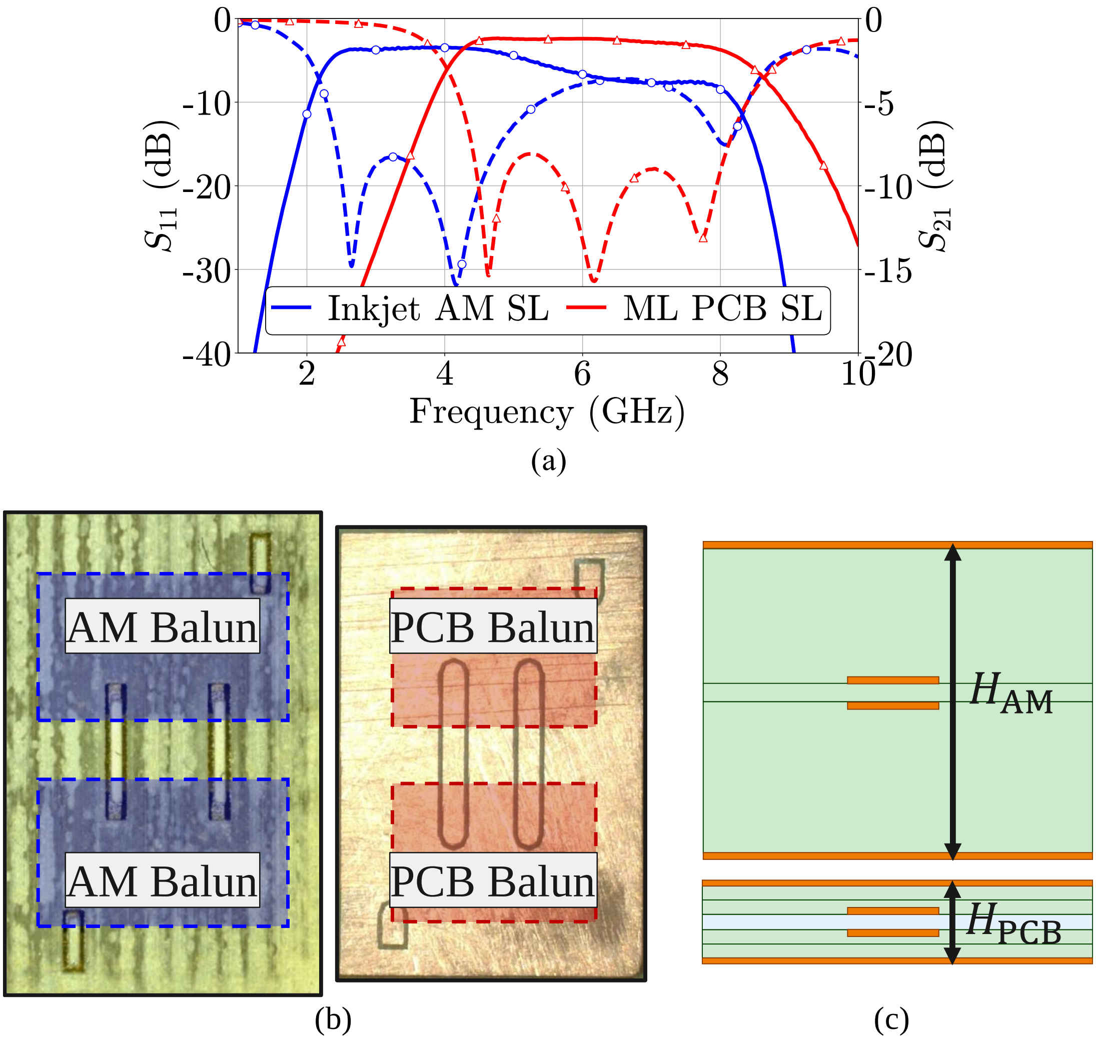

Figure 3.7. (a) Measured S-parameters of inkjet AM- (blue) and PCB-based (red) SL back-to-back baluns. (b) Optical photographs of the PCB (red) and AM (blue) SL back-to-back baluns. (c) Illustration of board thicknesses of AM- (top) and PCB-based (bottom) SL coupled lines.

enhance FBW by freely increasing in vertical height rather than footprint is a key advantage to the inkjet AM process.

4. Loss: The PCB process indeed offers lower loss compared to the inkjet AM process, where 2 dB of loss is measured at its $f_0 = 4.4$ GHz, while the ML PCB process gives 1.5 dB of loss at its $f_0 = 6$ GHz, as can be seen in Fugure 3.7 (a). There are two key material paramters which cause this difference in losses. Firstly, the inkjet DI has an approximately 3x higher loss tangent of 0.023

compared to the PCB dielectrics having 0.0075 and 0.009 for prepreg and core layers, respectively. There is therefore inovation required in DI development to reduce dielectric loss tangent values found in standard commercial PCB processes. The key material parameter causing the large losees in the AM baluns is the low conductivity of the CI used in the inkjet AM process (σ = 1.8×10^6 S/m) compared to the high conductivity copper layers (σ = 5.7×10^7 S/m) in the PCB process. This is a current drawback to inkjet AM and the development of higher conducitvity CIs is a key area needing improvement in inkjet AM manufacturing. The high power losses are therefore clearly the greatest disadvantage to the proposed design method compared to other approaches. The high material losses would pose a particular disadvantage to narrowband design, where lower couplings, and inherently higher insertion losses further degrade the baluns' power transmission. Therefore, this design approach is currently most suitable for wideband design.

5. Design Flexibility: It has been demonstrated that inkjet AM offers design freedoms not offered by other discrete multilayer processes, such as 3D traces, allowing for signals to be routed through various layers with minimual reflections, and continuously variable layer thicknesses, allowing for a greater range of coupled-line parameters to be selected. Considering these design capabilities, it is evident that inkjet AM offers potential to allow for enhanced balun performace compared to conventional multilayer processes.

3.4 Conclusion

This chapter reported on a detailed design methodology for the realisation of the best achievable FBW response for broadside coupled MBs on ML PCB processes. A simulation-based method determining the maximum achievable FBW considering a process' limits was reported. A SL and EMS balun was designed using a 6-layer PCB process, demonstrating their simplicity in design, wide BWs and very small footprints compared to other balun design approaches. Finally, a comparison between MBs designed using the ML PCB process and the inkjet AM process described in Chapter 2 was included. This comparison motivates further research into compact wideband, and multifunctional baluns integrated using inkjet AM, exploiting the various design freedoms associated with this novel two-material process.

4 Inkjet-Printed Capacitively-Loaded Marchand Baluns with Enhanced Fractional Bandwidths

In chapter 2, it was shown that the MB topology has a maximum FBW of 109% when using a 1:1 impedance transformation, while requiring coupled-line parameters generally out of reach of conventional processes. It was demonstrated that inkjet AM has the capability of reaching this FBW limit, but there is a need for topologies that can produce larger FBWs than this maximum for achievable coupled-line parameters. *C*-loading techniques have been shown to enhance MB performance in several areas including phase compensation, miniaturization, and frequency tunability [67], [69], [73], [74]. However, no research found in the open technical literature has explored FBW maximising procedures using *C*-loaded MB topologies. Considering the FBW limitations of the MB, this chapter presents: i) a comprehensive design methodology for *C*-loaded MBs with maximized FBW and highly-miniaturized footprint, ii) the potential of the two-material inkjet printing process in realizing *C*-loaded tightly-coupled TLs and 3D vertically integrated capacitor integration that can be exploited for miniaturization, iii) a FBW enhancement technique using a patterned ground plane.

4.1 Theoretical Foundations

4.1.1 Capacitively-loaded planar MBs

The conventional planar MB circuit-schematic, whose design has been described in Chapters 2 and 3, is shown in Figure 4.1(a), with 50 Ω port impedances for P_1, P_2, and P_3 considered as before. FBW enhancement and footprint miniaturization of the

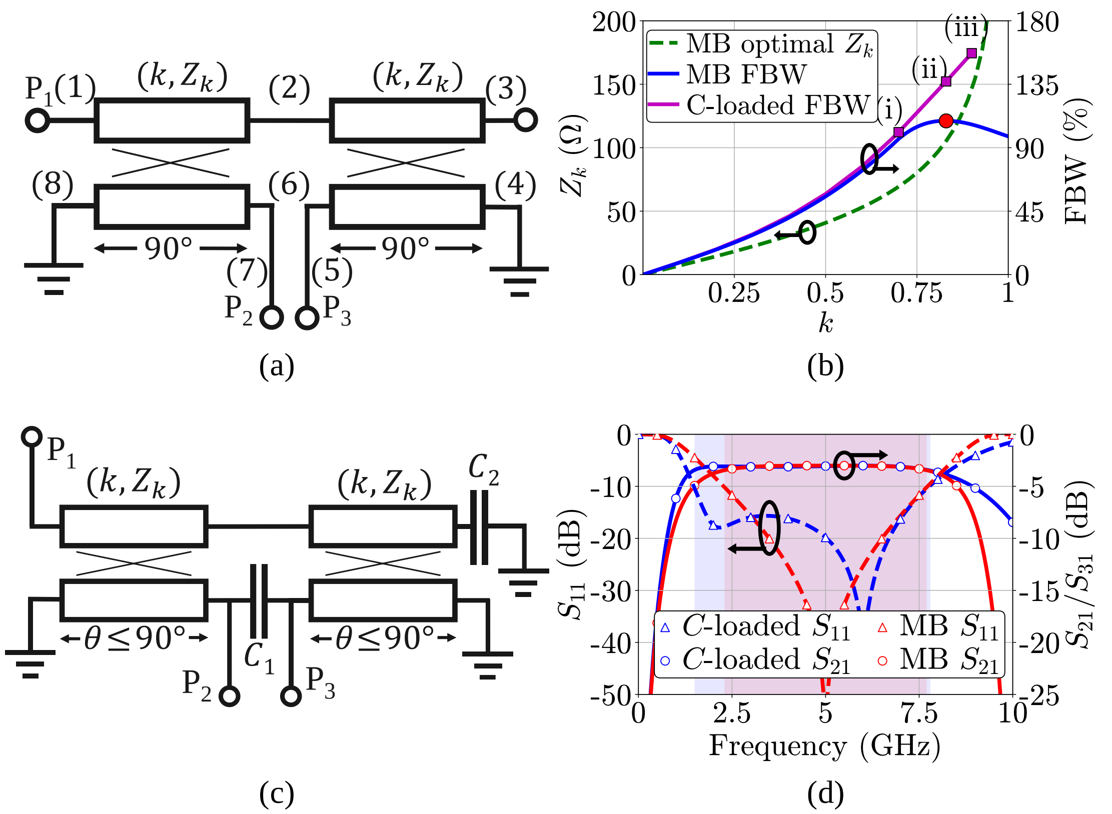

Figure 4.1. (a) Circuit-schematic of the conventional MB with possible series capacitor locations (1)-(8). (b) Optimal (S_{11} = 0 at f_0) (k, Z_k) curve and corresponding FBW as a function of k for the MB topology. Maximum FBW as a function of k for the C-loaded MB topology. (b) C-loaded MB with series capacitors C_1 and C_2 at (6) and (3) and coupled lines with electrical length θ. (d) Red: Maximum FBW S-parameter response for the conventional MB where FBW = 109% for k = 0.83, Z_k = 105 Ω. Blue: Maximum FBW S-parameter response of C-loaded MB under the condition that $k \leq$ 0.83 with FBW = 137%, k = 0.83, Z_k = 90 Ω, C_1 = 0.23 pF, C_2 = 1.8 pF, and θ = 40°.

MB can be achieved by loading the MB capacitively. As such, one and two capacitor topologies with series capacitors, C_1 and C_2, at locations (1)-(8) can be considered as shown in Figure 4.1(a). Overall, there are ‘8 choose 2’ = 28 variations. Each topology was optimized to maximise FBW by freely varying k, Z_k, C_1, C_2, and θ, quickly allowing for the best performing topologies to be identified. The locations (3) and (6), namely with C_1 between P_2 and P_3 and C_2 at the open end of P_1 as shown in Figure 4.1(d) gave the largest maximum FBW in this study and is considered hereon. For this topology, example maximum FBWs are plotted in Figure 4.1(b) for k = (i) 0.7, (ii) 0.83, and (iii) 0.9. As it can be seen FBW increases with k and has similar maximum FBW to the MB up to $k = 0.7$ where $Z_k = 71\ \Omega$, $\theta = 56$, $C_1 = 0.21$ pF, and $C_2 = 0.80$ pF, corresponding to maximum FBW = 102%. For large k, the topology can achieve considerably wider maximum FBWs. A FBW = 137% is achievable using the MB's optimal $k = 0.83$ with $Z_k = 90\ \Omega$, $\theta = 40°$, $C_1 = 0.23$ pF, and $C_2 = 1.8$ pF, its corresponding S-parameters are also provided in Figure 4.1(d) alongside maximum 137% FBW MB response. The FBW continues to increase with k with a maximum FBW = 157% for $k = 0.9$, $Z_k = 130\ \Omega$, $\theta = 33°$, $C_1 = 0.22$ pF, and $C_2 = 2$ pF. The high coupling region $k > 0.7$ is therefore the main region of interest. Additionally, θ is significantly reduced compared to the MB, enhancing miniaturization, and reducing loss. Considering wide FBWs require large k, Z_k, maximum FBW is determined by the integration process' capabilities in realising large k, Z_k. Understanding the achievable coupled-line parameters is therefore crucial to determine maximum achievable FBW.

4.1.2 Coupled-line and parameter selection

To achieve large k and Z_k, a broadside-coupled EMS TL integration scheme is explored using a multilayer two-material inkjet AM process as shown in Figure 4.2(a). As such, a wide range of k, Z_k can be obtained using full EM simulations in ANSYS HFSS [116]. To explore the FBW capabilities based on the achievable k and Z_k, the C_1, C_2, and θ parameters were optimised to maximise average FBW over the wide FBW range $0.7 < k < 0.9$. This optimization produced $\theta = 45°$, $C_1 = 0.25$ pF, and $C_2 = 1$ pF. To demonstrate the achievable FBW as a function of k, Z_k, a parametric study in steps of $\Delta k = 0.01$, $\Delta Z_k = 2\ \Omega$ was performed, and 10 dB FBWs extracted, producing the heat map shown in Figure 4.2(c), on top of which the achievable EMS k, Z_k range is plotted with white dashed lines. Three response regimes are seen. In the black region

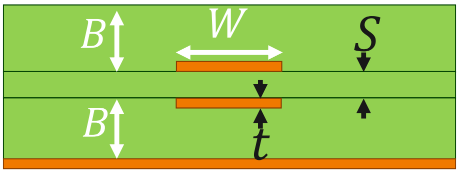

(a)

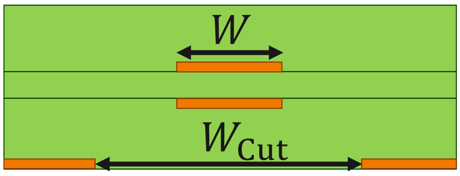

(b)

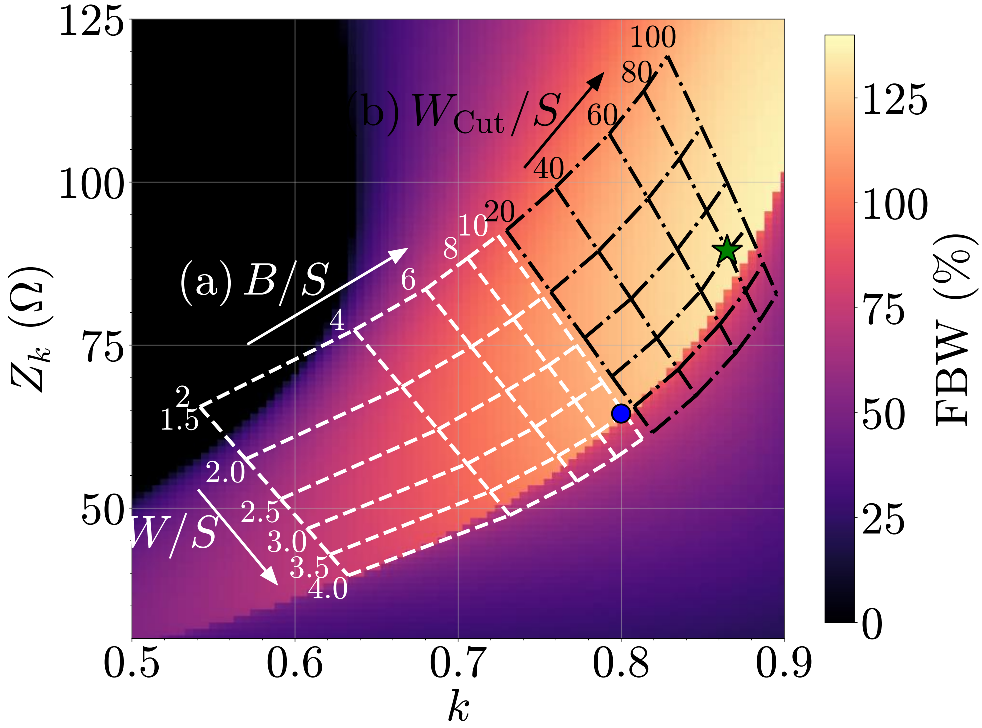

(c)

Figure 4.2. (a) Broadside-coupled EMS with a solid ground plane. (b) EMS with perforated grounded plane (W_{Cut} is the width of the perforation). (c) Heatmap of FBW over the (k, Z_k) parameter space for $\theta = 45°$, $C_1 = 0.25$ pF, and $C_2 = 1$ pF. Furthermore, the Z_k and k of the EMS is overlaid as a function of W/S and B/S for $W_{\mathrm{Cut}} = 0$, and as a function of W/S and W_{Cut}/S for $B/S = 10$.

responses have no 10 dB passband, i.e., FBW = 0%. In the central region there is a large k, Z_k range greater than the optimal planar MB FBW = 109%, as desired. In the lower-right region, marked off by a sharp boundary, matching is worse than 10 dB within the band, significantly diminishing FBW. Choosing a k, Z_k pair too close to this region is avoided to improve matching at f_0. It is evident that for $\theta = 45°$, $C_1 = 0.25$ pF, $C_2 = 1$ pF the realisable k, Z_k range covers the wide BW region, where there is a large range where FBW > 109%. As shown, a k between 0.53 and 0.82 can be obtained, leading to C-loaded baluns with FBWs from 0-113%.

4.1.3 Coupled-line enhancement with patterned ground planes

For a fixed conductor-to-ground distance (here, B = 500 µm), k and Z_k can be enhanced further using a patterned ground plane beneath the EMS as shown in Figure 4.2 (width: W_{Cut} in Figure 4.2(b)). The range of achievable k, Z_k are plotted in grey dot-dash lines in Figure 4.2(c). In this case, a significantly higher k between 0.73 and 0.89 can be obtained, leading to C-loaded baluns with FBWs from 70-133%. Thus, the perforated ground-plane EMS approach will be used for the realization of the proposed MB configuration. The TL parameters were selected to be W = 160 µm, B = 500 µm, and W_{Cut} = 4000 µm (green star in Figure 4.2(c)) to facilitate the realization of a FBW of 131% which is significantly higher than what can be obtained in conventional MBs

4.1.4 3D integrated interdigital capacitors

A crucial parameter in the implementation of the C-loaded MB is the realization of the large capacitance C_2 = 1 pF. If using a standard parallel plate capacitor like the one shown in Figure 4.3(a), large footprints ≈ 2 mm^2 when using the process minimum vertical spacing S = 50 µm are required. To decrease the required area needed to realise 1 pF capacitance, vertically-integrated interdigital plate configurations were designed as shown in in Figure 4.3(b) for the case of an 8-layer capacitor having an area A = $L_{\mathrm{Cap}} \times W_{\mathrm{Cap}}$. The capacitance as a function of area for the proposed capacitor in 4-layer and 8-layer vertical-integration fashion is compared with the case of a parallel plate capacitor in Figure 4.3(c). As evidenced, the vertically-integrated 3D capacitors result in a much smaller footprint (i.e., 0.22 mm^2 for a C = 1 pF). The required C_1 = 0.25 pF can be obtained for L_{Cap} = 400 µm and W_{Cap} = 300 µm when using 4 inter-digital

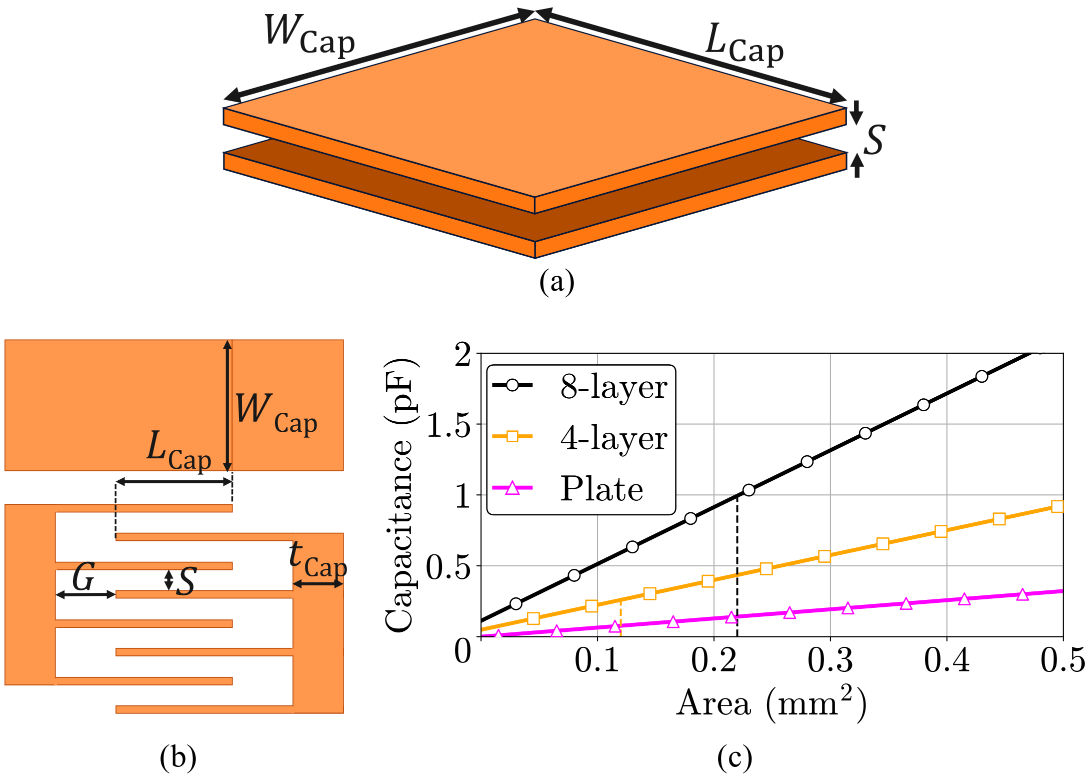

Figure 4.3. Vertically-integrated interdigital capacitors in the inkjet two-material AM process. (a) Illustration of a parallel plate capacitor with side lengths L_{Cap} and W_{Cap}, and vertical plate-to-plate spacing S. (b) Top view and side view of a capacitor having 8 vertically-integrated inter-digital fingers, for $t_{\mathrm{Cap}} = 70$ µm, $S = 50$ µm, and $G = 100$ µm. (c) Capacitance of a 4-layer interdigital (C_1), 8-layer interdigital (C_2), and parallel plate capacitors as a function of occupied area.

fingers, while the required $C_2 = 1$ pF can be obtained for $L_{\mathrm{Cap}} = 385$ µm and $W_{\mathrm{Cap}} = 700$ µm using 8 interdigital fingers.

4.1.5 C-loaded MB design

Based on the aforementioned design guidelines, the C-loaded MB can be designed using full-wave EM simulations and is shown in Figure 4.4(a). Straight coupled-line sections are used and are folded side-by-side for size compactness, leading to an overall footprint of 6.0 × 4.3 mm^2. The inter-connecting line (dimensions W_{conn} and L_{conn}) is carefully designed to optimise AI and PI throughout the required FBW using the design method in [16]. The patterned ground-plane width (W_{Patt}) was optimised to

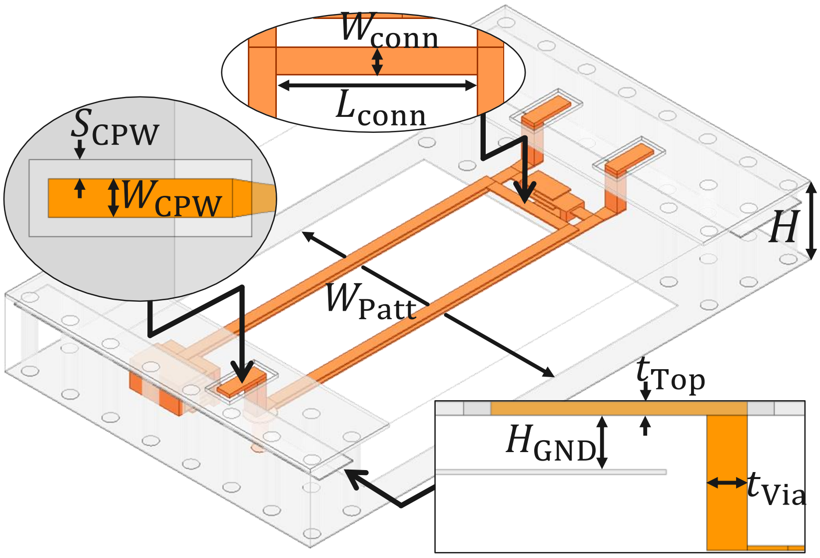

(a)

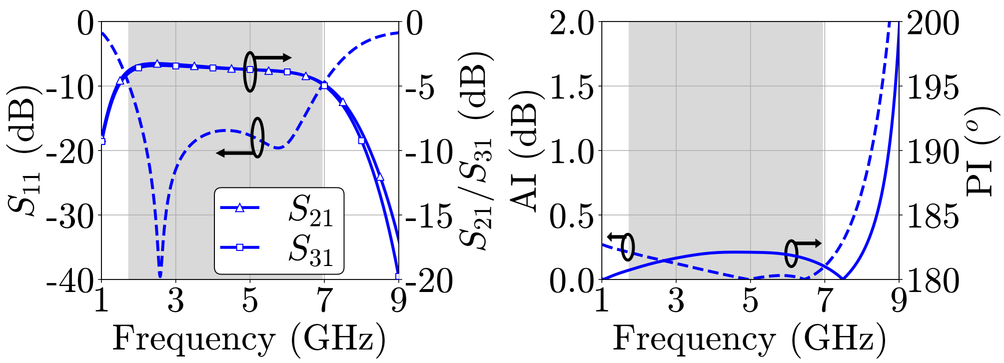

(b)

Figure 4.4. (a) 3D geometry of the *C*-loaded MB. L_{conn} = 1200 µm, W_{conn} = 160 µm, W_{Patt} = 4300 µm, W_{CPW} = 200 µm, S_{CPW} = 100 µm, H_{GND} = 187 µm, t_{Top} = 50 µm, t_{Via} = 150 µm, and $H = 2B + S + t + t_{Top}$ = 1117 µm. (b) EM-simulated S-parameters, AI, and PI.

4300 µm which is slightly larger than W_{Cut} = 4000 µm to compensate for the induced asymmetry from the inter-connecting line. The RF signal is connected to the balun using three 90° 3D vias. Furthermore, vias connect the bottom ground with the top plane, used for the GCPW of the RF input/output ports. Setting W_{CPW} = 200 µm, S_{CPW} = 100 µm, a 50 Ω impedance is precisely obtained by continuously varying H_{GND} =

187 μm. The balun exhibits the following RF performance characteristics: FBW = 123%, loss < 1.5 dB, AI < 0.22 dB, and PI < 2.3° throughout this BW. The narrowed FBW compared to the ideally-predicted 131% in Section 4.1.3 is to be expected considering the added parasitics from the required junctions and bends in the realistic prototype.

4.2 Experimental Validation

The *C*-loaded MB was manufactured using the two-material inkjet process in [100] and subsequently tested with an Agilent E5071C VNA network analyser. Two resistively-terminated prototypes: i) Balun A (P_3 is resistively-terminated) and ii) Balun B (P_2 is resistively-terminated) were manufactured. An X-ray and an optical photograph of an example manufactured prototype (Balun A) is provided in Figure 4.5(a). Its EM-simulated and RF-measured performance in terms of S-parameters, AI and PI are provided in Figure 4.5(b). Specifically, its measured performance is summarized as follows: f_0 = 4.4 and FBW of 121%, where over this BW, the measured power loss is between 0.8-2.2 dB, the PI is 3 ± 2°, and the AI is 0.4 ± 0.4 dB. As observed, a very good agreement is obtained with the EM simulations, successfully validating the proposed MB concept with miniaturized size and ultra-wide FBW characteristics. The measured PI and AI being slightly higher EM simulations is to be expected and is due to the AI and PI being calculated between two different prototypes (i.e., Balun A and Balun B), which are slightly different to one another due to process variations.

Table 4.1 compares the inkjet-printed *C*-loaded MB with SOA *C*-loaded MB variants. As it can be seen, the proposed configuration exhibits the widest FBW, which is 3.3-12 times larger than the ones obtained in [73], [74], [77], [78], [123], while

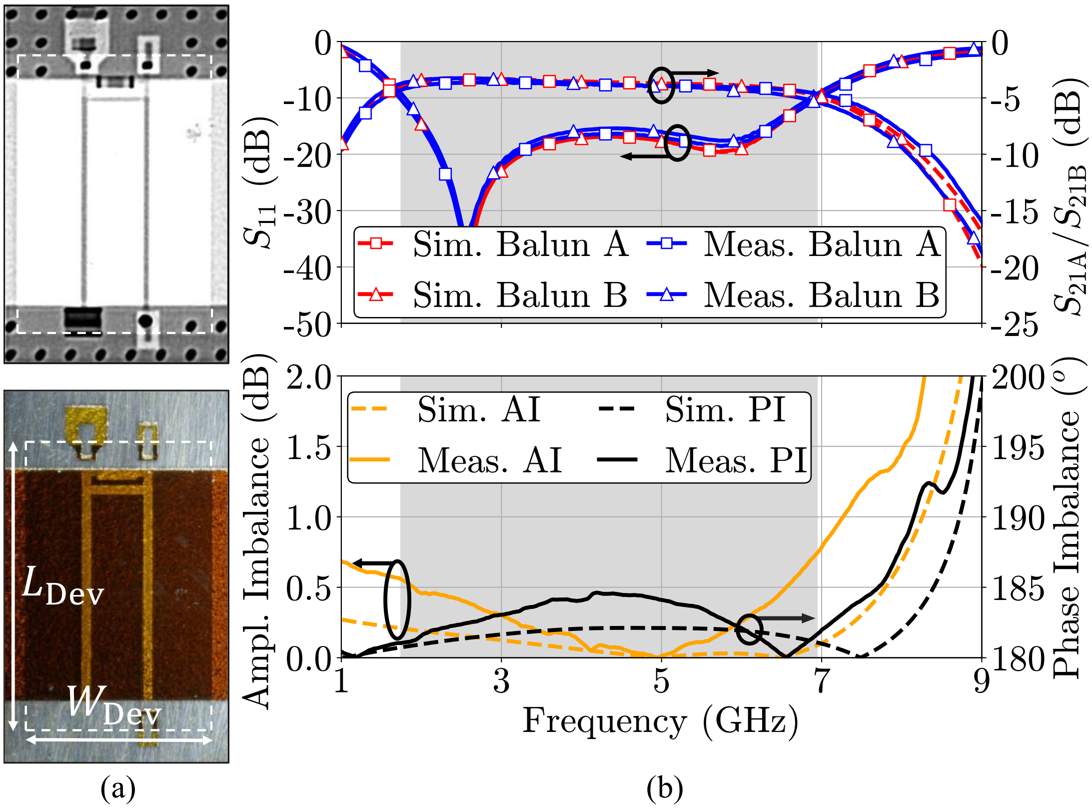

Figure 4.5. (a) Optical and X-ray images of the manufactured C-loaded Balun A (P_3 is 50 Ω terminated) where W_{Dev} = 4.3 mm, L_{Dev} = 6.0 mm. (b) EM-simulated and RF-measured S-parameters (top) of the two resistively-terminated baluns (Balun A: Corresponding to $S_{21\text{A}}$, Balun B: Corresponding to $S_{21\text{B}}$) and EM-simulated and RF-measured AI and PI (bottom). Grey area: operational BW.

achieving comparable footprint, AI, and PI. Furthermore, it exhibits significantly higher operational frequency and the 3D integration using a two-material inkjet printing process is presented in this work for the first time.

4.3 Conclusion

This chapter presented a detailed design methodology for the realisation of wideband and highly-miniaturized C-loaded MBs, alongside a unique integration concept using multi-material inkjet printing. A simulation-based method determining the maximum achievable FBW (~130%) and the characteristics of inkjet-printed

Table 4.1
Comparison with SOA C-loaded MBs

Ref.	**f_0 (GHz)**	**Max. Loss (dB)**	**FBW (%)**	**AI (dB)**	**PI (°)**	**Technology**	**Area (λ_g^2)**
[73]	2.4	1*	24	<1	<3	LTCC	<0.003**
[74]	0.55	1.2	29	<0.3	<3	PCB	0.009
[77]	2.45	1	16	<0.5	<2.6	LTCC	0.003
[78]	1.4	1.2*	37	<0.5	<5	PCB	0.01
[123]	2.1	1.6	12	<0.2	<2	PCB	<0.08**
This work	**4.4**	**2.2**	**121**	**<0.8**	**<4.5**	**Inkjet AM**	**0.013**

λ_g: Guided wavelength at f_0; *: Estimated from graphs; **: Estimated from images

broadside-coupled lines and 3D vertically-integrated capacitors were reported. A wideband MB was designed and tested at C-band demonstrating the widest reported C-loaded MB FBW to date enabled by a low cost and highly-versatile inkjet printing 3D integration concept.

5 Inkjet-Printed Vertically-Integrated RF Co-designed Bandpass Filtering Baluns

This chapter seeks to address the challenge of multi-functionality in emerging RF front-ends that will rely heavily on the realization of RF components with multi-functional capabilities. Specifically, due to the immense need for frequency selectivity in the RF front-end, this chapter explores the potential to incorporate bandpass filtering into the MB by exploiting the resonant behaviour of its quarter-wavelength lines and cascading them with additional coupled-line resonators to enhance frequency selectivity. Specifically, this chapter reports on: i) a new design methodology for the realization of highly-miniaturized BPF-Bs with scalable selectivity and form factor, and ii) a novel integration scheme using vertically-integrated broadside-coupled TLs that can be exploited to introduce transfer function versatility in terms of transfer function order and realizable BW.

5.1 Theoretical Foundations

5.1.1 RF co-designed bandpass filtering baluns

The circuit schematic of the BPF-B concept is illustrated in Figure 5.1 for the case of even- (Figure 5.1(a)) and odd-order (Figure 5.1(b)) transfer functions (TFs). It is based on a cascaded planar MB topology − first proposed in [60] but not treated using filter synthesis − allowing for higher order filtering TFs in each of its output ports P_2 and P_3. Considering that a planar MB consists of an OC $\lambda_g/2$ TL (at centre frequency f_0) coupled to two SC $\lambda_g/4$ TLs, its TF can be like the one obtained by a narrowband 2^{nd}-order ($N = 2$) coupled resonator BPF [14]. To increase the TF order, additional SC

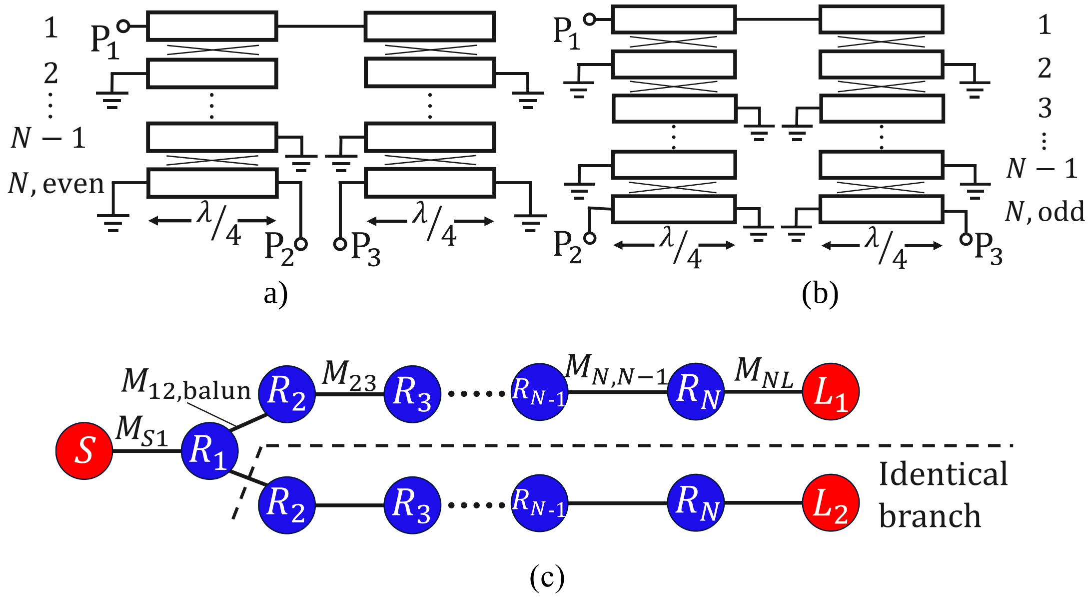

Figure 5.1. Multi-coupled TL-based BPF-B. (a) Circuit-schematic for even-order transfer functions. (b) Circuit-schematic for odd-order transfer functions. (c) Equivalent CRD for (a) and (b).

$\lambda/4$ TLs are coupled to the conventional MB as shown in Figure 5.1 (a), (b), where the only difference between the realization of odd- and even-order TFs is the locations of P_2 and P_3. The equivalent coupling routing diagram (CRD) for an N^{th}-order TF is shown in Figure 5.1(c), where P_1 is the source S, and P_2 and P_3 are loads L_1 and L_2.

To demonstrate the operating principles of the BPF-B concept, a 3rd-order topology (N=3 in Figure 5.1(b)) is considered in Figure 5.2(a), (b), where two alternative external coupling schemes are considered: Input/output (I/O) feeding lines (a) coupled capacitively to the resonators and (b) directly coupled to the resonators. These facilitate high and low external coupling strengths Q_e that are then more suitable for wideband (WB) and ultra-wideband (UWB) TFs, respectively. Figure 5.2(a) is therefore referred to as the WB BPF-B topology and Figure 5.2(b) is referred to as the UWB BPF-B topology. Since the two output branches split the output power equally, the design of the BPF-B can be performed by using the two-port CRD equivalent in Figure 5.2(c), whose coupling coefficients $M_{S1} = M_{NL} \equiv M_{I/O}$, M_{12} and M_{23} can be

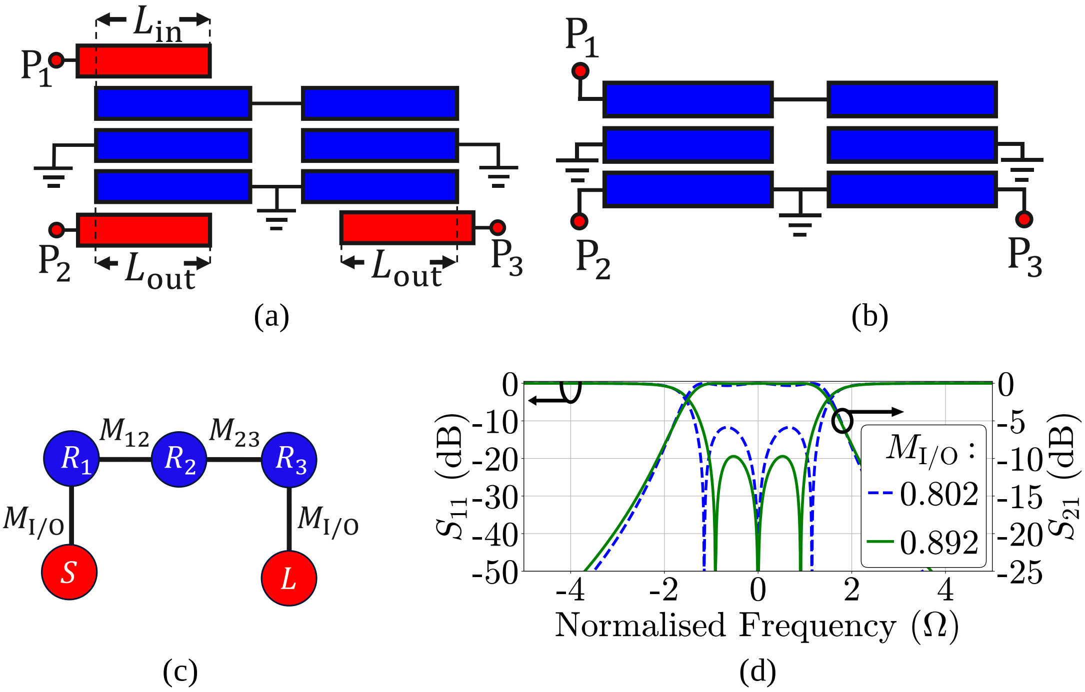

Figure 5.2. (a) 3rd-order BPF-B with its resonators coupled capacitively with the I/O feedlines (WB BPF-B). In this case, L_{in} = 5480 μm and L_{out} = 6050 μm. (b) 3rd-order BPF-B with directly-coupled I/O resonators (UWB BPF-B). (c) Equivalent third-order CRD for the two transmission paths. (d) S-parameters of a third-order BPF-B for M_{12} = 0.707, M_{23} = 0.707, and $M_{I/O}$ = 0.802 (dashed lines) or $M_{I/O}$ = 0.892 (solid lines).

specified using conventional coupled-resonator synthesis techniques. Having specified these coefficients, $M_{12,\mathrm{balun}}$ needs to be set equal to $M_{12}/\sqrt{2}$ to account for the power scaling in the 3-port network [124].

To demonstrate its operation, two example design cases are considered for a 3rd-order Chebyshev TF using M_{12} = 0.707 and M_{23} = 0.707. Shown in Figure 5.2(d), the passband ripple is controlled by $M_{I/O}$, with a 0.05 dB passband ripple for $M_{I/O}$ = 0.892 which is used in the WB case, and a 0.3 dB passband ripple for a lower $M_{I/O}$ = 0.802 which is used in the UWB case. Having specified the TF, the inter-resonator couplings $k_{i,i+1}$ and the external couplings $Q_{e,\mathrm{in}} = Q_{e,\mathrm{out}} = Q_e$ are calculated using (5.1).

$$k_{i,i+1} = \mathrm{FBW} \times M_{i,i+1}, \qquad Q_e = \frac{1}{\mathrm{FBW} \times M_{\mathrm{I/O}}^2} \tag{5.1}$$

The geometrical parameters of the BPF-B can be specified through EM simulations in ANSYS HFSS [116] and the design method in [125].

5.1.2 WB and UWB BPF-B coupled-line integration

Prior to extracting the $k_{i,i+1}$ and Q_e, the coupled line structure and process capabilities of the two-material inkjet process need to be considered. Broadside-coupled, vertically-integrated SL TLs are used as shown in Figure 5.3(a), (c) to achieve the desired couplings and size compactness. By exploiting the design freedom along the *z*-axis, alongside the particular broadside coupled line configuration, a wide range of $k_{i,i+1}$ and Q_e, and thus FBWs can be realised. If seeking to maximise FBW, i.e., the design goal of this work, the UWB BPF-B configuration (i.e., direct I/O coupling) and minimum vertical spacings should be chosen. If seeking lower FBWs <50%, the WB BPF-B configuration (i.e. coupled I/O feeding) can be used with a larger vertical inter-resonator spacings to realise lower couplings. It should be noted that maximum $k_{i,i+1}$ is achieved when the coupled lines are directly above each other, i.e., for $G_{i,i+1} = 0$. $k_{i,i+1}$ can then be finely decreased by increasing $G_{i,i+1}$, allowing for accurate synthesis of the necessary couplings to realise the desired TF. The design procedure for each of the WB and UWB topologies are now outlined.

5.1.2.1 WB BPF-B coupled-line parameter selection

The WB BPF-B was designed for a reasonably-wide FBW of 30% and a 0.05 dB passband ripple, leading to a $Q_e = 4.19$, $k_{12} = 0.15$ and $k_{23} = 0.21$ following (5.1). Its stack up is shown in Figure 5.3(a) where capacitively-coupled feedlines are used for

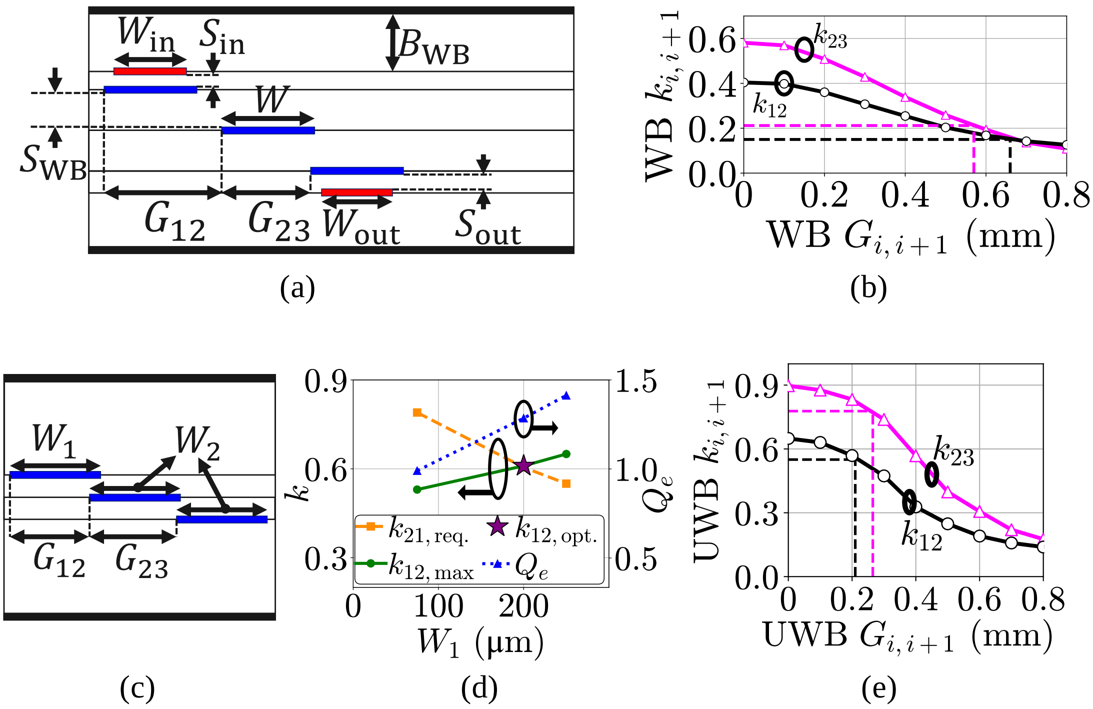

Figure 5.3. (a) Cross section of the WB BPF-B using coupled resonators with I/O feed lines (red) where $W_{\text{in}} = W_{\text{out}} = 480$, $S_{\text{in}} = 60$, $S_{\text{out}} = 160$, $S_{\text{WB}} = 200$, $W_1 = 300$, $B_{\text{WB}} = 140$, $H_{\text{WB}} = 217$, $t = 17$, and $H = 1050$ (unit: μm). (b) Extracted k_{12} and k_{23} as a function of G_{12} and G_{23} for the WB configuration resulting in $G_{12} = 660$ μm and $G_{23} = 570$ μm. (c) Cross section of the UWB BPF-B using directly-coupled resonators where $W_1 = 250$, $W_2 = 351$, $S_{\text{UWB}} = 50$, $H_{\text{UWB}} = 67$, $B_{\text{UWB}} = 450$, and $H = 1050$ (unit: μm). (d) Sizing W_1 for maximum FBW realisation in the UWB BPF-B. The dotted blue lines denote Q_e as a function of W_1. The solid green lines denote the maximum achievable k_{12} as a function of W_1. The dashed orange lines represent the required k_{12} (obtained using (5.1)) for the resultant Q_e as a function of W_1. (e) Extracted k_{12} and k_{23} as a function of G_{12} and G_{23} for the UWB configuration, $G_{12} = 286$ μm and $G_{23} = 280$ μm.

the realization of Q_e. By assigning a vertical inter-resonator spacing $S_{\text{WB}} = 200$ μm, and resonators with a width $W = 300$ μm, the Q_e is predominantly controlled through S_{in} (or S_{out}) [see Figure 5.3(a)] and fine-tuned by L_{in} (or L_{out}) [see Figure 5.2(a)]. $k_{i,i+1}$ is altered through $G_{i,i+1}$ as shown in Figure 5.3(b). The selected geometrical parameters are obtained through full-wave EM simulations and are provided in the caption of Figure 5.3.

5.1.2.2 WB BPF-B coupled-line parameter selection

The UWB BPF-B was designed for the maximum possible FBW and 0.3 dB passband ripple. Thus, the minimum vertical spacing of the process of 50 μm is used for S_{UWB} to maximize the $k_{i,i+1}$. Direct I/O feed lines [see in Figure 5.3(c)] are also used to allow for a sufficiently low Q_e which is controlled by the widths W_1 and W_2 of the I/O resonators, respectively. Generally, narrower trace widths reduce Q_e, and low Q_e is required for wide FBWs. Wide FBWs also require large k, and when using broadside-coupled lines, while narrower trace widths reduce k. Therefore, there is a minimum trace width whose Q_e corresponds to a FBW that has a realisable coupling k. Finally, as the input resonator is OC while the output resonator is SC, it is found that $W_1 < W_2$ for the same Q_e, so the input width W_1 is the limiting parameter. The maximum FBW can therefore be evaluated by sizing the input width W_1 as follows:

Following Figure 5.3(d) and setting W_1 equal to the process minimum of 75 μm, a $Q_e = 0.99$ can be obtained which corresponds to a FBW = 157%. This would require coupling $k_{12,\mathrm{req}} = 0.785$ (calculated using (5.1)) which as shown in Figure 5.3(d) is not possible due to $k_{12,\max} = 0.53$ for $W_1 = 75$ μm (and $G_{12} = 0$). The maximum FBW is then determined by plotting the required $k_{12,\mathrm{req}}$, for each Q_e (dashed orange trace in Figure 5.3(d)) and finding their point of intersection with the $k_{12,\max}$ that can be achieved by the process (green solid line in Figure 5.3(d)) that leads to $\mathrm{FBW}_{\max} =$ 121% for $W_1 = 200$ μm, $Q_e = 1.285$, $k_{12,\mathrm{req.}} = k_{12,\max} = k_{\mathrm{opt.}} = 0.605$, indicated with the star in Figure 5.3(d). Choosing the maximum $\mathrm{FBW}_{\max} = 121\%$ was found to produce a fairly crowded coupled-line structure, causing difficulties in shorting resonators to the top or bottom grounds due to the low required G_{12}. And G_{23}. Therefore, a slightly narrower FBW = 110% (a $Q_e = 1.41$ for $W_1 = 250$ μm, $W_2 = 351$ μm in Figure 5.3(d))

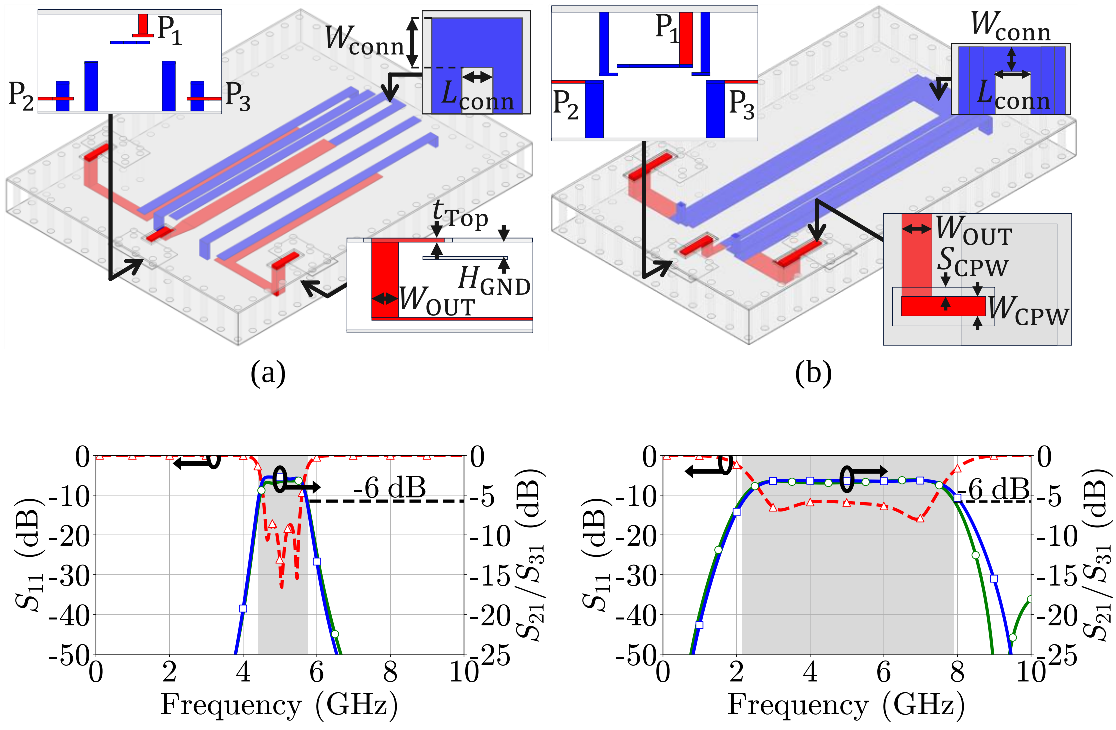

Figure 5.4. 3D geometry and EM simulated S-parameters for the 3[rd]-order BPF-Bs based on broadside-coupled SL lines. (a) Bird's eye view of the WB BPF-B with L_{conn} = 300, W_{conn} = 200, H_{GND} = 187, t_{Top}= 50, and W_{OUT} = 580 (unit: µm). (b) Bird's eye view of the UWB BPF-B with L_{conn} = 950, W_{conn} = 1000, W_{CPW} = 200, S_{CPW} = 100, and W_{OUT} = 580 (unit: µm). (c), (d) EM-simulated S-parameters of the WB and UWB BPF-B, respectively.

was used for the UWB BPF-B implementation. The optimized geometrical dimensions are provided in the caption of Figure 5.3.

5.1.3 WB and UWB BPF-B realisation

The final layouts of the WB BPF-B and UWB BPF-B are shown in Figure 5.4(a), (b). In both, the $\lambda_g/2$ OC resonator is folded side-by-side for size compactness. The inter-connecting line, with dimensions W_{conn} and L_{conn}, is carefully designed to optimise AI and PI throughout the designed FBW using the design method described in Section 2.1.2. The SC resonators are shorted using compact 90° 3D traces that are

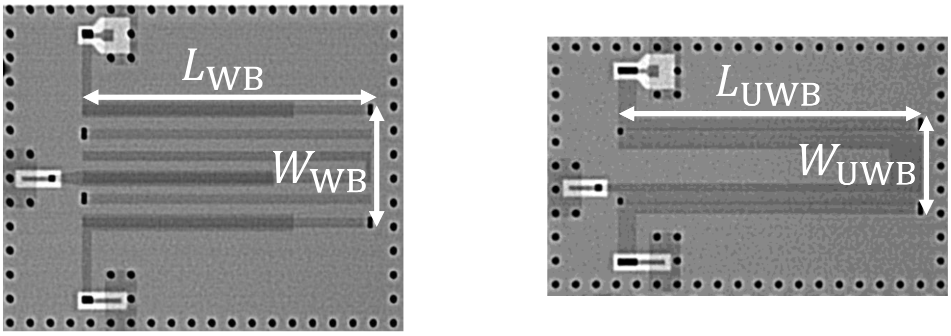

(a) (b)

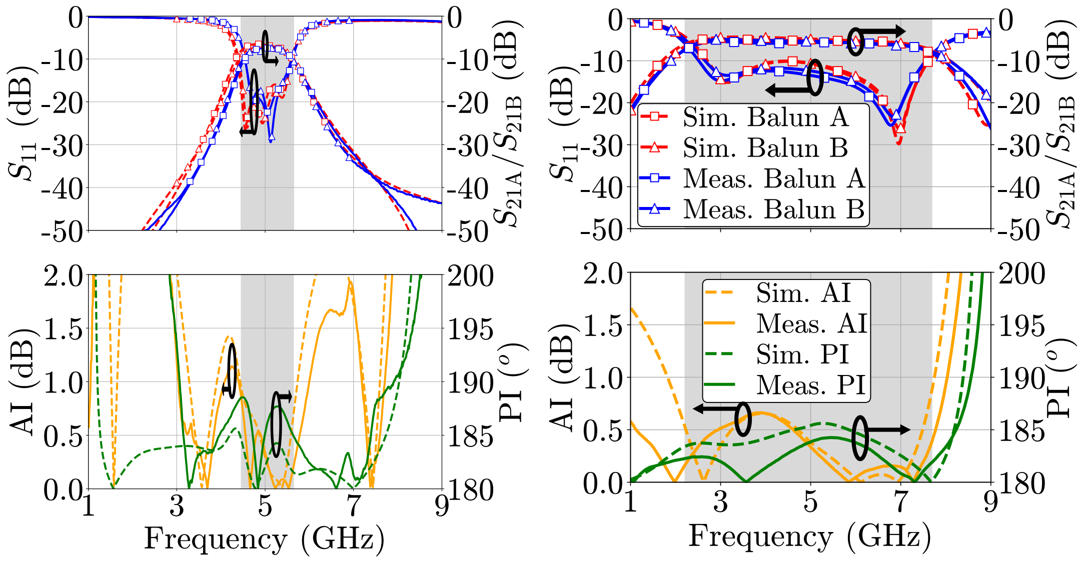

(c) (d)

Figure 5.5. (a), (b) X-ray scans of the WB and UWB BPF-Bs with their P_3 terminated to 0402 50 Ω resistors where $L_{\mathrm{WB}} = 8.9$, $W_{\mathrm{WB}} = 2.7$, $L_{\mathrm{UWB}} = 8.9$, and $L_{\mathrm{UWB}} = 3.5$ (unit: mm). (c), (d) EM-simulated and RF-measured S-parameters (top) and AI and PI (bottom) for the WB and UWB BPF-Bs, respectively. The shaded grey area indicates the operational BW.

only possible using the inkjet-printed process. The RF signal is connected to the BPF-Bs using 90° 3D traces to 50 Ω GCPW terminations. Grounding vias surround the device, connecting the bottom and top grounds and isolating the structure. The WB and UWB baluns are simulated using lossless dielectrics and conductors and their S-parameters are shown in Figure 5.4(c), (d), respectively.

Table 5.1
Comparison with SOA filtering baluns

Ref.	**f_0 (GHz)**	**Loss @ f_0 (dB)**	**FBW (%)**	**AI (dB)**	**PI (°)**	**Technology**	**Area (λ_g^2)**
[14]	5.55	2*	14	<0.6	<5	LTCC	0.007
[50]	3.75	0.9	93	<0.34	<3.5	ML PCB	0.225
[35]	2.25	0.56	111	<0.7	<6	ML PCB	0.173
[13]	5.22	0.5	133	<0.8	<5.8	ML PCB	0.651
WB	**5.0**	**2.3**	**111**	**<0.8**	**<8**	**Inkjet AM**	**0.019**
UWB	**5.0**	**4.3**	**24**	**<0.9**	**<4**	**Inkjet AM**	**0.025**

λ_g: Guided wavelength at f_0; ML: Multilayer; *: Estimated from graphs

5.2 Experimental Validation

The WB and UWB designs were manufactured using the two-material inkjet process and RF characterization was performed with an Agilent E5071C VNA and 250 μm 2-port GSG RF probes. Again, in this case the BPF-Bs were characterized using resistive terminations with two prototypes being tested for each design, namely Balun A (P_3-terminated) and Balun B (P_2-terminated). An X-ray of the WB and UWB Balun A type are provided in Figure 5.5(a), (b). The EM-simulations (including material losses) and RF-measured S-parameters, AI, and PI are provided in Figure 5.5(c), (d). For the WB and UWB designs, the measured power loss, PI and AI were measured between 4.3-7.3 dB and 1.8-5.3 dB, 4 ± 4° and 2 ± 2°, and 0.45 ± 0.45 dB and 0.4 ± 0.4 dB, respectively, with overall footprints of 8.9 × 3.5 mm^2 and 8.9 × 2.7 mm^2. A very good agreement is obtained with the EM simulations, successfully validating the proposed concept.

Table 5.1 compares the inkjet-printed multi-coupled line BPF-B with SOA BPF-Bs. As shown, the proposed configuration exhibits much smaller footprint compared to [13], [121], [35]. Only [14], shows smaller footprint, however it only has a 2nd order TF and provides significantly narrower FBW. Furthermore, this work exhibits 3D vertical integration using a two-material inkjet printing process, which is demonstrated in this work for BPF-Bs for the first time.

5.3 Conclusion

This chapter presented a detailed design methodology for the realization of multi-coupled TL-based BPF-Bs, alongside a unique vertical integration concept using multi-material inkjet printing. A simulation-based method determining the maximum achievable FBW considering the manufacturing process capabilities was reported. For practical validation purposes, both WB and UWB BPF-Bs were designed, manufactured, and tested at C-band, demonstrating competitive RF performance and high levels of miniaturization when compared to the SOA.

6 Conclusions and Outlook

6.1 Summary & Contributions

The primary goal of this thesis was to lay the foundations for new design methodologies and integration techniques for the realization of broadside coupled-line baluns achieving ultra-wide bandwidths, small physical size and the RF co-designed functionality of a BPF. Additionally, the thesis explored the potential of a novel manufacturing process based on inkjet-printed dielectric and conductive materials and benchmarked its potential in relation to streamlined multi-layer PCB process. **Table 6.1** presents a summary of the key metrics of the baluns presented in this thesis. It is evident that low footprint, wide BW designs have been designed demonstrated, with the lowest footprints achieved for the spiral MB designs, and the widest BWs achieved in for the *C*-loaded balun design. The specific contributions of this thesis are as follows:

- Chapter 2 presented a detailed design methodology for the practical development of wideband MBs, alongside a unique integration concept using multi-material inkjet printing. The maximum achievable FBW for alternative

Table 6.1
Performance of fabricated and measured baluns presented in Chapters 2-5

Balun Description	$\boldsymbol{f_0}$ **(GHz)**	**FBW (%)**	**PI (°)**	**AI (dB)**	**Max. Loss (dB)**	**Footprint** $(\boldsymbol{\lambda_g^2})$
PCB SL Spiral MB	6	56	<3	<0.6	2	0.0034
PCB EMS Spiral MB	4.5	71	<7.5	<0.8	1.5	0.0025
Inkjet-printed SL Spiral MB	5	94	<7	<0.6	3.5	0.0043
Interdigital *C*-loaded MB	4.4	122	<5	<0.9	2.5	0.013
Wideband filtering balun	5	20	<8	<1	5	0.025
Ultra-wideband filtering balun	5	100	<4.5	<0.7	4	0.019

RF input/output impedance transformations and achievable couplings were introduced in this thesis for first time. Additionally, this chapter demonstrated that maximising the coupling k does not lead to a maximum FBW response. Rather, a specific k (i.e., k = 0.83 for a 1:1 impedance transformation) yields the maximum FBW. As the maximum FBW response is generally out of reach for most processes, a novel optimization procedure determining the maximum achievable MB FBW dependent on process capabilities was described. Several TL-based integration concepts were analysed using 2D and 3D EM simulations taking into consideration the capabilities of a multi-material multilayer inkjet printing process which is used in this work for the realization of MBs for first time. A miniaturization scheme using spiral TLs and slanted vias was also explored for size compactness. The fabricated miniaturised baluns demonstrated both wide FBWs ~100% and low footprints < 0.005 λ_g^2. The outcomes of this work have been published in [109].

- Chapter 3 applied the design methodology that was established in Chapter 2 to the realisation of the best achievable FBW response for broadside coupled MBs on ML PCB processes. SL and EMS baluns were designed using a 6-layer PCB process, demonstrating their simplicity in design, wide BWs and very small footprints compared to other balun design approaches. The measured balun results allowed for a comparison to be made between the inkjet AM and PCB processes, which highlighted the key advantages of inkjet AM and justified its use in the subsequent balun designs.
- Chapter 4 introduced a detailed design methodology for the realisation of wideband and highly-miniaturized *C*-loaded MBs, alongside a unique integration concept using multi-material inkjet printing. A simulation-based

method determining the maximum achievable FBW (~130%), wider than what is possible with the conventional MB, was described for the first time, while the characteristics of inkjet-printed broadside-coupled lines and 3D vertically-integrated capacitors were investigated. A wideband MB was designed and tested at C-band demonstrating the widest reported *C*-loaded MB FBW to date enabled by a low cost and highly-versatile inkjet printing 3D integration concept.

- Chapter 5 reported on a detailed design methodology for the realization of multi-coupled TL-based BPF-Bs, alongside a unique vertical integration concept using multi-material inkjet printing. A simulation-based method determining the maximum achievable FBW considering the manufacturing process capabilities was reported. For practical validation purposes, both WB and UWB BPF-Bs were designed, manufactured, and tested at C-band, demonstrating competitive RF performance and high levels of miniaturization, providing significantly lower footprints compared to the more common slotline transition approach to BPF-B design.

6.2 List of Publications

1. Wideband Broadside-Coupled Line Baluns Enabled by Multi-Material Additive Manufacturing, **J. Steele**; D. Psychogiou, *IEEE Transactions in Microwave Theory and Techniques*, Date of Publication: 09/05/2024.

2. Compact Multilayer PCB-Based Marchand Baluns with Maximized Fractional Bandwidth, **J. Steele**; D. Psychogiou, *IEEE Access*, Accepted.

3. Inkjet-Printed Capacitively-Loaded Marchand Baluns with Enhanced Fractional Bandwidths, **J. Steele**; D. Psychogiou, *IET Electronics Letters*, Accepted.

4. Self-Packaged Inkjet-Printed Vertically-Integrated RF Co-designed Bandpass Filtering Baluns, **J. Steele**; D. Psychogiou, *IEEE Transactions in Components and Manufacturing Technologies*, Accepted.

6.3 Future Work

Beyond the contributions of this thesis, there are further avenues of research which may promise further balun FBW enhancement and footprint reduction and are summarized as follows:

6.3.1 Alternative two-line topologies

The coupled-line balun topology in Figure 6.1(a) [120] is an alternative to the MB and its design has not yet been explored in regards to FBW maximization. Preliminary studies demonstrate that it can lead to wider FBWs than the MB, but only for unrealistic couplings $k > 0.88$, as indicated by the shaded region in Figure 6.1(b) which compares its FBW performance against the conventional MB. It is believed that the evolving capabilities of inkjet AM have the potential to functionalize the required k and may make this a potential ultra-wideband, highly miniaturizable balun that can be investigated as a further extension of this work.

6.3.2 Alternative capacitively-loaded coupled-line balun topologies

Although the widest FBW C-loaded MB found in the literature was demonstrated in Chapter 4, the survey on capacitive loading demonstrated in this work is not exhaustive. Therefore, alternative capacitive loading combinations can be studied to further enhance FBW and decrease size. For example, the same procedure described in Chapter 4 to find the widest FBW topology can be applied to shunt capacitors rather than series capacitors, or combinations of shunt and series capacitors. The number of

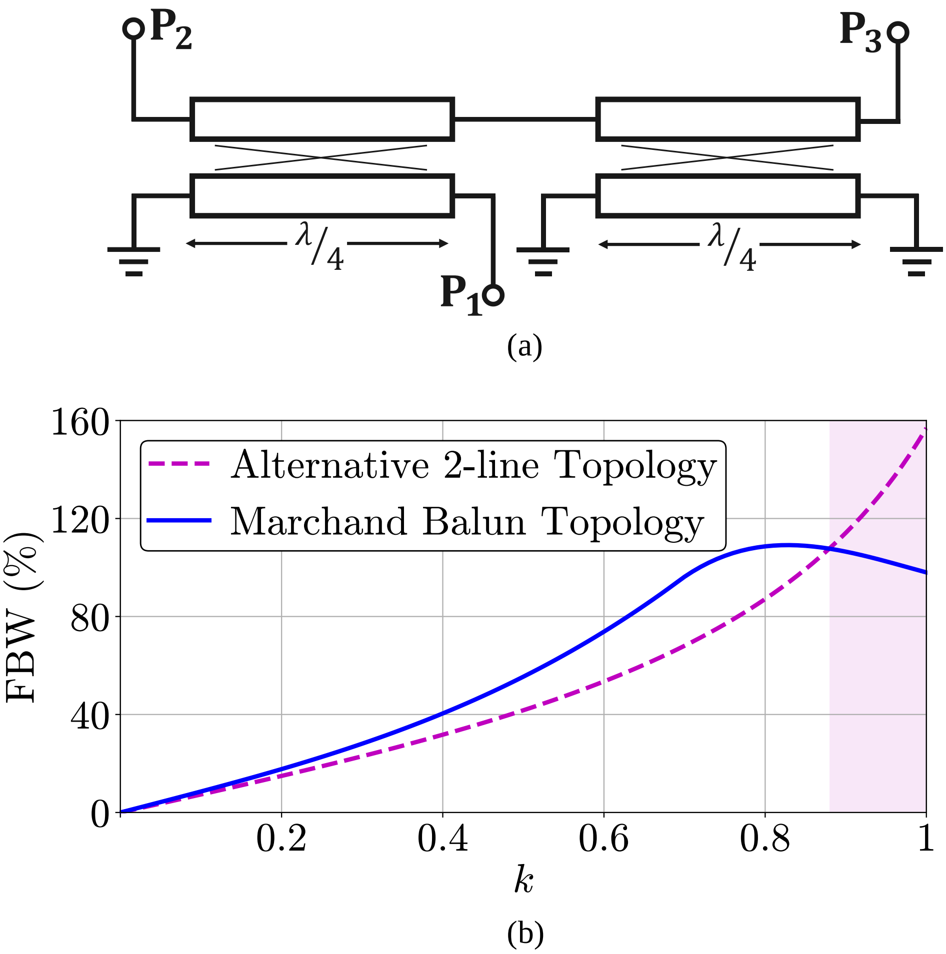

Figure 6.1. (a) An alternative two-line topology to the MB, introduced in [120]. (b) FBW of the MB and alternative 2-line topologies as a function of *k*.

possible configurations is large, and therefore a more sophisticated approach to search for large FBW *C*-loaded topologies is likely required compared to the manual search conducted in Chapter 4. Additionally, capacitive loading can also be applied to the balun topology in Figure 6.1 to explore its FBW enhancement potential.

6.3.3 Patterned ground footprint reduction

As evidenced by the realised balun footprints of the *C*-loaded MB in Chapter 4, the patterned GND increases the overall device footprint. For example, the spiral MB shown in Chapter 2 (with a FBW = 95%) has a footprint of 0.0043 λ_g^2 compared to

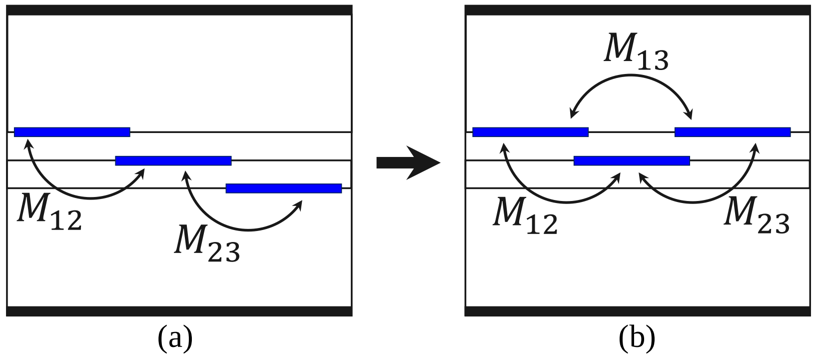

Figure 6.2. (a) Coupled resonator structure employed for the realisation of BPF-Bs in Chapter 5. (b) An alternative coupled resonator configuration which introduces an additional cross-coupling M_{13}.

the C-loaded balun with patterned GND plane (FBW = 122%) having a footprint of 0.013 λ_g^2, increasing footprint by a factor of 3. This increase in footprint is due to the large patterned ground plane required to achieve the coupled-line parameters (k, Z_k) needed to get a FBW = 122%. Rather than using a large slot, other approaches of patterning the ground plane may produce the same (k, Z_k) while occupying a smaller area [114]. Advancements to the integration of this topology which can reduce footprint and further enhance coupled-line parameters could be explored.

6.3.4 Realising advanced BPF-B transfer functions

In this thesis, the design freedoms afforded by the inkjet AM process allowed for the realisation of BPF-Bs with N^{th}-order TFs. The specific integration method used in this work ensured no unwanted cross-couplings which could degrade the passband as shown in Figure 6.2(a). To increase the passband selectivity, transmission zeros (TZs) can be introduced to the transfer function. This requires inter-resonator cross-couplings and therefore more sophisticated coupled-line configurations. For example, a TZ could be introduced to the passbands of the BPF-Bs synthesised in Chapter 5 by introducing the cross-coupling M_{13}, which can be achieved using the configuration illustrated in Figure 6.2(b). This inherently introduces further complexity into the synthesis and optimization of the passband, but the design freedoms afforded by inkjet printed AM technology may allow for the realization of wideband BPF-Bs with enhanced selectivity alongside excellent balanced signal quality throughout the passband.

References

[1] G. Marconi, “Wireless telegraphic communication,” *Nobel Lecture*, vol. 11, pp. 198–222, 1909.

[2] N. E. Lindenblad, “Television transmitting antenna for Empire State Building,” RCA Rev., vol. 3, 1939.

[3] C. H. Liu, C. Y. Hsu, H. R. Chuang, and C. Y. Chen, “A 60-GHz millimeter-wave CMOS Marchand balun using 0.18-μm CMOS technology,” *Microw. Opt. Technol. Lett.*, vol. 51, no. 3, pp. 766–770, 2009, doi: 10.1002/mop.24176.

[4] A. Munk, J. Kraus, and R. Marhefka, *Antennas for all applications*, Third. New York: McGraw-Hill, 2002, page 301.

[5] T. H. Chen *et al.*, “Broadband monolithic passive baluns and monolithic double-balanced mixer,” *IEEE MTT-S Int. Microw. Symp. Dig.*, vol. 2, no. 12, pp. 861–864, 1991, doi: 10.1109/mwsym.1991.147143.

[6] P. Hsu, C. Nguyen, and M. Kintis, “Uniplanar broad-band push–pull FET amplifiers,” *IEEE Trans. Microw. Theory Tech.*, vol. 45, pp. 2150–2152, Dec. 1997.

[7] S. Maas and Y. Ryu, “A broadband, planar, monolithic resistive frequency doubler,” in *IEEE Int. Microw. Symp. Dig.*, 1994, pp. 443–446.

[8] F. Aryanfar and C. Werner, “An amplitude-based phase detector at mm-wave frequency range,” *IEEE MTT-S Int. Microw. Symp. Dig.*, pp. 1–4, 2011, doi: 10.1109/MWSYM.2011.5972986.

[9] D. Simpson and D. Psychogiou, “Multiband magnetless isolators and circulators with reconfigurable bandpass filtering capabilities,” *IEEE Trans. Microw. Theory Tech.*, vol. 71, no. 3, pp. 1239–1250, 2023, doi: 10.1109/TMTT.2022.3218114.

[10] D. Simpson and D. Psychogiou, “GaAs MMIC nonreciprocal single-band, multi-band, and tunable bandpass filters,” *IEEE Trans. Microw. Theory Tech.*, vol. 71, no. 6, pp. 2439–2449, 2023, doi: 10.1109/TMTT.2022.3232103.

[11] M. Fan, K. Song, L. Yang, and R. Gómez-garcía, “Frequency-reconfigurable input-reflectionless bandpass filter and filtering power divider with constant absolute bandwidth,” *IEEE Trans. Circuits Syst. II Express Briefs*, vol. 68, no. 7, pp. 2424–2428, 2021, doi: 10.1109/TCSII.2021.3049417.

[12] Y. Rao, H. J. Qian, Y. Bingzheng, R. Gómez-García, and X. Luo, “Dual-band bandpass filter and filtering power divider with ultra-wide upper stopband using hybrid microstrip / DGS dual-resonance cells,” *IEEE Access*, vol. 8, 2020.

[13] L. P. Feng and L. Zhu, “Wideband filtering balun on a novel hybrid multimode resonator with the functionality of vertical transition,” *IEEE Trans. Components, Packag. Manuf. Technol.*, vol. 7, no. 8, pp. 1324–1330, 2017, doi: 10.1109/TCPMT.2017.2658669.

[14] J.-X. Xu, X. Y. Zhang, and X. Zhao, “Compact LTCC balun with bandpass response based on Marchand balun,” *IEEE Microw. Wirel. Components Lett.*,

vol. 26, no. 7, pp. 493–495, 2016.

[15] S. Lin, J. Wang, G. Zhang, and J. Hong, "Design of microstrip tri-mode balun bandpass filter with high selectivity," *Electron. Lett.*, vol. 51, no. 13, pp. 998–999, 2015, doi: 10.1049/el.2015.1047.

[16] P. H. Tsai, Y. H. Lin, J. L. Kuo, Z. M. Tsai, and H. Wang, "Broadband balanced frequency doublers with fundamental rejection enhancement using a novel compensated Marchand balun," *IEEE Trans. Microw. Theory Tech.*, vol. 61, no. 5, pp. 1913–1923, 2013.

[17] T. Zhang, L. Li, M. Xie, H. Xia, and T. J. Cui, "Low-cost aperture-coupled 60-GHz-phased matching network," *IEEE Trans. Antennas Propag.*, vol. 65, no. 12, pp. 6355–6362, 2017.

[18] S. Selvakumar, S. Adithe, J. S. Isaac, R. Pradhan, V. Venkatesh, and S. B., "A study of the printed circuit board (PCB) E-waste recycling process," in *Sustainable Approaches and Strategies for E-Waste Management and Utilization*, no. June, 2023, pp. 159–184. doi: 10.4018/978-1-6684-7573-7.ch009.

[19] S. Chakraborty, L. E. Milner, X. Zhu, A. Parker, and M. Heimlich, "Analysis and comparison of Marchand and transformer baluns applied in GaAs," *IEEE Trans. Circuits Syst. II Express Briefs*, vol. 69, no. 11, pp. 4278–4282, 2022, doi: 10.1109/TCSII.2022.3180549.

[20] S. Chakraborty, L. E. Milner, A. Parker, and M. Heimlich, "A folded edge-coupled transformer balun in GaAs with excellent balance from 9 to 20 GHz," *2018 48th Eur. Microw. Conf. EuMC 2018*, pp. 1101–1104, 2018, doi: 10.23919/EuMC.2018.8541427.

[21] Y. Ye, B. Yu, A. Tang, B. Drouin, and Q. J. Gu, "A high efficiency e-band CMOS frequency doubler with a compensated transformer-based balun for matching enhancement," *IEEE Microw. Wirel. Components Lett.*, vol. 26, no. 1, pp. 40–42, 2016, doi: 10.1109/LMWC.2015.2505617.

[22] L. Jing, A. Li, D. Luo, C. R. Rowell, and C. P. Yue, "Millimeter-wave 4:1 transformer-based balun design for CMOS RF IC's," *2015 IEEE Int. Wirel. Symp. IWS 2015*, pp. 1–4, 2015, doi: 10.1109/IEEE-IWS.2015.7164519.

[23] W. Z. Chen, W. H. Chen, and K. C. Hsu, "Three-dimensional fully symmetric inductors, transformer, and balun in CMOS technology," *IEEE Trans. Circuits Syst. I Regul. Pap.*, vol. 54, no. 7, pp. 1413–1423, 2007, doi: 10.1109/TCSI.2007.899628.

[24] J. Li, S. Qu, and Q. Xue, "Miniaturised branch-line balun with bandwidth enhancement," *Electron. Lett.*, vol. 43, no. 17, pp. 1–2, 2007, doi: 10.1049/el. 20071074

[25] I. S. Krishna and S. Mukherjee, "Design of folded substrate integrated coaxial line wideband balun for K-band applications," *2018 IEEE Indian Conf. Antennas Propagation, InCAP 2018*, pp. 9–12, 2018, doi: 10.1109/INCAP.2018.8770732.

[26] I. Bulu and H. Caglayan, "A wideband high selectivity filtering balun," *Microw.*

Opt. Technol. Lett., vol. 57, no. 5, pp. 1107-1110, 2015.

[27] C. Liu and W. Menzel, "Broadband via-free microstrip balun using metamaterial transmission lines," *IEEE Microw. Wirel. Components Lett.*, vol. 18, no. 7, pp. 437–439, 2008, doi: 10.1109/LMWC.2008.924913.

[28] M. S. Mahani and R. Abhari, "A planar ultra wide band single layer microstrip balun operating from 200 MHz to 10 GHz," *IEEE MTT-S Int. Microw. Symp. Dig.*, pp. 26–28, 2012, doi: 10.1109/MWSYM.2012.6259713.

[29] J. Shao, X.-H. Wang, C. Chen, R. Zhou, H. Kim, and H. Zhang, "Design of a wideband balun using parallel strips," *Proc. 2013 IEEE Texas Symp. Wirel. Microw. Circuits Syst. WMCS 2013*, vol. 23, no. 3, pp. 125–127, 2013, doi: 10.1109/WMCaS.2013.6563568.

[30] J.-S. Lim *et al.*, "800–5000MHz ultra-wideband CPW balun," *Electron. Lett.*, vol. 42, no. 18, pp. 1037–1039, 2006.

[31] M. A. Antoniades and G. V Eleftheriades, "A broadband Wilkinson balun using microstrip metamaterial lines," in *IEEE Antennas Wirel. Propag. Lett.*, 2005, pp. 209–212.

[32] C.-H. Tseng and C.-L. Chang, "Wide-band balun using composite right/left-handed transmission line," *Electron. Lett.*, vol. 41, no. 2, pp. 40–41, 2005, doi: 10.1049/el.

[33] Y. Q. Yu, W. Jiang, L. Qin, H. Y. Shao, and S. X. Gong, "Design of a planar transmission line balun based on novel phase inverter," *IEEE Access*, vol. 8, pp. 18915–18924, 2020, doi: 10.1109/ACCESS.2020.2968341.

[34] Z. Y. Zhang, Y. X. Guo, L. C. Ong, and M. Y. W. Chia, "A new wide-band planar balun on a single-layer PCB," *IEEE Microw. Wirel. Components Lett.*, vol. 15, no. 6, pp. 416–418, 2005, doi: 10.1109/LMWC.2005.850486.

[35] S. Guan, X. Bi, Q. Ma, and Q. Xu, "A wideband balun filter based on folded ring slotline resonator and dual-feedback stubs With 17.8 f_0 stopband rejection," *IEEE Trans. Circuits Syst. II Express Briefs*, vol. 70, no. 2, pp. 466–470, Feb. 2023, doi: 10.1109/TCSII.2022.3174954.

[36] Z. Feng, X. Bi, Z. Cao, A. Shen, Q. Ding, and Q. Xu, "A filtering balun utilizing multi-ring loaded vertical transition structure with 161% fractional bandwidth and 5.8 f_0 stopband," *IEEE Trans. Circuits Syst. II Express Briefs*, vol. 69, no. 4, pp. 2061–2065, 2022, doi: 10.1109/TCSII.2021.3139158.

[37] A. K. Poddar, U. L. Rohde, V. Madhavan, and S. K. Koul, "A novel UWB balun: application in 5G systems," *2016 IEEE Int. Freq. Control Symp. IFCS 2016 - Proc.*, 2016, doi: 10.1109/FCS.2016.7546747.

[38] Z. Chi, Y. Rao, Z. Deng, C. Han, and X. Luo, "Wideband filtering balun with wide stopband and imbalance compensation using hybrid DGS with float strip-line," *2021 IEEE Int. Symp. Radio-Frequency Integr. Technol. RFIT 2021*, pp. 2021–2023, 2021, doi: 10.1109/RFIT52905.2021.9565284.

[39] L. Yang *et al.*, "Wideband balanced-to-unbalanced bandpass filters synthetically designed with chebyshev filtering response," *IEEE Trans. Microw. Theory Tech.,* vol. 66, no. 10, pp. 4528–4539, 2018.

[40] B. L. Pham, H. H. Ta, A. V. Pham, R. E. Leoni, and Y. Leviatan, "23:1 Bandwidth ratio quasi-lumped component balun on a multilayer organic substrate," *IET Microwaves, Antennas Propag.*, vol. 10, no. 5, pp. 561–567, 2016, doi: 10.1049/iet-map.2015.0589.

[41] C. Van Pham, B. Pham, A. V. Pham, and R. E. Leoni, "A 46:1 bandwidth ratio balun on multilayer organic substrate," *2015 IEEE MTT-S Int. Microw. Symp. IMS 2015*, pp. 46–48, 2015, doi: 10.1109/MWSYM.2015.7166899.

[42] H. H. Ta and A. V. Pham, "A compact broadband balun on multilayer organic substrate," *Microw. Opt. Technol. Lett.*, vol. 55, no. 8, pp. 1957–1959, 2013, doi: 10.1002/mop.27670.

[43] H. H. Ta, B. Le Pham, and A. Pham, "Compact wide bandwidth balun based on modified asymmetric broadside coupled lines," *IEEE Microw. Wirel. Components Lett.*, vol. 22, no. 12, pp. 624–626, 2012.

[44] H. Chung, H. Chiou, Y.-C. Hsu, T.-Y. Yang, and C.-L. Chang, "Design of step-down broadband and low-loss Ruthroff-type baluns using IPD technology," *IEEE Trans. Compon., Packag. Manuf. Technol.*, vol. 4, no. 6, pp. 967–974, 2014.

[45] A. Abbosh, "Planar ultra-wideband balun using coupled microstrip lines," *Electron*, vol. 49, no. 10, pp. 10–11, 2013, doi: 10.1049/el.2013.0922.

[46] A. M. Pavio and K. Anthony, "A monolithic or hybrid broadband compensated balun," in *IEEE Int. Microw. Symp. Dig.*, 1990, pp. 483–486.

[47] S. Chakraborty, L. E. Milner, X. Zhu, O. Sevimli, A. E. Parker, and M. C. Heimlich, "An edge-coupled Marchand balun with partial ground for excellent balance in 0.13 μm SiGe technology," *IEEE Trans. Circuits Syst. II Express Briefs*, vol. 68, no. 1, pp. 226–230, 2021, doi: 10.1109/TCSII.2020.3004642.

[48] Z. Xu and L. MacEachern, "Optimum design of wideband compensated and uncompensated Marchand baluns with step transformers," *IEEE Trans. Microw. Theory Tech.*vol. 57, no. 8, pp. 2064–2071, 2009.

[49] C. Cho and K. C. Gupta, "A new design procedure for single-layer and two-layer three-line baluns," *IEEE Trans. Microw. Theory Tech.*, vol. 46, no. 12, pp. 2514–2519, 1998.

[50] F. Huang, J. Wang, K. Aliqab, J. Hong, and W. Wu, "Analysis and design of a new self-packaged wideband balun bandpass filter with the functionality of impedance transformation," *IEEE Trans. Microw. Theory Tech.*, vol. 67, no. 6, pp. 2322–2330, 2019.

[51] C. Tang, W. Cheng, J. Wu, and Y. Lin, "Design of a compact balun with three octant-wavelength coupled lines," *IEEE Int. Microw. Symp.*, vol. 2, pp. 109–112, 2010.

[52] Y. Chen and H. Lin, "Novel broadband planar balun using multiple coupled lines," in 2006 *Microw. Symp. Dig.*, pp. 1571–1574, 2006.

[53] J. Schellenberg and H. Do-ky, "Low-loss, planar monolithic baluns for K/Ka-band applications," *IEEE MTT-S Int. Microw. Symp. Dig.*, pp. 1733–1736, 1999.

[54] Y. Dai, H. Yin, Y. Feng, P. Li, Q. Han, and M. Han, "A LTCC miniaturized broadband modified Marchand balun," *2012 Int. Symp. Commun. Inf. Technol. Isc. 2012*, pp. 110–113, 2012, doi: 10.1109/ISCIT.2012.6380858.

[55] Y. Li, X. Zhu, L. Tian, and R. Liu, "Compact 2 – 18 GHz on-chip balun based on centrosymmetric spiral transformers," *Electron. Lett.*, vol. 56, no. 5, pp. 229–230, 2020, doi: 10.1049/el.2019.3253.

[56] N. Marchand, "Transmission line conversion transformers," *Electron*, vol. 17, no. 12, pp. 142–145, 1944.

[57] R. Bawer and J. J. Wolfe, "A printed circuit balun for use with spiral antennas," *IEEE Trans. Microw. Theory Tech.*, vol. 8, no. 3, pp. 319–325, 1960.

[58] K. C. Lin and Y. C. Lin, "A simple printed compensated balun for enhanced ultra-wideband performances," *IEEE Microw. Wirel. Components Lett.*, vol. 24, no. 1, pp. 5–7, 2014, doi: 10.1109/LMWC.2013.2285211.

[59] A. C. Chen, A.-V. Pham, and R. E. Leoni III, "Development of low-loss broad-band planar baluns using multilayered organic thin films," *IEEE Trans. Microw. Theory Tech.*, vol. 53, no. 11, pp. 3648–3655, 2005.

[60] A. C. Chen, A. V Pham, and R. E. Leoni III, "A novel broadband even-mode matching network for Marchand baluns," *IEEE Trans. Microw. Theory Tech.*, vol. 57, no. 12, pp. 2973–2980, 2009.

[61] X. Lan *et al.*, "An ultra-wideband balun using multi-metal GaAs MMIC technology," *IEEE Microw. Wirel. Compon. Lett.*, vol. 20, no. 8, pp. 474–476, 2010.

[62] Z. Zhang, Y. X. Guo, L. C. Ong, and M. Y. W. Chia, "Improved planar Marchand balun using a patterned ground plane," *Int. J. RF Microw. Comput. Eng.*, vol. 15, no. 3, pp. 307–316, 2005, doi: 10.1002/mmce.20084.

[63] G. Yang, Z. Wang, Z. Li, Q. Li, and F. Liu, "Balance-compensated asymmetric Marchand baluns on silicon for MMICs," *IEEE Microw. Wirel. Compon. Lett.*, vol. 24, no. 6, pp. 391–393, 2014.

[64] M. J. Chiang, H. S. Wu, and C. K. C. Tzuang, "A compact CMOS marchand balun incorporating meandered multilayer edge-coupled transmission lines," *IEEE MTT-S Int. Microw. Symp. Dig.*, no. 1, pp. 125–128, 2009, doi: 10.1109/MWSYM.2009.5165648.

[65] H. W. Chin, L. T. Hwang, F. S. Chang, S. M. Wang, and P. S. Li, "Design of an IPD ultra wideband Marchand balun using a phase compensation line," in *2015 Asia-Pacific Microw. Conf.*, 2015, pp. 1–3.

[66] K. Nishikawa, I. Toyoda, and T. Tokumitsu, "Compact and broad-band three-dimensional MMIC balun," *IEEE Trans. Microw. Theory Tech.*, vol. 47, no. 1, pp. 96–98, 1999.

[67] W. M. Fathelbab and M. B. Steer, "New classes of miniaturized planar Marchand baluns," *IEEE Trans. Microw. Theory Tech.*, vol. 53, no. 4, pp. 1211–1220, 2005.

[68] M. Johnston, C. Van Niekerk, and D. I. L. de Villiers, "Ultra-wideband planar

Marchand balun design for the pyramidal sinuous antenna," in *2019 IEEE AP-S Int. Symp. Dig.*, 2019, pp. 735–736.

[69] R. Phromloungsri, M. Chongcheawchamnan, and I. D. Robertson, "Inductively compensated parallel coupled microstrip lines and their applications," *IEEE Trans. Microw. Theory Tech.*, vol. 54, no. 9, pp. 3571–3582, 2006.

[70] C. H. Tseng and Y. C. Hsiao, "A new broadband Marchand balun using slot-coupled microstrip lines," *Microw. Wirel. Compon. Lett.*, vol. 20, no. 3, pp. 157–159, 2010.

[71] S. Chakraborty, L. E. Milner, X. Zhu, O. Sevimli, A. E. Parker, and M. C. Heimlich, "An Edge-Coupled Marchand Balun with Partial Ground for Excellent Balance in 0.13 µm SiGe Technology," *IEEE Trans. Circuits Syst. II Express Briefs*, vol. 68, no. 1, pp. 226–230, 2021, doi: 10.1109/TCSII.2020.3004642.

[72] F. Zhu, W. Hong, J. X. Chen, and K. Wu, "Ultra-wideband single and dual baluns based on substrate integrated coaxial line technology," *IEEE Trans. Microw. Theory Tech.*, vol. 60, no. 10, pp. 3062–3070, 2012, doi: 10.1109/TMTT.2012.2209448.

[73] H. L. Lee, D. Z. Kim, W. G. Lim, M. Q. Lee, and J. W. Yu, "Miniaturized lumped-distributed wideband balun using double-sided CPW structure," in *European Microw. Conf. (EuMC)*, 2009, pp. 1171–1174.

[74] C. Y. Chang and C. W. Tang, "A semi-lumped balun fabricated by low temperature co-fired ceramic," in *IEEE MTT-S Int. Microw. Symp. Dig.*, 2002, pp. 2201–2204. doi: 10.1109/mwsym.2002.1012309.

[75] T. K. Johansen and V. Krozer, "A 38 to 44 GHz sub-harmonic balanced HBT mixer with integrated miniature spiral type Marchand balun," *Prog. Electromagn. Res.*, vol. 135, pp. 317–330, 2013.

[76] Y. Wang, J. Lee, and S. Member, "A miniaturized Marchand balun model with short-end and capacitive feeding," *IEEE Access*, vol. 6, pp. 26653–26659, 2018, doi: 10.1109/ACCESS.2018.2834948.

[77] K. S. Ang, Y. C. Leong, and C. H. Lee, "Analysis and design of miniaturized lumped-distributed impedance-transforming baluns," *IEEE Trans. Microw. Theory Tech.*, vol. 51, no. 3, pp. 1009–1017, 2003.

[78] Y. X. Guo, Z. Y. Zhang, L. C. Ong, and M. Y. W. Chia, "Design of miniaturized LTCC baluns," *Int. J. RF Microw. C. E.*, vol. 16, no. 3, pp. 268–279, 2006, doi: 10.1109/MWSYM.2006.249614.

[79] R. Phromloungsri, S. Srisathit, M. Chongcheawchamnan, and I. D. Robertson, "Novel technique for performance improvement in impedance-transforming planar Marchand baluns," *2005 Eur. Microw. Conf.*, vol. 1, p. 4 pp., doi: 10.1109/EUMC.2005.1608911.

[80] S. Tseng, C. Meng, C. Chang, and G. Huang, "SiGe HBT Gilbert downconverter with an integrated miniaturized Marchand balun for UWB applications," *IEEE MTT-S Int. Microw. Symp. Dig.*, 2007, pp. 2141–2144.

[81] Y. X. Guo, Z. Y. Zhang, and L. C. Ong, "Design of miniaturized LTCC baluns,"

IEEE MTT-S Int. Microw. Symp. Dig., pp. 1567–1570, 2006, doi: 10.1109/MWSYM.2006.249614.

[82] V. M. Pepino, A. F. Da Mota, A. Martins, and B. H. V. Borges, "3-D-printed dielectric metasurfaces for antenna gain improvement in the ka-band," *IEEE Antennas Wirel. Propag. Lett.*, vol. 17, no. 11, pp. 2133–2136, 2018, doi: 10.1109/LAWP.2018.2860521.

[83] S. Wang, X. Zhang, L. Zhu, and W. Wu, "Single-fed wide-beamwidth circularly polarized patch antenna using dualfunction 3-D printed substrate," *IEEE Antennas Wirel. Propag. Lett.*, vol. 17, no. 4, pp. 649–653, 2018, doi: 10.1109/LAWP.2018.2810105.

[84] S. Alkaraki, Y. Gao, S. Stremsdoerfer, E. Gayets, and C. G. Parini, "3D printed corrugated plate antennas with high aperture efficiency and high gain at X-band and Ka-band," *IEEE Access*, vol. 8, pp. 30643–30654, 2020, doi: 10.1109/ACCESS.2020.2972101.

[85] K. Johnson *et al.*, "Digital manufacturing of pathologically-complex 3D printed antennas," *IEEE Access*, vol. 7, pp. 39378–39389, 2019, doi: 10.1109/ACCESS.2019.2906868.

[86] V. T. Bharambe, J. Ma, M. D. Dickey, and J. J. Adams, "Planar, multifunctional 3D printed antennas using liquid metal parasitics," *IEEE Access*, vol. 7, pp. 134245–134255, 2019, doi: 10.1109/ACCESS.2019.2942058.

[87] S. Sarjoghian, M. H. Sagor, Y. Alfadhl, and X. Chen, "A 3D-printed high-dielectric filled elliptical double-ridged horn antenna for biomedical monitoring applications," *IEEE Access*, vol. 7, pp. 94977–94985, 2019, doi: 10.1109/ACCESS.2019.2928629.

[88] B. Li, P. F. Jing, L. Q. Sun, K. W. Leung, and X. Lv, "3D printed OAM reflectarray using half-wavelength rectangular dielectric element," *IEEE Access*, vol. 8, pp. 142892–142899, 2020, doi: 10.1109/ACCESS.2020.3013678.

[89] B. Sanz-Izquierdo and E. A. Parker, "3-D printing of elements in frequency selective arrays," *IEEE Trans. Antennas Propag.*, vol. 62, no. 12, pp. 6060–6066, 2014, doi: 10.1109/TAP.2014.2359470.

[90] A. Vallecchi, D. Cadman, W. G. Whittow, J. Vardaxoglou, E. Shamonina, and C. J. Stevens, "3-D printed bandpass filters with coupled vertically extruded split ring resonators," *IEEE Trans. Microw. Theory Tech.*, vol. 67, no. 11, pp. 4341–4352, 2019, doi: 10.1109/TMTT.2019.2934456.

[91] G. Lipkowitz *et al.*, "Injection continuous liquid interface production of 3D objects," *Sci. Adv.*, vol. 8, no. 39, pp. 1349–1352, 2022, doi: 10.1126/sciadv.abq3917.

[92] J. P. Kruth, X. Wang, T. Laoui, and L. Froyen, "Lasers and materials in selective laser sintering," *Assem. Autom.*, vol. 2315, no. 5, pp. 357–371, 2003.

[93] P. M. Njogu *et al.*, "Evaluation of planar inkjet-printed antennas on a low-cost origami flapping robot," *IEEE Access*, vol. 8, pp. 164103–164113, 2020, doi: 10.1109/ACCESS.2020.3020824.

[94] S. Jun *et al.*, "Circular polarised antenna fabricated with low-cost 3D and inkjet printing equipment," *Electron. Lett.*, vol. 53, no. 6, pp. 370–371, 2017, doi: 10.1049/el.2016.4605.

[95] A. Chauraya *et al.*, "Inkjet printed dipole antennas on textiles for wearable communications," *IET Microw., Antennas Propag.*, vol. 7, no. 9, pp. 760–767, 2013, doi: 10.1049/iet-map.2013.0076.

[96] B. S. Cook and A. Shamim, "Inkjet printing of novel wideband and high gain antennas on low-cost paper substrate," *IEEE Trans. Antennas Propag.*, vol. 60, no. 9, pp. 4148–4156, 2012, doi: 10.1109/TAP.2012.2207079.

[97] G. McKerricher, D. Titterington, and A. Shamim, "A fully inkjet-printed 3-D honeycomb-inspired patch antenna," *IEEE Antennas Wirel. Propag. Lett.*, vol. 15, pp. 544–547, 2016, doi: 10.1109/LAWP.2015.2457492.

[98] B. K. Tehrani, B. S. Cook, and M. M. Tentzeris, "Inkjet printing of multilayer millimeter-wave Yagi-Uda antennas on flexible substrates," *IEEE Antennas Wirel. Propag. Lett.*, vol. 15, pp. 143–146, 2015.

[99] M. Kacar, T. M. Weller, and G. Mumcu, "3D printed wideband multilayered dual-polarized stacked patch antenna with integrated MMIC switch," *IEEE Open J. Antennas Propag.*, vol. 2, no. October 2020, pp. 38–48, 2021, doi: 10.1109/OJAP.2020.3041959.

[100] Nano Dimension, "The Material Advantage of DragonFly™." [Online]. Available: https://www.nano-di.com/ame-materials. Accessed: 10/05/2024.

[101] J. Zhu *et al.*, "Additively manufactured millimeter-wave dual-band single-polarization shared aperture fresnel zone plate metalens antenna," *IEEE Trans. Antennas Propag.*, vol. 69, no. 10, pp. 6261–6272, 2021, doi: 10.1109/TAP.2021.3070224.

[102] M. Li, F. Iacopi, Y. Yang, J. Nulman, and S. Chappel-Ram, "3D-printed low-profile single-substrate multi-metal layer antennas and array with bandwidth enhancement," *IEEE Access*, vol. 8, pp. 217370–217379, 2020.

[103] J. Zhu, M. Li, J. Lai, and Y. Yang, "Multimaterial additively manufactured transmissive spin-decoupled polarization-maintaining metasurfaces," *Laser Photonics Rev.*, vol. 17, no. 12, pp. 1–13, 2023, doi: 10.1002/lpor.202300433.

[104] J. Zhu, Y. Yang, J. Lai, and J. Nulman, "Additively manufactured polarization insensitive broadband transmissive metasurfaces for arbitrary polarization conversion and wavefront shaping," *Adv. Opt. Mater.*, vol. 10, no. 21, pp. 1–12, 2022, doi: 10.1002/adom.202200928.

[105] J. Zhu, Y. Yang, N. Hu, S. Liao, and J. Nulman, "Additively manufactured multi-material ultrathin metasurfaces for broadband circular polarization decoupled beams and orbital angular momentum generation," *ACS Appl. Mater. Interfaces*, vol. 13, no. 49, pp. 59460–59470, 2021, doi: 10.1021/acsami.1c16493.

[106] J. Zhu, Y. Yang, F. Wang, J. Lai, and M. Li, "3D printed spin-decoupled transmissive metasurfaces based on versatile broadband cross-polarization rotation meta-atom," *Adv. Opt. Mater.*, vol. 11, no. 4, 2023, doi:

10.1002/adom.202202416.

[107] M. Li, Y. Yang, F. Iacopi, M. Yamada, and J. Nulman, "Compact multilayer bandpass filter using low-temperature additively manufacturing solution," *IEEE Trans. Electron Devices*, vol. 68, no. 7, pp. 3163–3169, 2021, doi: 10.1109/TED.2021.3072926.

[108] M. Li, Y. Yang, Y. Zhang, F. Iacopi, S. Ram, and J. Nulman, "A fully integrated conductive and dielectric additive manufacturing technology for microwave circuits and antennas," *2020 50th Eur. Microw. Conf. EuMC 2020*, pp. 392–395, 2021, doi: 10.23919/EuMC48046.2021.9338141.

[109] J. Steele and D. Psychogiou, "Wideband broadside-coupled line baluns enabled by multi-material additive manufacturing," *IEEE Trans. Microw. Theory Tech.*, vol. Preprint, 2024. Published: 09/05/2024.

[110] Keysight Technologies, "Advanced Design System (ADS)." 2021. [Online]. Available: https://www.keysight.com/en/pd-1000000716%3Aepsg%3Apro-pn-ADS. Accessed: 09/05/2024.

[111] C. Hsiao-Wei, H. Lih-Tyng, C. Fa-Shian, W. Shun-Min, and L. Pei-Shuo, "Design of an IPD ultra wideband Marchand balun using a phase compensation line" in 2015 *IEEE Asia-Pacific Microw. Conf. (APMC)*, 2015, pp. 1-3.

[112] R. H. Jansen, J. Jotzo, and R. Engels, "Improved compaction of multilayer MMIC/MCM: baluns using lumped element compensationcm:," *IEEE Int. Microw. Symp. Dig.*, vol. 1, pp. 277–280, 1997.

[113] M. C. Tsai, "New compact wideband balun," *IEEE MTT-S Int. Microw. Symp. Dig.*, pp. 123–125, 1993.

[114] Z. Zhang, Y. X. Guo, L. C. Ong, and M. Y. W. Chia, "Improved planar Marchand balun using a patterned ground plane," *IEEE Trans. Microw. Theory Tech.*, vol. 15, no. 3, pp. 307–316, 2005.

[115] D. Sokol, M. Yamada, and J. Nulman, "Design and performance of additively manufactured in-circuit board planar capacitors," *IEEE Electron Device Lett.*, vol. 68, no. 11, pp. 5747–5752, 2021, doi: 10.1109/TED.2021.3117934.

[116] Ansys Inc., "High-Frequency Structure Simulator (HFSS)." [Online]. Available: https://www.ansys.com/products/electronics/ansys-hfss. Accessed: 10/05/2024.

[117] I. J. Bahl and P. Bhartia, "Characteristics of inhomogeneous broadside-coupled striplines," *IEEE Trans. Microw. Theory Tech.*, vol. 28, no. 6, pp. 529–535, 1980.

[118] S. M. Wang, C. H. Chi, M. Y. Hsieh, and C. Y. Chang, "Miniaturized spurious passband suppression microstrip filter using meandered parallel coupled lines," *IEEE Trans. Microw. Theory Tech.*, vol. 53, no. 2, pp. 747–753, 2005.

[119] D. Sokol, M. Yamada, and J. Nulman, "Design and performance of additively manufactured in-circuit board planar capacitors," *IEEE Trans. Electron Devices*, vol. 68, no. 11, pp. 5747–5752, 2021, doi: 10.1109/TED.2021.3117934.

[120] Y. Dai, H. Yin, Y. Feng, P. Li, Q. Han, and M. Han, “A LTCC miniaturized broadband modified Marchand balun,” in *2012 Int. Symp. Commun. Inf. Technol.*, IEEE, 2012, pp. 110–113. doi: 10.1109/ISCIT.2012.6380858.

[121] F. Huang, J. Wang, J. Hong, and W. Wu, “Wideband balun bandpass filter with broadside-coupled microstrip/slotline resonator structure,” *Electron. Lett.*, vol. 53, no. 19, pp. 1320–1321, 2017, doi: 10.1049/el.2017.2835.

[122] C. W. Tang and C. Y. Chang, “A semi-lumped balun fabricated by low temperature co-fired ceramic,” in *IEEE MTT-S International Microwave Symposium Digest*, 2002, pp. 2201–2204. doi: 10.1109/mwsym.2002.1012309.

[123] C. Y. Ng, M. Chongcheawchamnan, and I. D. Robertson, “Analysis and design of a high-performance planar Marchand balun,” in *2002 IEEE AP-S Int. Symp. Dig.*, 2002, pp. 113–116.

[124] L. K. Yeung and K. Wu, “An LTCC balanced-to-unbalanced extracted-pole bandpass filter with complex load,” *IEEE Trans. Microw. Theory Tech.*, vol. 54, no. 4, pp. 1512–1518, 2006.

[125] J.-S. Hong, *Microstrip filters for RF/microwave applications*, Second. Wiley, 2011, pp. 330-342.

[126] Y. Jen and J. Tsai, “Design and analysis of a 55 – 71-GHz compact and broadband distributed active transformer power amplifier in 90-nm CMOS process,” *IEEE Trans. Microw. Theory Tech.,* vol. 57, no. 7, pp. 1637–1646, 2009, doi: 10.1109/TMTT.2009.2021876.

[127] C. Lin, M. Yeh, J. Fu, H. Chang, K. Lin, and W. Huei, “Analysis of multiconductor coupled-line Marchand baluns for miniature MMIC design,” *IEEE Trans. Microw. Theory Tech.,* vol. 55, no. 6, pp. 1190–1199, 2007.

[128] G. Yang, K. Tang, and Z. Wang, “3.6-8.1 GHz CMOS balun with 1.8° in-band phase difference by using capacitive balance compensation technique,” *Microw. Opt. Technol. Lett.,* vol. 62, no. 4, pp. 1548–1551, 2020, doi: 10.1002/mop.32228.

[129] D. Jorgensen and C. Marki, “Balun basics primer”, *Marki Microwave*, 2014.

[130] K. Hu, M. Tang, M. Li, R. Ziolkowski, “Compact, Low-Profile, Bandwidth-Enhanced Substrate Integrated Waveguide Filtenna,” *IEEE Antennas Wirel. Propag. Lett.*, vol. 17, no. 8, pp. 1552–1556, 2018, doi: 10.1109/LAWP.2018.2854898.